MODELLING OF PHASE CHANGE MATERIAL FOR THERMAL MANAGEMENT OF A LI-ION BATTERY MODULE

Lappeenranta–Lahti University of Technology LUT

Energy Technology, Master's Thesis

Master's programme in Sustainable Energy Systems

2026

Ellinoora Veikkanen

Examiners: Professor Jouni Ritvanen

Professor Pertti Kauranen

ABSTRACT

Lappeenranta–Lahti University of Technology LUT

LUT School of Energy Systems

Energy Technology

Ellinoora Veikkanen

Modelling of phase change material for thermal management of a Li-ion battery module

Master's thesis

2026

92 pages, 40 figures, 7 tables and 7 appendices

Examiners: Professor Jouni Ritvanen and Professor Pertti Kauranen

Keywords: phase change material, Li-ion, battery, computational fluid dynamics, thermal runaway

This thesis studied thermal behaviour of a phase change material (PCM) as a battery thermal management system. The objective was to develop a computational fluid dynamics (CFD) model and capture the effects of PCM and possible natural convection. The module consisted of 12 cylindrical Li-ion cells, and the studied PCM was Rubitherm's RT35HC. Other objectives included to study the components, configuration, and other basics of Li-ion batteries and battery thermal management systems (BTMS).

It was found that the performance and safety of Li-ion batteries are highly affected by internal and ambient temperatures. In worst scenario, increased temperature may lead to thermal runaway and even to an explosion. Thus, it is important to pay attention to the thermal behaviour of batteries. The temperatures can be controlled via BTMS. PCM has raised interest due to its low costs and simplicity. The working principle of PCM is based on its latent heat, the energy needed for the material to undergo a phase change.

The CFD model was developed successfully. PCM was found to delay the temperature rise of the module significantly. Simplified no-PCM case showed temperature increase over 28 °C compared to the module with PCM. Natural convection was captured successfully and was found to expedite the melting from the top. Thus, the PCM didn't maintain uniform melting in vertical direction. Results showed that only up to 50% of melting range, the PCM was effective for reducing the temperature rise. These results guide future studies on optimizing PCM based battery thermal management systems.

TIIVISTELMÄ

Lappeenrannan–Lahden teknillinen yliopisto LUT

LUTin energiajärjestelmien tiedekunta

Energiatekniikka

Ellinoora Veikkanen

Faasimuutosmateriaalin mallintaminen litiumioniakkumoduulin lämmönhallinnassa

Diplomityö

2026

92 sivua, 40 kuvaa, 7 taulukkoa ja 7 liitettä

Tarkastajat: Professori Jouni Ritvanen ja Professori Pertti Kauranen

Avainsanat: faasimuutosmateriaali, Li-ioni, akku, virtauslaskenta, lämpökarkaaminen

Diplomityössä tutkittiin faasimuutosmateriaalin lämpökäyttäytymistä akun lämmönsäätelyjärjestelmänä. Tavoitteena oli kehittää virtauslaskentamalli (CFD) ja tutkia materiaalin vaikutuksia sekä mahdollisen luonnollisen konvektion esiintymistä. Moduuli koostui 12 sylinterimäisestä Li-ioni akusta ja tutkittu faasimuutosmateriaali oli Rubithermin RT35HC. Muut tavoitteet sisälsivät Li-ioni akkujen komponenttien, toimintaperiaatteen, sekä muiden perusteiden, että akkujen lämmönsäätelyjärjestelmien tutkimista.

Tuloksien mukaan Li-ioni akkujen toiminta ja turvallisuus ovat tiukasti riippuvaisia sisäisestä sekä ympäristön lämpötilasta. Pahimmassa tapauksessa korkeat lämpötilat voivat johtaa lämpökarkaamiseen ja jopa räjähdykseen. Siksi on tärkeää kiinnittää huomiota akkujen lämpökäyttäytymiseen. Lämpötiloja voidaan hallita akkujen lämmönsäätelyjärjestelmillä. Faasimuutosmateriaali on kerännyt huomiota sen alhaisen hinnan ja yksinkertaisuuden takia. Materiaalin toiminta perustuu sen latenttilämpöön, eli energiamäärään mikä tarvitaan aineen faasimuutokseen.

CFD-malli kehitettiin onnistuneesti. Tutkitun materiaalin huomattiin hidastavan moduulin lämpötilan nousua merkittävästi. Yksinkertaistetussa tapauksessa ilman faasimuutosmateriaalia lämpötila nousi yli 28 °C enemmän verrattuna materiaalia sisältävään tapaukseen. Luonnollinen konvektio saatiin mallinnettua onnistuneesti ja sen huomattiin nopeuttavan sulamista moduulin yläosassa. Tämän takia faasimuutosmateriaali ei sulanut tasaisesti pystysuunnassa. Tuloksista huomattiin, että faasimuutosmateriaali oli tehokas hidastamaan lämpötilan nousua vain 50 %:iin asti materiaalin sulamisalueesta. Nämä tulokset toimivat lähtökohtana faasimuutosmateriaaliin perustuvien akun lämmönsäätelyjärjestelmien optimointia käsitteleville tutkimuksille.

ACKNOWLEDGEMENTS

I would like to thank my examiners, Professor Jouni Ritvanen and Professor Pertti Kauranen, for their valuable insights and guidance throughout this thesis. I am also grateful for the opportunity to conduct this thesis as a part of Flexible Clean Propulsion Technologies project, and the financial support provided by Business Finland.

Most of all, I would like to thank my fiancé, Vikke. Thank you for believing in me even in the moments where I doubted myself. Thank you for your endless support, advice and encouragement throughout this thesis and throughout the years. Your faith in me has meant more than words can express. I could not have completed this journey without you by my side.

I am also deeply grateful to my family, and especially to my parents. Thank you for always believing in me and encouraging me to pursue my dreams. Your constant support, guidance and encouragement have given me the confidence to move forward even in the challenging moments. I would not be where I am today without your love and support.

SYMBOLS AND ABBREVIATIONS

Roman characters

A_{m}	mushy zone constant	
c_{p}	specific heat capacity	J/(kgK)
H	enthalpy	J/kg
h	convective heat transfer coefficient	W/(m^{2}K)
I	current	A
k	thermal conductivity	W/(mK)
L	latent heat	J/kg
L_{c}	characteristic length	m
n	direction	
p	pressure	Pa
Q	heat generation rate	W
q''	heat flux	W/m^2
T	temperature	K
t	time	s
U	voltage	V
V	terminal voltage	V
v	velocity	m/s

Greek characters

β	thermal expansion coefficient	1/K
ε	emissivity	
λ	liquid fraction	

μ	dynamic viscosity	kg/(ms)
ρ	density	kg/m^3

Constants

g	gravitational acceleration	9.81 m/s^2
σ	Stefan-Boltzmann constant	5.67e-8 $W/(m^2K^4)$

Dimensionless

y	numerical coefficient

Subscripts

A	anode
aveg	averaged
C	cathode
conv	convection
k	variable
Li	lithium
l	liquid
n	direction
oc	open circuit
pcm	phase change material
rad	radiation
ref	reference
s	solid

sf	surface
∞	surroundings

Abbreviations

BEV	Battery Electric Vehicle
BTMS	Battery Thermal Management System
CFD	Computational Fluid Dynamics
EV	Electric Vehicle
GCI	Grid Convergence Method
GHG	Greenhouse Gas
LCO	Lithium Cobalt Oxide
LFP	Lithium-Iron-Phosphate
LGPCM	Liquid to Gas Phase Change Material
LIB	Lithium-Ion Battery
Li-Ion	Lithium-ion
LMO	Lithium Manganese Oxide
LTO	Lithium Titanate
NCA	Nickel Cobalt Aluminium
NMC	Nickel Manganese Cobalt
PE	Polyethylene
PHEV	Plug-in Hybrid Electric Vehicle
PCM	Phase Change Material
PP	Polypropylene
SEI	Solid Electrolyte Interphase

SGPCM	Solid to Gas Phase Change Material
SLPCM	Solid to Liquid Phase Change Material
SSPCM	Solid to Solid Phase Change Material
TR	Thermal Runaway

Table of contents

Abstract

Acknowledgements

Symbols and abbreviations

Declarations

1 Introduction 11
2 Lithium-Ion Battery Packs 13
2.1 Configuration of Lithium-Ion Batteries 15
2.2 Working Principle of Lithium-Ion Batteries 17
2.3 Materials of the Components 19
2.4 Heat Generation 22
2.5 Effects of Temperature 23
2.6 Thermal Runaway 24
3 Thermal Management 27
3.1 Heat Transfer 27
3.2 Battery Thermal Management Systems 29
3.2.1 Active Management 30
3.2.2 Passive Management 32
4 Phase Change Material 37
4.1 Categorization by Phase Change 38
4.2 Solid-Liquid Phase Change Materials 39
5 Thermal Modelling Approaches 42
5.1 Modelling of Lithium-Ion Battery 42
5.2 Modelling of PCM 43
5.3 Alternative Modelling Software 46
5.4 Recent Studies on PCM 47
6 Modelling Setup 50
6.1 Case Description 50

6.2 Setup for Software 54
6.3 Grid Independence Study 58
7 Results & Discussion 63
7.1 Model Verification 77
7.2 Sources of Error 80
8 Conclusions 82
References 85

Appendices

Appendix 1. Experimental setup, no PCM

Appendix 2. Correlations for determining the convective heat transfer coefficient

Appendix 3. Approximate and extrapolated relative errors of two finest grids

Appendix 4. Maximum temperatures of each cell

Appendix 5. Cell Temperatures with and without PCM with longer simulation time

Appendix 6. Thermal image, experimental

Appendix 7. Experimental study

DECLARATIONS

Turnitin

The originality of this thesis has been reviewed with the Turnitin similarity checking service.

AI usage

The author of the thesis, Ellinoora Veikkanen, used the following AI-tools during the preparation of the thesis:

1. Copilot
    a. Purpose of use: troubleshooting CFD -simulations, grammar checking and refining the language
    b. Explanation of the use of the tool: As challenges were encountered during modelling, the problem was simply explained to Copilot, and suggestions to fix the problem were asked. Some of the suggestions were implemented. Grammar checking and refining the language was limited to individual sentences, and only slight revisions were made without directly copying the suggestions of Copilot.
2. Claude AI
    a. Purpose of use: troubleshooting CFD -simulations
    b. Explanation of the use of the tool: As challenges were encountered during modelling, the problem was simply explained to Claude AI, and its suggestions to fix the problem were asked. Some of the suggestions were implemented.

Responsibility

The author, Ellinoora Veikkanen, takes full responsibility for the content of this thesis and has reviewed and edited the content generated by the possible use of AI tools.

1 Introduction

For the last 150 years, human activities have caused greenhouse gas (GHG) emissions to increase significantly in the atmosphere (EPA 2026). This has caused global temperatures to rise, reaching 1.1 ℃ above the 1850–1900 levels during 2011–2020 (IPCC 2023). The main sources of the emissions are from the continued use of fossil fuels in transportation and in heat and electricity production (EPA 2026). Batteries are one of the many technologies that help to mitigate further global warming as they provide an alternative, more environmentally friendly energy source for vehicles, and energy storage for intermittent wind and solar power. When batteries are used in electric vehicles (EVs), they can significantly reduce the GHG emissions of land-based transport (IPCC 2023).

A widely used battery type is the Lithium-ion (Li-ion) battery. They have many advantages, such as high nominal voltage, cycle life and good performance, and are therefore used in most handheld devices (Warner 2024). Individual battery cells can be connected to form a battery module to increase power and energy supplied, and the modules can be further connected to form a whole battery pack that could be utilized, for example, in EVs (Liu H. et al. 2017).

The overall utilization of Li-ion batteries has grown sixfold between 2020-2025, which is mainly due to increasing implementation of EVs and energy storage, contributing to over 70% and 15% of all applications, respectively (IEA 2026). Even though Li-ion batteries are generally safe, they possess a risk of thermal hazards (Tukes 2026). As studied by Sun T. et al. (2025), this refers to a chain-reaction known as thermal runaway (TR), where the temperature of the battery increases to a hazardous level and can even lead to an explosion. This could be caused by too high ambient or internal temperatures, as Li-ion batteries generate internal heat during charging and discharging phases. The growing demand and applications highlight the importance of the safety of Li-ion batteries.

The thermal conditions of a Li-ion battery can be controlled via battery thermal management system (BTMS). These can be divided into active and passive cooling methods, of which passive cooling with phase change materials (PCMs) has been a promising technology due to its low costs and high latent heat (Sun T. et al. 2025; Warner 2024). A composite phase change material has even been found to limit the temperature rise of a Li-ion battery cell in

a nail penetration test so effectively, that it prevented hazardous thermal runaway (Wilke et al. 2016).

Sutheesh et al. (2024) studied different thermal management systems for Li-ion batteries. They found that PCM alone does not have efficient enough thermal conduction to maintain optimal operating temperatures for batteries. However, enhanced with, for example, metal fins or additives, it provides better heat transfer and maintains the cell temperature below the required level at low charge rates. This highlights the importance of studying the heat transfer in PCM and optimizing the battery thermal management systems, thus ensuring the safety of the battery.

The objectives of this thesis include understanding the basics of Li-ion batteries, their configuration, working principle, materials, and how they generate internal heat. In addition, this thesis will discuss how heat and external temperatures affect the battery's performance, and how the temperatures of a battery pack can be controlled with different thermal management systems.

The main objective of this thesis, however, is to understand how phase change material affects the temperatures of a Li-ion battery module as a thermal management system. PCMs are usually combined with other thermal management systems to improve the cooling efficiency, but this thesis studies battery thermal management based solely on pure PCM. More specifically, the focus of this thesis is on how the melting process proceeds, how it affects the module temperatures, and does natural convection occur and what effect would it have on the melting. The behaviour of the material will be studied by completing a three-dimensional numerical study for a specific PCM. The model is based on an actual setup of a lithium-ion battery module, consisting of 12 cylindrical lithium-ion battery cells. The cells are surrounded by the PCM and thus in direct contact. The principle of numerical modelling and previous studies conducted for a PCM-based BTMS will be discussed.

2 Lithium-Ion Battery Packs

Lithium-ion batteries (LIBs) can be found in most of the devices we use. They are highly utilized as they possess many advantages compared to other commercial batteries (Li Y. et al. 2017). As explained by Warner (2024), Li-ion batteries have a higher cycle life, meaning that they can be charged/discharged more times compared to other typical batteries and have lower self-discharging rates. Low self-discharging rate refers to capacity loss when the battery is not used and can be either permanent or reversible. However, as Warner (2024) has mentioned, the most important advantage of Li-ion batteries is their higher voltage. The nominal voltage of Li-ion batteries is 3.2–3.8 V, as in other batteries the nominal voltage is typically only in the range of 1.2–2 V. In addition, Li-ion batteries have good reliability, lightweight structure, high energy and power density, available materials, and a wide operating temperature range, which will be discussed later in this thesis (Zubi et al. 2018; Li Y. et al. 2017).

For different applications, there are different types of battery cells, and lithium-ion batteries mainly include cylindrical, pouch and prismatic cells (Warner 2024). This thesis focuses only on cylindrical cells. Additionally, Warner (2024) describes that batteries can be divided into primary and secondary batteries. The secondary refers to rechargeable batteries, which this thesis will focus on. In secondary batteries, the electrochemical reactions are reversible, meaning the battery can be recharged. Batteries can have different chemistries, which all influence the performance, the possible application, lifetime and the number of possible charges of the battery. These chemistries are discussed in more detail in Section 2.3.

Liu H. et al. (2017) noted, that one battery cell can only provide a limited amount of power and energy, and thus single cells can be connected to form a module. These modules can further be connected to form a battery pack. The connections of a single cell can be either parallel or series connections and the cells and modules are connected through electric wires. Warner (2024) explains that in a parallel connection, current flows through all the batteries at the same time, thus increasing the energy and capacity of the module. In this case, the capacity is the sum of capacities of the individual battery cells, but the voltage remains unchanged. In series connections, on the other hand, the voltage is increased, but the capacity remains unchanged. The parallel and series connections are illustrated in Figure 1.

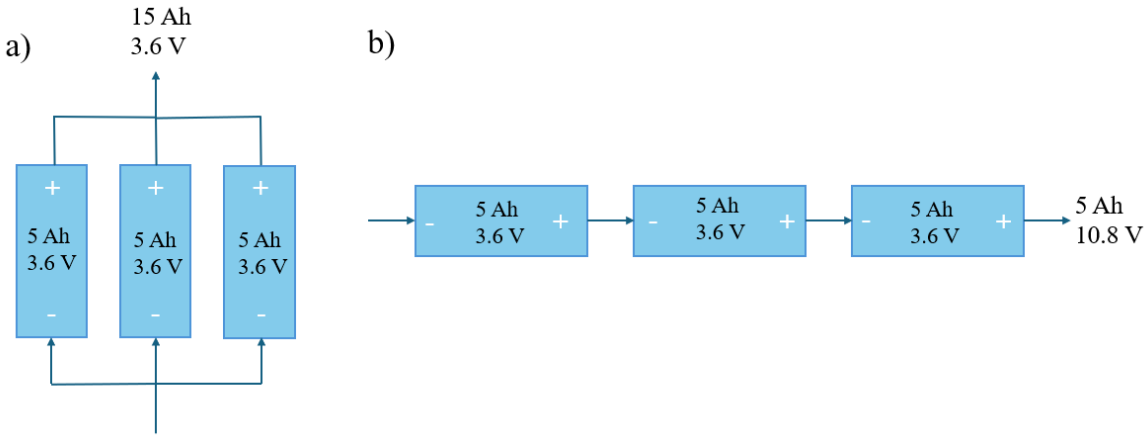


Figure 1. Different types of battery connections a) Parallel connection; b) Series connection (Redrawn from Warner 2024)

Liu H. et al. (2017) noticed in their study that the utilization of Li-ion batteries in EVs draws attention to the generated internal heat. With larger battery packs, more power is produced for the vehicle, but also more heat is generated. Besides the size of the pack, also fast charging/discharging processes increase the amount of heat generated. In battery packs, it is crucial that the heat dissipates effectively throughout the whole pack. Otherwise, accumulated heat and variating heat transfer creates temperature differences between the cells and thus negatively affects the pack's performance and safety. The effects of temperature will be discussed in more detail in later sections.

Figure 2 represents two important factors associated with batteries, state of charge and depth of discharge.

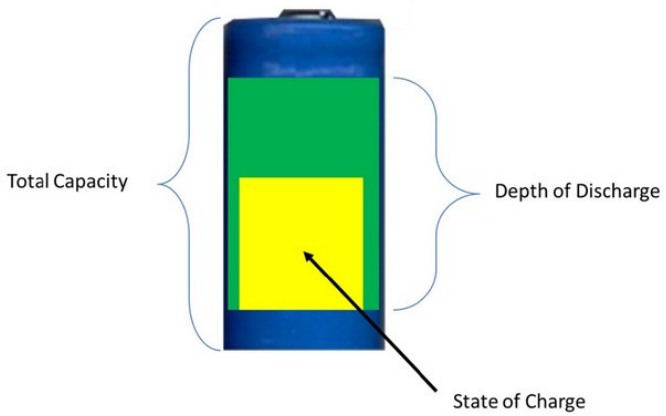


Figure 2. The state of charge and depth of discharge (Warner 2024)

As Warner (2024) describes, the battery's performance can be described through a state of charge (SOC) and depth of discharge (DOD). The state of charge describes how much energy

is utilized at a specific time. The depth of discharge describes, on the other hand, the amount of energy that can be utilized from the battery. For example, Li-ion batteries tend to operate around 10–90% of the battery's overall energy, to prevent too low and high charges. Illustrative fractions of DOD and SOC from the whole capacity of a battery can be seen in Figure 2.

Another important factor when speaking of batteries is the charge rate (C -rate), which describes the ability of the battery to charge in an hour. For example, 1C rate takes one hour, 2C rate takes 30 minutes to charge and, on the contrary, a smaller value than 1C would mean a charge time longer than an hour.

In the subsections, the configuration and working principle of a Li-ion battery are discussed. In addition, the most used materials of different components, heat generation, the effects of ambient temperatures, and the meaning of thermal runaway are discussed.

2.1 Configuration of Lithium-Ion Batteries

In a Lithium-ion battery (LIB) there are many different components, which all have a meaningful role in the performance of the battery. The components of a LIB include anode, cathode, current collectors, separator, housing and electrolyte (Liao et al. 2019; Warner 2024). The configuration is presented in Figure 3.

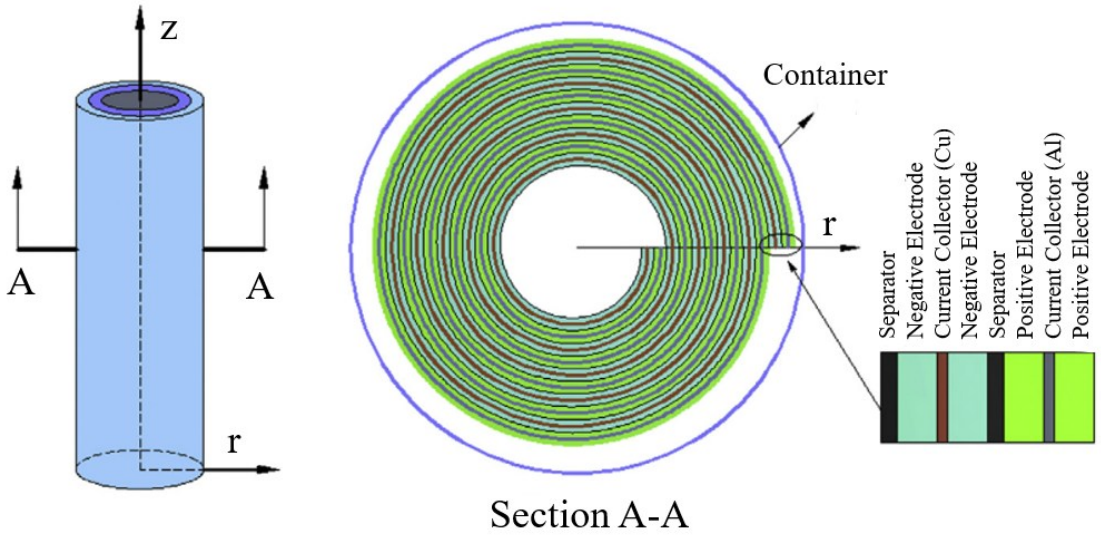


Figure 3. Configuration of a cylindrical Li-ion battery (Yang T. et al. 2016)

In a Li-ion battery, the cathode is considered as the positive end, and the anode, consequently, is considered as the negative end (Warner 2024). As described by Liao et al. (2019), the cathode and anode consist of current collectors which are covered by their specific active materials. The current collectors collect electrons and migrate them to an external circuit (Finkelstein et al. 2024). As Liao et al. (2019) has explained that the anode and cathode are collectively called electrodes, and between them lies the separator. The separator plays an important part in the performance of a Li-ion battery by preventing short-circuiting, i.e. the anode and cathode from touching. Otherwise, it would lead them to react with each other and short circuit.

As studied by Warner (2024), components of a Li-ion battery also include a container and the electrolyte solution. The anode, cathode, and separator, or as referred to as “jelly roll”, are placed in the container. The electrolyte solution is put into the container and thus the jelly roll is immersed into it. The electrolyte allows the migration of Li-ions between the cathode and anode, and can have several different additives mixed in it, all affecting the cell’s properties differently. It is important to note here, that the electrolyte is only conductive for Li-ions, not for electrons (Finkelstein et al. 2024). The working principle and more specific materials of these main components are discussed in the next sections.

2.2 Working Principle of Lithium-Ion Batteries

The precise working principle of a LIB is a complex process which includes different chemical reactions. In this thesis, the working mechanisms are only handled in a simple manner to keep the overall view of the topic clear. The basic working principle of a LIB is presented in Figure 4.

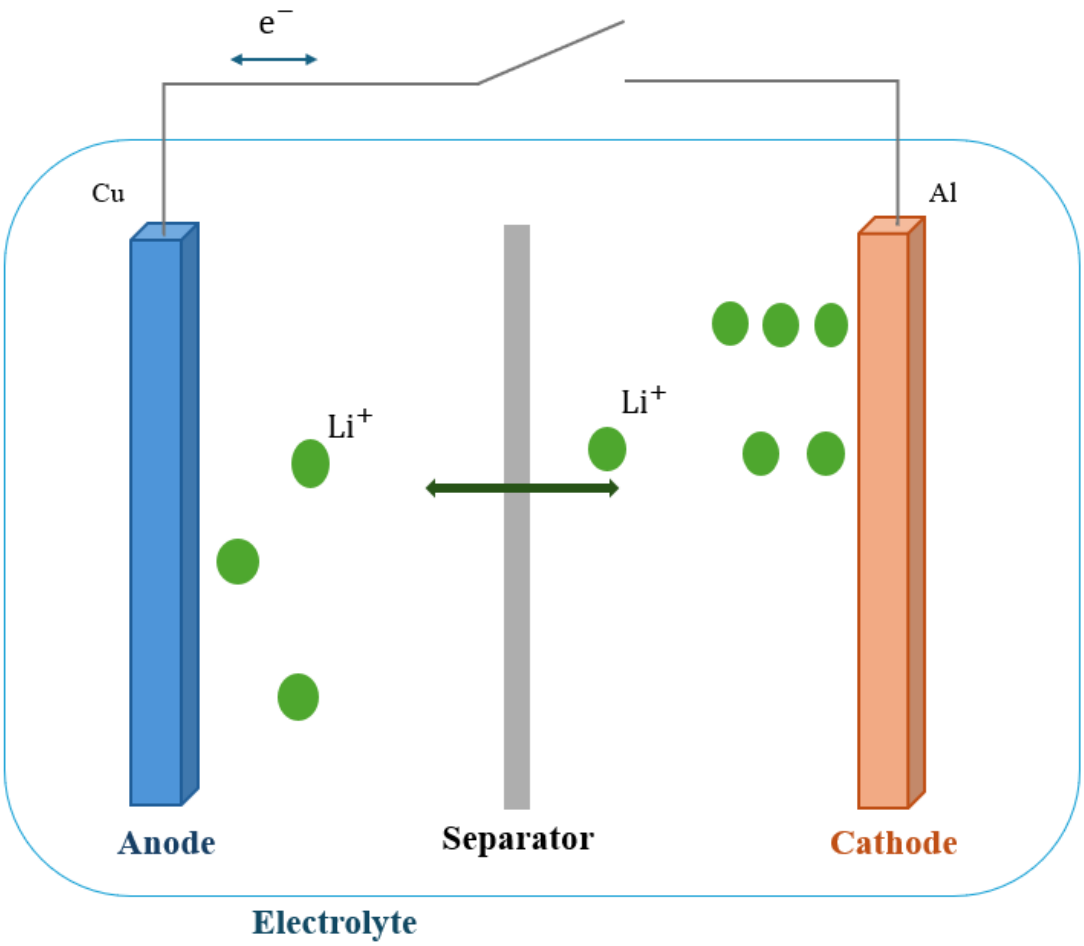


Figure 4. The working principle of Li-ion battery (Adapted from Goodenough & Park 2013)

In their study, Etacheri et al. (2011) has examined the chemical reactions taking place in the Li-ion battery. They include oxidation/reduction and intercalation/deintercalation reactions at the electrodes. The first phase of a Li-ion battery is always charging. The reversible oxidation and delithiation reactions of a cathode, i.e. losing electrons and Li-ions, can be described as follows, using lithium cobalt oxide (LCO) as an example of the active material of a cathode. The reaction can be expressed as in Equation (1).

$$\mathrm{LiCoO_2} \rightleftharpoons \frac{1}{2}\mathrm{Li^+} + \frac{1}{2}\mathrm{e^-} + \mathrm{Li_{0.5}CoO_2} \quad (1)$$

At the same time, an anode's active material experiences reduction and lithiation, i.e. it receives electrons and Li-ions. As will be discussed in Section 2.3, graphite is a highly used material as the anode's active material, and the ability of a graphite to store Li-ions is described as intercalation (Liu C. et al. 2016). Using graphite as an example of the anode's active material, the reversible intercalation of lithium in the anode can be described as in Equation (2).

$$\mathrm{C_6} + \mathrm{Li^+} + \mathrm{e^-} \rightleftharpoons \mathrm{LiC_6} \quad (2)$$

Finkelstein et al. (2024) has studied the reactions and movement of Li-ions in precise detail. In a discharge phase of a Li-ion battery, the Li-ions move through the electrolyte and separator from the anode to cathode. This discharge process happens spontaneously as the ions are attracted to the cathode, which has stronger bonding abilities for Li-ions than the anode. This reaction is irreversible and called to happen "energetically downhill", as the ions move from higher energy to lower. More precisely, the Li-ion is formed when the Li-atom goes through an oxidation reaction in the discharging process, and an electron is released. However, the electrolyte and the separator impede the electrons from migrating through them. Thus, the electrons must circulate through an external circuit. There they release the energy gained from the reaction, which creates power for the device being used. The migrating Li-ions then bond to the active material of the cathode, going through a reduction reaction and consuming electrons from the external circuit. The formed Li-atoms intercalate to the cathode's chemical structure, between atom layers. Consumption of the electrons enables electrical neutrality, which is mandatory for solids.

The charging process of a Li-ion battery needs an external voltage applied for the reactions to happen in the opposite direction as Finkelstein et al. (2024) has described. This is because the cathode possesses such a strong bonding ability for lithium, thus the reactions do not happen spontaneously. When the voltage is applied, and it exceeds the strength of the bond of Li-ions, they are released back to the electrolyte, where they are attracted by the anode. In the reaction, also the electrons are pushed out of the cathode into the external circuit and forced into the anode by the applied voltage.

As Liu C. et al. (2016) explains, a battery's performance is highly dependent on the anode and cathode, but also the electrolyte. The potential difference between cathode and anode determines the working voltage, i.e. the open circuit voltage. It can be described as follows in Equation (3)

$$V_{\mathrm{oc}} = \frac{K_{\mathrm{A}} - K_{\mathrm{C}}}{e} \tag{3}$$

The e refers to the magnitude of the electronic charge, and K_{A} and K_{C} refer to the chemical potentials of anode and cathode, respectively. In addition to the potential difference, the electrolyte's electrochemical properties also affect the working voltage. Besides this, the cathode's active material can be a limiting factor for the battery's performance. The capacity of the active material to store Li-ions, along with the discharge potential, determines the energy density of the battery. The anode materials usually provide higher capacity for storage.

2.3 Materials of the Components

In Li-ion batteries, different lithium compounds are used as the active material of the cathode and are often referred to as Li-ion chemistries. A lithium compound is needed to supply lithium-ions to the anode's active, non-lithium-containing material during the first charging phase (Passerini et al. 2020). These chemistries should obtain a high oxidation-reduction potential to confirm better capacity and higher output voltage for the battery (Liao et al. 2019). The most widely used chemistries are listed by Warner (2024), and they include lithium-iron-phosphate (LFP), nickel-manganese-cobalt oxide (NMC), lithium-cobalt oxide (LCO), lithium-manganese oxide (LMO), and lithium-nickel-cobalt-aluminium oxide (NCA). Warner (2024) also notes that of these cathode chemistries, the most used is the LFP. It has a high power density, and because of the good availability of iron and phosphate, it has low costs. Therefore, LFP has been used widely in the automotive sector. However, LFP chemistry needs additional carbon additives to enhance its electrical conductivity, which decrease LFP's already low energy density (Passerini et al. 2020). As Warner (2024) states, another chemistry that is suitable for long range vehicles is NMC. It has higher voltage and energy density, which could be increased even higher by modifying the proportions of the nickel, manganese and cobalt. On the other hand, it holds higher costs, depending on the

proportions of the high-cost cobalt. Likewise, the LCO has higher costs, containing mainly only cobalt. Although LCO is widely used in handheld devices, it cannot withstand high temperatures and can enter thermal runaway at lower temperatures than other chemistries, at only 130°C. Conrad (2023) has described that the NCA chemistry is similar in safety features to the NMC, and the main difference is between aluminium and manganese. Also, in the NCA chemistry, cobalt increases the costs, and thus the nickel covers up to 80% of the composition, with minimized use of cobalt. Compared to the NMC, the NCA has even higher energy density, better fast-charging abilities, but decreased thermal stability due to high nickel content, which can lead to thermal runaway occurring at 65°C in overcharging. The NCA chemistry has shifted from portable devices to the automotive sector and is highly utilized by Tesla (Warner 2024).

There are many options and ongoing research for the anode's active material in Li-ion batteries. The most widely used material has been graphite (Passerini et al. 2020). However, the need for higher power and energy densities of better performing Li-ion batteries has created a need for development of the anode's materials (Sun C. 2019). Warner (2024) noted that several different chemistries and materials have been studied for anode material, such as carbon nanotubes, tin, silicon, and even lignin-based hard carbon. Also, one other promising chemistry has been lithium-titanate oxide (LTO), but due to its lower energy density and higher costs, it has not yet reached wide utilization. However, graphite has many advantages, which include that it is easy to handle, it has low costs, has good reversibility abilities considering the intercalation of Li-ions, and it generates a solid electrolyte interphase (SEI). Graphite seems like a good option even when considering the following restrictions, Liao et al. (2019) has stated. These restrictions include that the active material of the anode should not prevent the formation of SEI, and it should not be permanently affected by the migration of Li-ions. It should also have good electrochemical stability and low oxidation-reduction potential.

Warner (2024) has described in detail the SEI layer. It is a passivation layer which is formed through reactions between the electrolyte and the graphite during the first charge of the battery. Formation of SEI can be seen as beneficial, as it doesn't allow electrons to pass through, and thus prevents further, harmful, reactions from happening between the anode and the electrolyte (Passerini et al. 2020; Warner 2024). On the other hand, the formation of SEI consumes lithium-ions, and thus causes irreversible capacity loss for the battery. In

addition, as the battery operates, the SEI layer can become unstable and continue growing, which can either block the electrode or even pierce through the separator and thus cause a safety hazard (Tomaszewska et al. 2019).

Liao et al. (2019) explains that the current collectors in Li-ion batteries are usually made of aluminium (Al) or copper (Cu). In a Li-ion battery, Al is often used on the cathode side, as the cathode operates at higher potentials than anode, and Al can tolerate these potentials better (Liao et al. 2019; Etacheri et al. 2011). Al is also more unstable at low potentials, as Li and Al experience alloying reactions, and thus, it is not usually utilized for the anode side (Zhu et al. 2020). In addition, Liao et al. (2019) describes that due to oxidation reactions, i.e. corrosion, a protective layer is formed on the surface of the Al. The layer prevents further oxidation reactions from taking place at the Al. Besides this, Al has good conductivity and relatively low costs. Like Al, Cu also has high conductivity and is usually chosen for the lower potential anode side, as it has lower oxidation potential. As Zhu et al. (2020) explains, Cu has higher costs than Al, but as mentioned, Al is unstable at the low potentials of the anode side. Also, Cu behaves more stably at the anode's low potentials, and dissolves at higher potentials. Therefore, when copper is used as current collector material, over-discharging should be avoided as it could increase the potential of anode side and thus lead to formation of Cu dendrites. The hazards of dendrite formation are discussed later in Section 2.6.

As aforementioned, the separator prevents the battery from short-circuiting and thus has an important role in securing performance. The separator is porous, usually a ceramic substance or plastic-based polyethylene (PE) or polypropylene (PP) (Warner 2024). Liao et al. (2019) noted that the separator is usually constructed as a combination layer, PP/PE/PP. This is done to prevent the internal short-circuiting, as the PE has a melting point of 130°C. In the case of slightly increased temperatures, the middle layer of the separator partially melts, blocking the pores and thus preventing the migration of Li-ions. However, PP also has a relatively low melting point, 165°C, which creates a challenge in the case of high temperatures. At temperatures exceeding 165°C, the separator melts entirely, exposing the anode and cathode, contributing to the internal short-circuit. The melting temperature of the separator is referred to as current-interruption temperature, and it should not be too low, or too high, ensuring good capacity, but also safety in the case of overheating.

The electrolyte acts as a conductive solution for the Li-ions moving between the anode and cathode, as aforementioned. The electrolyte can be liquid or solid, but in Li-ion batteries, usually organic liquid electrolytes are used, however they tend to be flammable (Passerini et al. 2020). As Liao et al. (2019) has explained, the electrolyte consists of lithium salts which can offer free lithium-ions and contribute to formation of the protective layer on the electrodes. These layers define the battery's properties, such as, operating temperature, capacity and energy density. The lithium salts can be, for example, LiPF6, LiAsF6 or LiClO4, of which LiPF6 is used most, but it possesses safety risks at temperatures over 60 °C (Passerini et al. 2020). In addition, the electrolyte contains organic solvent and the mentioned additives, which all affect the properties of the battery cell (Liao et al. 2019). The solvent can be, for example, dimethyl carbonate (DMC), propylene carbonate (PC) or ethylene carbonate (EC) (Passerini et al. 2020). Liao et al. (2019) also states few constraints for the organic solvent for Li-ion batteries, and one is that it must not be reactive with the materials of anode and cathode, as it could affect the battery's performance. Passerini et al. (2020) also describes that the electrolyte should have a wide temperature range, good thermal stability, and wide potential range, because of the differences at anode and cathode. It should also be noticed that the cost of the electrolyte directly affects the cost of the battery. As the charging and discharging, i.e. the movement of Li-ions, does not affect the electrolyte, its quantity can be minimized, which increases the energy density of the battery. In addition, because of the minimized quantity of electrolyte, it could be concluded that the cost of the battery would therefore decrease.

2.4 Heat Generation

As El Idi et al. (2021) has stated, the operating temperature and the internal heat generated in a Li-ion battery affect its performance. Moreover, the battery's lifetime can suffer from too high temperatures, and its operation can become unsafe. As explained by Pesaran (2002), the performance parameters that could be affected by internal temperature include power and energy available, the SOC, the resistances of the components and open circuit voltage. In battery packs, the accumulation of heat can lead to temperature differences along the module, thus affecting negatively the pack's performance. It is stated by Pesaran (2002) that the temperature differences should not exceed 5°C inside the pack.

The heat generation has been studied in detail by Sun T. et al. (2025). Heat is generated by different mechanisms in different components in a Li-ion battery, and the performance of the battery is highly dependent on the temperature. The heat is generated in the charging and discharging phases, and can be considered as two forms, reversible and irreversible heat generation. The reversible heat is generated through the reversible electrochemical reactions taking place at the electrodes. The irreversible heat generation can be further divided into ohmic heat and polarization heat. The ohmic heat can also be referred to as Joule heating (Liao et al. 2019). The ohmic heat is generated by the ohmic resistances of different components in the battery cell, as the electrons and Li-ions move through them. The polarization heat, on the other hand, is generated by gradients. These include the electrode reaction and ion diffusion rates, and the differences in the Li-ion concentrations between the electrodes. In addition, the formation of the SEI further increases the polarization heat, as it creates a gradient in the potentials.

To estimate the heat generated by the battery, the widely used Bernardi equation can be applied (Sun T. et al. 2025). The Bernardi equation accounts for the irreversible and reversible heat, takes thermal and electrical parameters into account and can be expressed as follows in Equation (4) (Bernardi et al. 1985).

$$Q = I(U - V) - IT\frac{\partial U}{\partial T} \tag{4}$$

On the right side of the equation, the first term corresponds to the irreversible heat generation and the last term to the reversible heat generation. In Equation 4, Q corresponds to the heat generation rate (W), I to the current (A), U and V to the open circuit voltage and terminal voltage (V), T to the battery temperature (K), respectively. The $\frac{\partial U}{\partial T}$ is called the entropy coefficient, and it is highly determined by the SOC (Sutheesh et al. 2024).

2.5 Effects of Temperature

Besides the internally generated heat, also external temperatures affect the battery's performance. The optimal operating temperature range for a Li-ion battery is from +10°C to +35°C (Warner 2024). A battery's aging may be accelerated if it operates at too high or too low temperatures, which makes temperature an important aspect to enhance the battery's life

(Sun T. et al. 2025). At normal operating temperatures, the only challenge with Li-ion batteries is the internal heat generated, as Liu L. et al. (2022) has explained. The risk of thermal runaway increases if the heat generated by the battery cannot dissipate effectively and thus accumulates inside or around the cell. The process of thermal runaway is discussed in the next section.

However, as Warner (2024) explains, Li-ion batteries can operate at temperatures exceeding this optimal temperature range. The operational temperature range refers to temperatures of -20°C to +45°C, where the Li-ion battery still operates, but may experience reduced capacity at the -20°C temperatures, as the electrolyte may begin to freeze. The loss of capacity caused by freezing is due to an increase in the internal resistances, which may further increase the internal heating of the battery and thus be harmful for the battery's performance (Liu L. et al. 2022).

As Warner (2024) stated, the operation of Li-ion batteries is still possible at -40°C to +60°C, although this range is called a survival temperature range. In this range, the battery's capacity will be reduced, and the overall operation at high temperatures can be unstable and unsafe, which will be discussed in the next subsection.

2.6 Thermal Runaway

Thermal runaway is a term used to describe a situation when external or internal factors cause a chain-reaction and causes the battery's temperature to accumulate to a hazardous level (Sun T. et al. 2025). Wang Qingsong et al. (2012) has described that the thermal runaway of a Li-ion battery is a result of the battery structure's decomposition in the case of increased pressure and temperature. These could be due to, for example, high charge or discharge rates or could be related to the flammability of the electrolyte. The increased temperature or pressure could result in the rupture of the materials, short-circuits and therefore possible ignition. In addition, if a battery cell enters the thermal runaway in a battery pack, it can cause the adjacent cells' temperatures to increase and thus cause them to enter the thermal runaway. The challenge with thermal runaway is its irreversibility and uncontrollability (Sun T. et al. 2025).

The causes of a thermal runaway process are described by Sun T. et al. (2025). Different external and internal factors can be the triggering cause for a battery to enter the thermal runaway stage. The causes are usually divided into thermal, mechanical, and electrical factors. Mechanical factors can include rupture of the materials or penetration, the electrical factors can be due to high discharging/charging, and the thermal triggers could be from the separator melting due to high temperatures. Depending on the triggering factor, differing chemical reactions take place in the battery, which will, nonetheless, accelerate heat generation and thus trigger the thermal runaway.

As Sun T. et al. (2025) has explained, overcharge and -discharge are classified as electrical triggering factors and they have been described as follows. The overcharge causes internal resistances of the battery to increase due to increased voltage and therefore generates more heat. In addition, lithium dendrites are formed because of a side reaction where excess lithium moves to the anode's side and therefore generates even more heat. The over-discharge, on the other hand, causes the voltage of the battery to become negative. In over-discharge the cathode's active material will begin to dissolve and copper dendrites will be formed which will eventually penetrate the separator and cause internal short-circuits in the battery.

As aforementioned, the temperature of the battery increases if internally generated heat cannot dissipate effectively. Passerini et al. (2020) states, that when the Li-ion battery temperature reaches 90°C, the protective SEI layer begins to decompose. This accelerates the reactions taking place between the anode's graphite and the electrolyte, thus further increasing the temperature, even up to 150°C.

Sun T. et al. (2025) has explained the process of thermal runaway. A temperature of 150°C triggers the thermal runaway and is a temperature where melting of the separator begins. Melting of the separator exposes the anode and cathode, thus accelerating short-circuit reactions and the temperature rises even further. These reactions release gas and even more heat. As a result, the temperature can increase even up to 400°C, which causes the electrolyte to burn and release rapidly a large amount of heat. The large amount of heat released could already rupture the housing of the battery and lead to an explosion. However, in the last phase of thermal runaway, the rupture of the housing is inevitable, and even combustion is possible as a large amount of heat is rapidly released due to a reaction of thermal runaway. In Figure 5, the process of thermal runaway is presented.

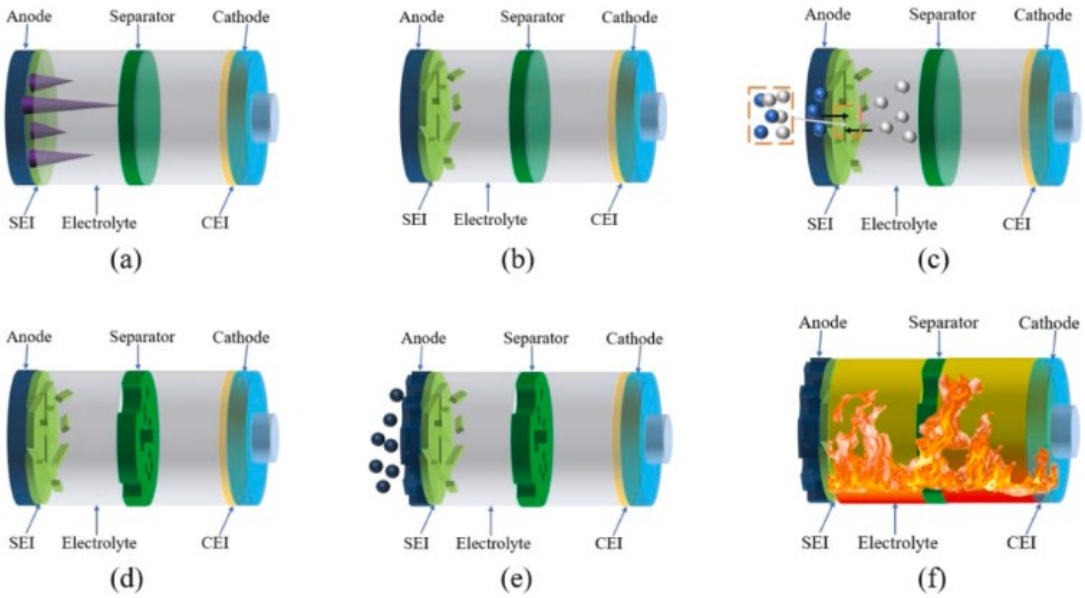


Figure 5. Thermal Runaway a) Formation of dendrites; b) Reactions with electrolyte; c) SEI decomposition; d) Melting of the separator; e) Anode material melts; f) TR and Combustion (Sun T. et al. 2025)

3 Thermal Management

In this section, the mechanisms of heat transfer within a battery and its surroundings are discussed. Along with these, the thermal management systems used for Li-ion batteries are studied and classified accordingly to their working principle.

3.1 Heat Transfer

Generally, heat transfer can happen by three different mechanisms, conduction, convection and radiation, which are presented in Figure 6.

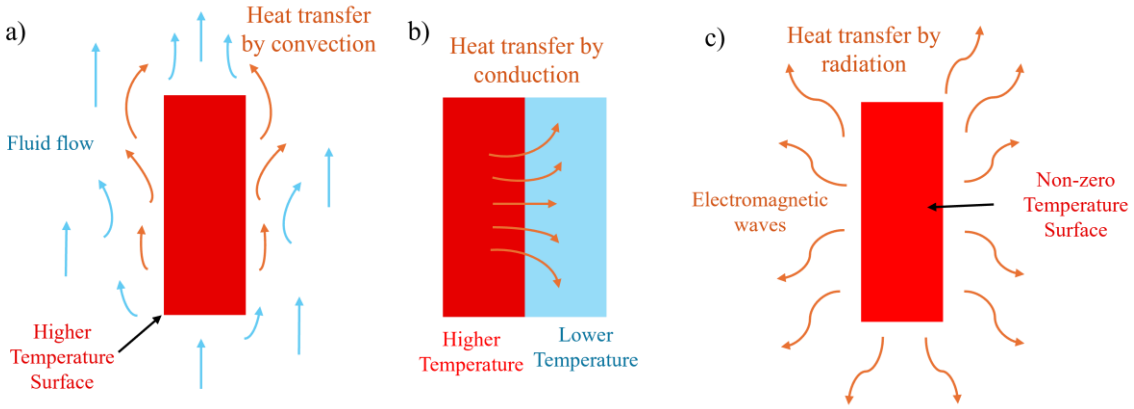


Figure 6. Heat transfer mechanisms a) Convection; b) Conduction; c) Radiation (Adapted from Sun T. et al. 2025)

As described by Incropera et al. (2007), conduction heat transfer is caused by movement and collisions of molecules and atoms of a substance. The energy transfers between the molecules and atoms from higher to lower energy contents. In a solid substance, the movement of the molecules and atoms causes the lattice to vibrate, which transfers the energy within the solid. Three-dimensional heat conduction is expressed in Equation (5).

$$q_n'' = -k\frac{\partial T}{\partial n} \tag{5}$$

Where q_n'' is the heat flux (W/m^2) in direction n, k refers to the thermal conductivity (W/(mK)), and $\frac{\partial T}{\partial n}$ is temperature gradient in direction n.

The phenomenon of convection is also described by Incropera et al. (2007). Convection takes into account random movement of molecules, but also uniform movement of a fluid, which then transfers the heat in the case of temperature differences between substances. Heat transfer by convection takes place between solid surface and a fluid flow, and forms two boundary layers between them, a thermal boundary layer and a velocity boundary layer. In the velocity boundary layer, the velocity of the flow varies between zero and the velocity of the flow, from the surface of the solid to the outer flow. The thermal boundary layer is formed when the solid has a differing temperature from the fluid. In the thermal boundary layer, near surface heat transfer takes place only through conduction as the velocity of the fluid is zero near the surface. However, convection can be either natural or forced convection. Natural convection refers to a heat transfer due to buoyancy forces of a fluid, which are affected by the density and temperature differences in the fluid. The forced convection, on the other hand, refers to a flow that is due to an external cause, for example, a fan or a pump.

Sun T. et al. (2025) noticed, that when considering a battery pack instead of a single battery cell, few aspects need to be considered in the heat transfer. The battery pack's layout and the shape of the surface impact the convection heat transfer. The smoother the surface of the pack is, the more effective natural convection takes place, and vice versa. Likewise, the layout of the pack impacts both natural and forced convection, however affecting more on the natural convection's efficiency. The heat transfer by convection can be expressed as in Equation (6) (Incropera et al. 2007).

$$q''_{\text{conv}} = h(T_{\text{sf}} - T_{\infty}) \tag{6}$$

Where q''_{conv} refers to the convective heat flux (W/m^2), h to the convection heat transfer coefficient (W/(m^{2}K)), T_{sf} to the temperature of the surface and T_{∞} to the temperature of the surroundings (K).

The last heat transfer form is radiation. As described by Incropera et al. (2007), every matter that has non-zero temperature, emits energy, i.e. thermal radiation, which is carried by electromagnetic waves. Thermal radiation does not need a medium to be transferred, unlike convection and conduction, and is due to the temperature differences between the matter and its surroundings. A heat flux that is emitted by a surface is expressed in Equation (7)

$$q''_{\text{rad}} = \varepsilon\sigma T_{\text{sf}}^4 \tag{7}$$

There, the σ refers to the Stefan-Boltzmann constant, which is 5.67e-8 W/m^2K^4, and ε to the surface emissivity.

3.2 Battery Thermal Management Systems

The temperature of the battery affects highly on the battery's performance and safety. For this reason, Battery Thermal Management Systems (BTMS) have an important role in the performance of the battery as they are designed to keep the battery's temperature at the desired operation temperature and to maintain the pack's internal temperature difference below the 5 °C (Liu L. et al. 2022). Effective thermal management can even extend a battery's life, as it delays aging which too high or low operating temperatures cause (Sun T. et al. 2025).

Warner (2024) explains that besides the management of high temperatures, thermal management systems can also be utilized as heaters. Heating could be needed in the case of low ambient temperatures, where the battery's performance begins to decrease due to the aforementioned freezing. However, low ambient temperatures are the only case where heating should take place. Because of the more significant safety hazards of high temperatures, this thesis will only focus on the management of high temperatures.

As described by Liu H. et al. (2017), the thermal management systems are divided into passive and active methods, based on whether the cooling needs external power. By the location of the needed heat removal, the management systems can be further divided into external and internal cooling systems. The external cooling systems refer to more traditional solutions and cover most of the currently utilized systems. In external systems, the heat is removed from the surface of the battery cell to the surroundings. As the internal heat generated by the battery affects its performance, also internal cooling systems have raised interest. These internal systems would be located inside the battery cell and could be realized, for example, as channels in the electrodes, where a coolant could flow and remove the heat (Mohammadian et al. 2015). However, the main challenge for the development of internal cooling systems is the closed housing of the batteries, which makes these harder to implement. Thus, this thesis will focus only on the external cooling systems. The division of thermal management systems can also contain a combination of the passive and active, a hybrid management system (Sun T. et al. 2025). The division is presented in Figure 7.

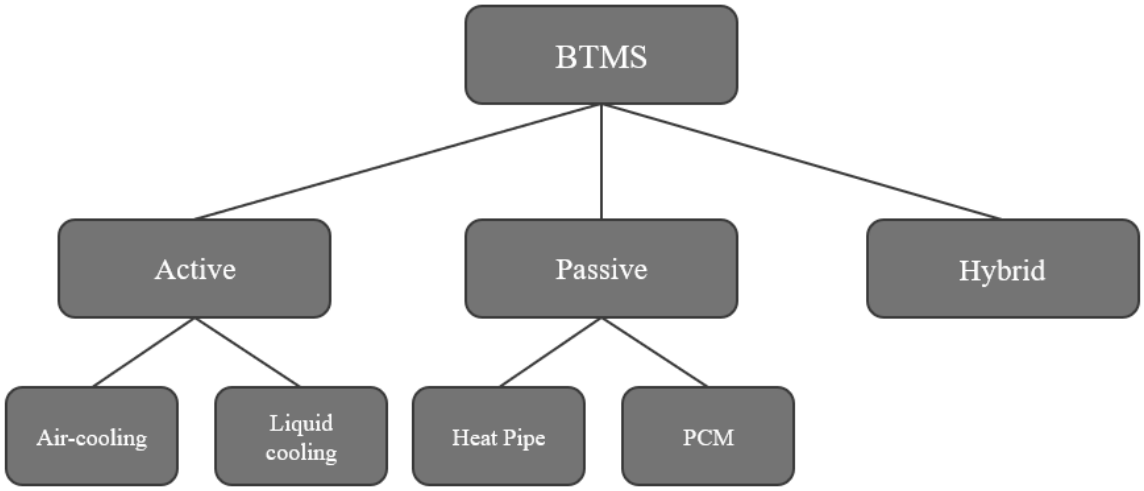


Figure 7. Battery Thermal Management System classification

As it can be noticed, the active and passive cooling systems are further divided into more specific cooling methods which will be discussed in the next subsections. In this thesis, the hybrid systems will not be discussed further.

3.2.1 Active Management

Liu L. et al. (2022) notes, that one of the most widely used active management systems is air-cooling. It has been widely utilized in electric vehicle applications, and its advantages include that it is simple by structure and thus lightweight, has low maintenance costs, it is safe and has good durability. Sun T. et al. (2025) has described that in the air-cooling systems, the main principle is that the air flows through the battery pack, carrying away the heat from the battery cells. In active air cooling, like in most active management systems, the heat transfer takes place mainly through forced convection. The convection can be accomplished, for example, with pumps or fans, which cause the air to flow. An active air-cooling system utilizing a fan is illustrated in Figure 8.

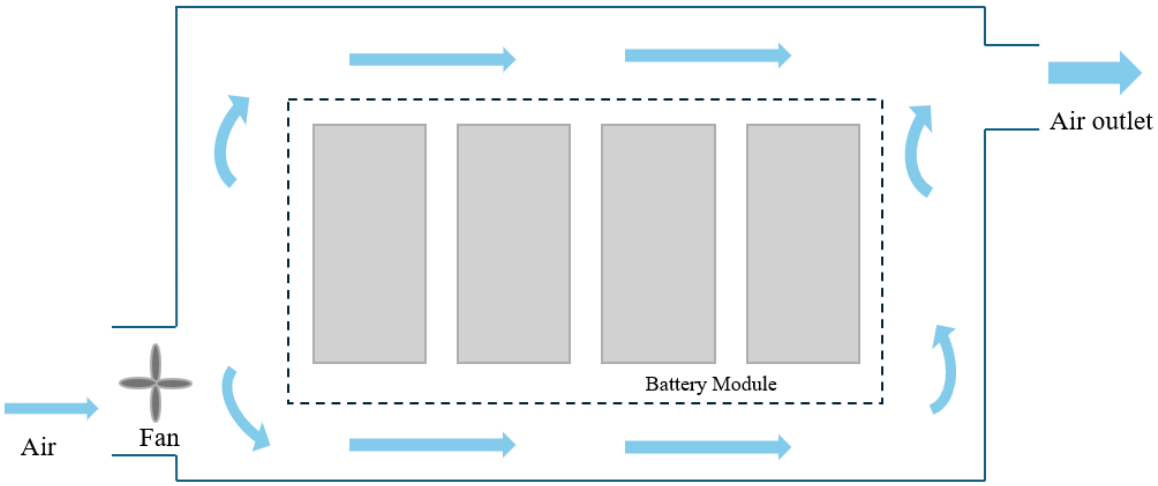


Figure 8. Active air-cooling (Adapted from Battery Design, 2022)

Despite the low costs, safety and durability, Warner (2024) states few disadvantages of the air-cooling system. Cooling the battery with only air is not as efficient as with liquids. Moreover, depending on layout, it may contribute to even higher temperature gradients inside the pack, as the cells at the beginning of the flow cool down more compared to the last cells the flow reaches. As mentioned in Section 3.1 of this thesis, the battery pack's design and layout may affect the convection heat transfer negatively. In addition, possible sealed housing for the battery pack could create a challenge for effective air cooling (Warner 2024).

Another active thermal management system used for battery packs is liquid cooling, and it is considered more effective (Sun T. et al. 2025). Despite its effectiveness, the liquid cooling system can increase the weight, complexity and costs of the system compared to the air-cooling system and can cause safety hazards due to possible leakage (Liu H. et al. 2017; Warner 2024). As described by Sun T. et al. (2025), liquid cooling can be realized either through direct or indirect contact, and likewise air-cooling, happens through forced convection. In liquid cooling, the circulating coolant can be, for example, water, oil, or ethylene glycol. One reason which makes liquid cooling more effective than air-cooling is that the coolants used for liquid cooling mainly have higher specific heat capacity and better thermal conductivity compared to air (Liu L. et al. 2022).

In a more specific manner, the liquid-cooling system can be realized through either by direct contact submerging, additional pipelines or cold plates, which are thin metal sheets where

the coolant circulates through inner channels (Wang Qian et al. 2016). The complexity of the liquid cooling system is due to these additional components and Sun T. et al. (2025) describes one possible configuration of indirect cooling as follows. Generally, in addition to a pipeline, there is a tank which is used to store the coolant. The coolant circulates in the pipeline due to an additional pump, which is considered as one of the main components of this system. There is also a cold plate that is used to transfer the heat from the battery to the coolant, and a heat exchanger that further transfers the heat from the coolant to the surroundings. A presentative figure of a possible liquid-cooling concept is illustrated in Figure 9.

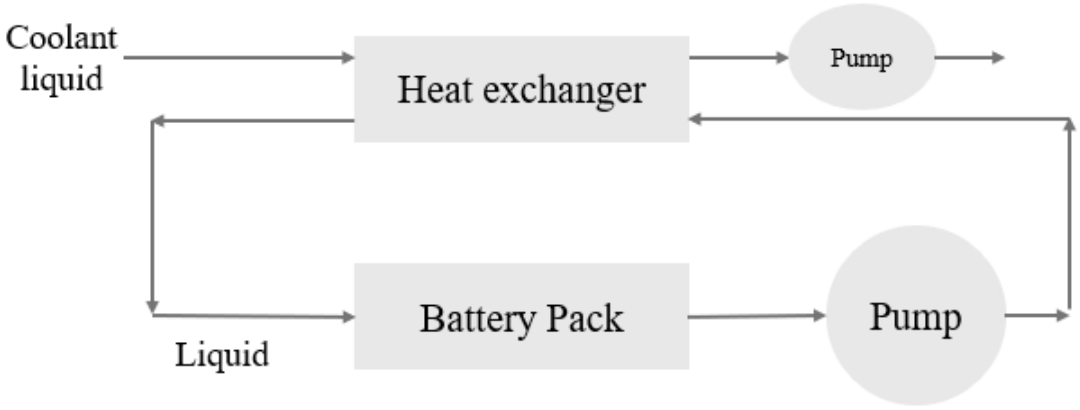


Figure 9. Active liquid-cooling (Adapted from Wang Qian et al. 2016)

Direct and indirect contact refers to the contact between the coolant and the battery, as explained by Liu H. et al. (2017). In direct cooling, the battery is immersed in the coolant fluid, which increases the cooling efficiency. This system requires the coolant fluid to be dielectric, which decreases the risk of short circuits in the battery (Tomaszewska et al. 2019). However, the power consumption of the system increases, as dielectric fluids are high in viscosity and need additional power to achieve sufficient flow rates. In indirect cooling, the coolant circulates through pipes, thus increasing the thermal resistance and decreasing the efficiency of the system. However, in this system the coolant does not need to be dielectric and thus can be lower in viscosity.

3.2.2 Passive Management

Because of the possible temperature gradients in air-cooling, complexity, increased costs and possible leakage of liquid cooling, more attractive, passive management systems have

been studied despite the better effectiveness of liquid cooling (Wilke et al. 2016). As explained by Sun T. et al. (2025), a passive thermal management is a system that does not require external power and is mainly based on natural convection and conduction. Besides the advantage of not needing additional power and thus lower costs, the passive management systems are also easily maintained and have high reliability. Despite these advantages, they may face challenges in controlling the temperature during rapid changes in load and temperature.

As described by Sun T. et al. (2025), air-cooling can also be considered as a passive method. This passive air-cooling refers to the natural flow of air, simultaneously cooling the battery. This system could be realized, for example, as a car driving and, due to the speed, air flows through gaps in the battery pack. The drawback of passive air-cooling is that it is only capable of decreasing the temperature of battery to the temperature of the environment, which may not be efficient enough to hinder the heat accumulation (Warner 2024). The passive air-cooling method is illustrated in Figure 10.

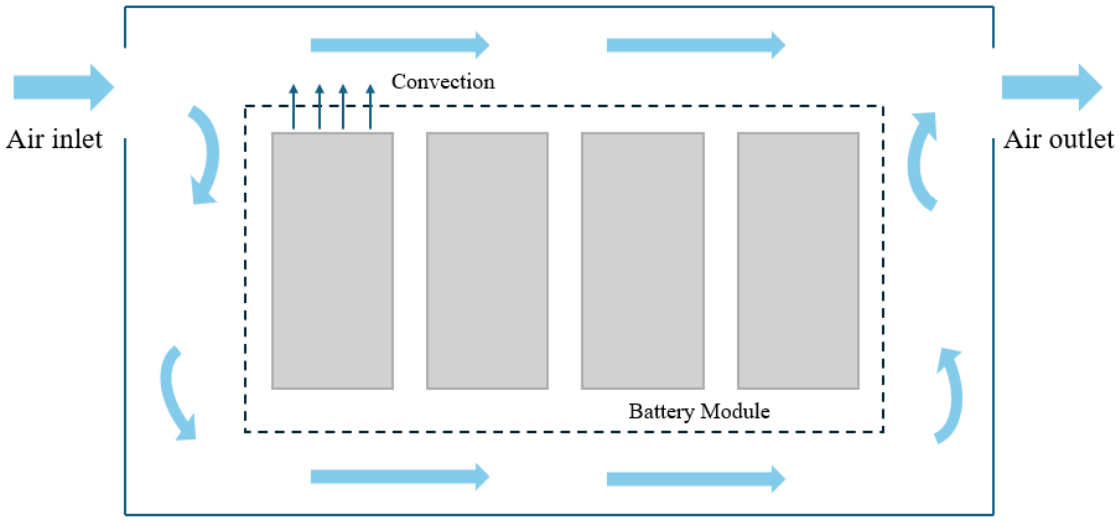


Figure 10. Passive air-cooling

As Liu H. et al. (2017) states, other passive thermal management systems utilize phase change phenomena. There the energy required for the material to change its phase, for example, from liquid to gas, is utilized to absorb heat from the battery. One highly used passive thermal management method based on the phase change is a heat pipe system (Sun T. et al. 2025). Sun T. et al. (2025) and Liu H. et al. (2017) have described the heat pipe

system in detail. The heat pipe system consists of evaporation, condensation and adiabatic sections, which evaporation is in contact with the battery. In the evaporation section, the circulating liquid evaporates to vapor from the heat obtained from the battery's surface, thus experiencing a liquid-vapor phase change. The vapor transfers through the adiabatic section to the condensation, meaning no heat is lost between evaporation and condensation sections. In condensation, the vapor experiences a vapor-liquid phase change, releasing the heat absorbed from the battery and condensing into liquid. Due to gravity or capillary effects, the liquid then circulates back to the evaporation section. This natural circulation of the liquid, however, does not need external power, and thus can be categorized as passive management. The working principle of the heat pipe system is presented in Figure 11.

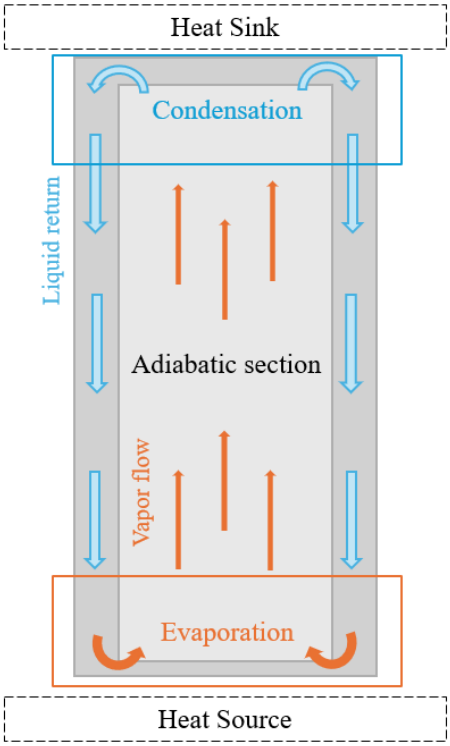


Figure 11. Configuration of Heat Pipe system (Adapted from In-Taek et al. 2023)

As Warner (2024) has explained, other thermal management systems that rely on phase change are phase change materials (PCM). The PCM works on the same principle as the liquid in the heat pipe system; the PCM is, for example, in solid state, and when it absorbs the heat from the battery, it starts to melt. The PCM does not need to converge into liquid entirely, nor is it preferable due to possible leakage challenges and thus safety hazards, but moreover, it softens due to absorbing the heat from the battery, which eventually dissipates into the surroundings (Warner 2024; Liu L. et al. 2022).

PCM based thermal management has been described by Warner (2024). The effectiveness of the PCM management system is based on the high demand for energy for the material to undergo a phase change, meaning the material can absorb large amounts of heat. Like other passive management systems, also PCM has reduced costs compared to more complex active management systems but suffers from limitations. Even though PCM can absorb large amounts of heat before melting, it cannot effectively dissipate the heat after achieving fully melted phase. In addition, Chen J. et al. (2019) highlights the importance of the material properties, such as melting point, latent heat and thermal conductivity, but also the configuration of the system, such as the thickness and structure of the PCM. Even though PCM does not need any additional devices or space, the weight of the battery pack might be increased.

It has been experimentally studied by Wilke et al. (2016) that an optimized PCM effectively dissipates the heat from battery cells and even prevents thermal runaway from propagating. In the experiments, air and PCM filled battery packs were compared and a nail penetration test conducted. The PCM filled battery pack showed lower temperature peaks and prevented the propagation of thermal runaway. The safety of the pack with PCM was significantly increased compared to the pack with only air which reached higher temperatures and the thermal runaway occurred instantaneously in the case of short circuits occurring. In Figure 12, the concept of PCM is presented.

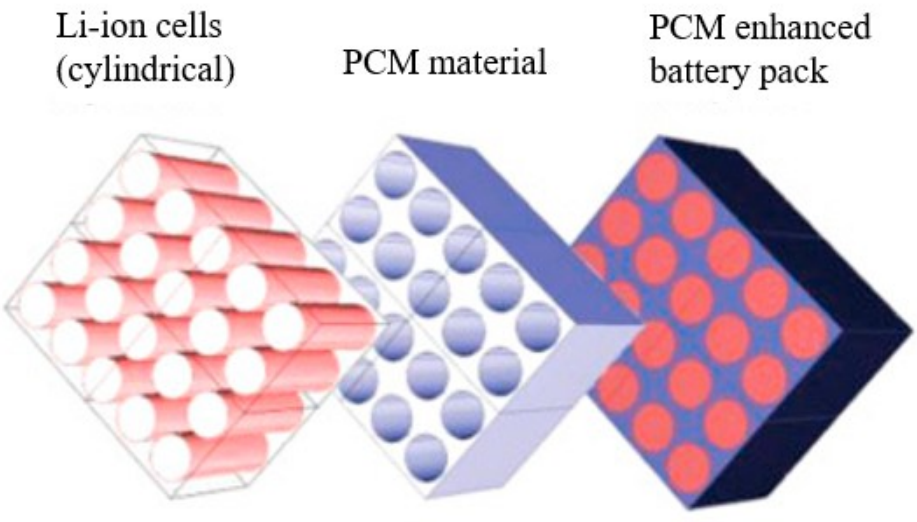


Figure 12. PCM battery thermal management system (Wang Qian et al. 2016)

Bianco et al. (2022) also found PCM based thermal management systems to reduce the temperature peaks and maintain the temperature distribution more even. The PCM based systems thus provided more stable performance of batteries, and when combined with active cooling methods, could improve the cooling efficiency and maintain the operating temperature at optimal levels.

4 Phase Change Material

As mentioned in Section 3.2.2 of this thesis, the working principle of the phase change material is based on the material's latent heat, the energy needed for the material to undergo a phase change. As described by Rubitherm (2026), the phase change material absorbs heat from a specified source, and utilizes it to change its phase, for example from solid to liquid, after reaching its melting temperature. Before the PCM has fully changed the phase, the temperature remains mainly constant as shown in Figure 13. After the phase change is accomplished, the temperature keeps increasing and eventually dissipates into surroundings as the material begins solidification.

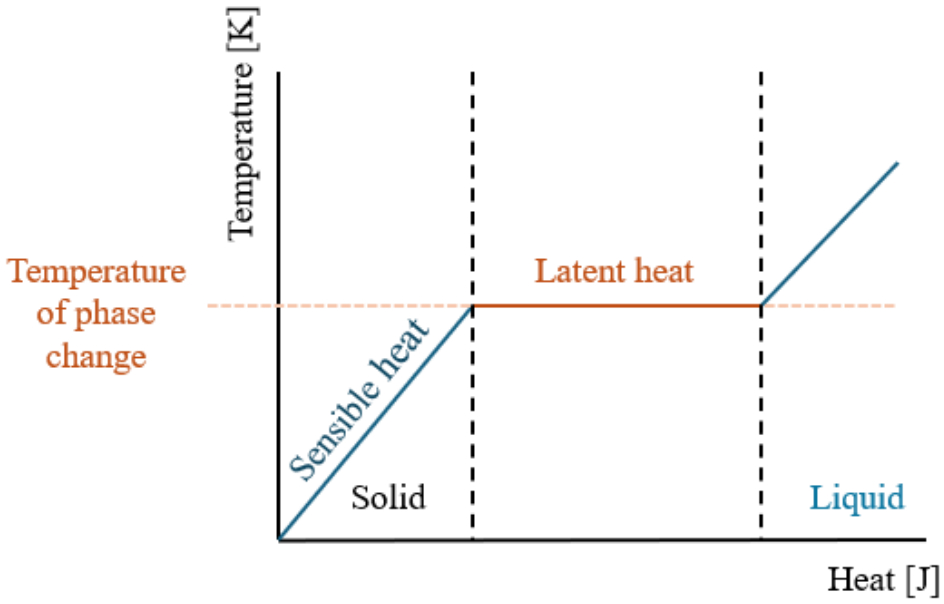


Figure 13. Working principle of PCM

The phase change materials can be categorized into high and low temperature ranges according to the applications, as Zhang et al. (2022) has described. For high temperature PCMs, the melting range of the phase change material lies between 120°C to 850°C, and the applications can be, for example, solar power generation or low-temperature engines. For the low-temperature PCMs, the melting range of phase change material lies between 0°C to 120°C, and the application can be, for example, thermal management of battery or heat recovery. In addition, there are sub-zero PCMs which can be utilized at low temperatures, for example in cold storage applications (Yang L. et al. 2021). The PCM studied in this thesis

is a low temperature PCM, and further categorization of the phase change materials can be done based on the type of phase change.

4.1 Categorization by Phase Change

Phase change in materials can occur from solid to liquid (SLPCM), solid to gas (SGPCM), solid to solid (SSPCM), or liquid to gas (LGPCM) (Zhang et al. 2022). While the other phase change categories are self-explanatory, solid-solid PCMs undergo changes in their crystal structure rather than melting or vaporization (Gulfam et al. 2019). Of these categories, mainly SSPCMs or SLPCMs are utilized in battery thermal management systems, as varying gas production causes challenges in the materials containing a gas phase change (Zhang et al. 2022). However, the LGPCMs have been studied as a BTMS and has been noticed in some cases to have better heat dissipation abilities than convection through liquid (Liu H. et al. 2017). Nevertheless, the PCM studied in this thesis is categorized as solid to liquid material (SLPCM), and thus the focus will be on them. Figure 14 presents the possible phase changes.

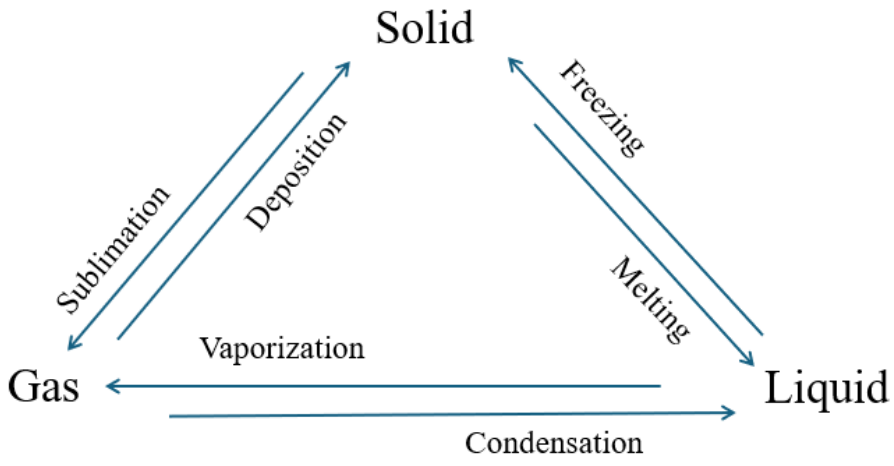


Figure 14. Phase Changes

However, Zhang et al. (2022) has stated few advantages of the SSPCM worth mentioning. The SSPCMs have small changes in the volume of the material, long lifetime and high thermal efficiency. On the other hand, the SSPCM possesses higher costs and lower latent heat. The most common phase change materials are SLPCMs, and thus generally, when speaking of PCM based thermal management, it refers to SLPCMs (Liu H. et al. 2017). Like

the SSPCMs, the SLPCMs are also popular due to their low volume changes, but also due to their good controllability and thus are the most used phase change materials (Chen J. et al. 2019). This thesis will only focus on SLPCM, which will be discussed in more detail in Section 4.2.

4.2 Solid-Liquid Phase Change Materials

The solid to liquid phase change materials can be further divided into organic and inorganic materials and as a mixture of those, eutectics (Chen J. et al. 2019). In this thesis the focus will be on organic and inorganic materials. The categorization of solid to liquid phase change materials is presented in Figure 15.

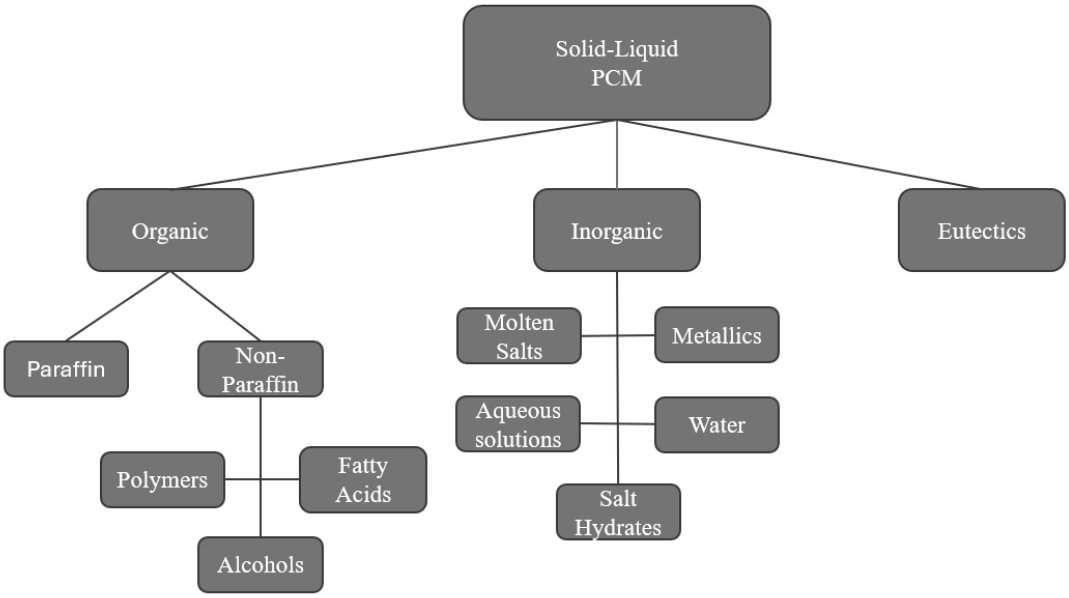


Figure 15. Categorization of Solid to Liquid Phase Change Materials

The inorganic phase change materials include water and other aqueous solutions, salt hydrates, and molten salts (Chen J. et al. 2019). On the other hand, Sharma R. et al. (2015) divides inorganic PCMs also into metallics, which, along with salt hydrates, are highly utilized in solar energy applications. Even though metallics have high thermal conductivity, they pose many challenges in the application, for example, increased weight (Sharma A. et al. 2009).

As Sharma R. et al. (2015) have studied, the inorganic materials have a good ability to maintain their latent heat even after many melting and freezing periods, and have better thermal conductivity than organic materials, around 0.5 W/(mK). However, inorganic materials, especially salt hydrates, melt unevenly (Sharma A. et al. 2009; Sharma R. et al. 2015). Sharma A. et al. (2009) explains that the melting process of the salts refers to the hydration and dehydration. This dehydration is the cause for the uneven melting, as water released in the melting process is inadequate to dissolve the solid salt entirely and causes further differences in density.

The organic materials include paraffins, organic acids or as referred as fatty acids, alcohols, and polymers, of which paraffin is mostly used in battery thermal management systems with solid-liquid phase changes, and thus will be later discussed in more detail (Chen J. et al. 2019; Sharma R. et al. 2015; Gulfam et al. 2019). Paraffins, fatty acids, and alcohols are highly flammable, but fatty acids possess higher cost than paraffins (Sharma R. et al. 2015).

As Kim et al. (2018) describes, the SLPCM is usually initially in a solid form and directly in contact with the battery. The PCM is manufactured so that it can be applied directly into the battery module. In some applications, there can be plates assembled on the sides of the PCM, which transfer the heat more effectively.

The phase change process of a SLPCM has been described by Chen J. et al. (2019). Because of the internal heat generation of a battery, the temperature of the battery increases. The heat accumulated to the surface then transfers through conduction through the PCM, which starts to melt after reaching its melting range. However, before reaching the melting point, the PCM has absorbed the heat in the form of sensible heat, after which it absorbs heat at a constant temperature, and the melting starts (Kim et al. 2018). Lastly, the heat will eventually dissipate to the surroundings from the PCM via convection and conduction.

The paraffin materials, which are most used in SLPCMs, are straight chain alkanes (Sharma A. et al. 2009). Zhang et al. (2022) has described that the requirements for paraffin, or other solid-liquid phase change materials include a suitable melting point and operating temperature, suitable latent heat, it must be environmentally friendly and non-toxic, non-flammable and have low costs. As Chen J. et al. (2019) states, paraffin meets most of these requirements and is therefore the most suitable option for battery thermal management systems. Moreover, other advantages stated by Sharma A. et al. (2009) include paraffin’s

reliability and safety, its performance is easy to predict, and it doesn't cause corrosion. As mentioned in the previous section, the SLPCMs mainly have low changes in volume, and it is also true in the case of paraffin materials. In addition, paraffins can act stably even up to temperatures of 500°C.

Despite the many advantages of paraffins, as aforementioned, there is a possibility for leakage in the case if the paraffin melts entirely. This causes loss of the phase change material and possible environmental damage, which is why it should be a non-toxic material (Chen J. et al. 2019). Even though one of the requirements of SLPCMs was non-flammability as aforementioned, in many cases paraffins can be flammable, if they are not modified with different additives (Sharma A. et al. 2009).

As examined by Chen J. et al. (2019), most of the SLPCM's, even paraffins, possess low thermal conductivity which causes challenges at high temperatures and currents. The improper dissipation of heat from the battery will promote thermal runaway eventually, and therefore, the thermal conductivity of the SLPCMs needs to be optimized. The thermal conductivity of a paraffin can be only in the range of 0.1-0.3 W/(mK) (Sharma R. et al. 2015). However, it can be enhanced by adding different additives, for example, carbon fibre, nanoparticles or metal mesh, to mention a few (Zhang et al. 2022). A paraffin based PCM management system usually has relatively long melting and freezing periods (Sharma A. et al. 2009).

Considering the requirements and challenges of PCM, the choice of the material is an important factor when developing a PCM based BTMS. The wanted performance of PCM depends on the application and needs to be considered carefully, as discussed by Ali (2024). Different additives can be added to the material to change the performance or, as mentioned, to enhance the thermal conductivity of it. In addition, fins can be added to the system to increase the heat transfer area and therefore enhance the thermal performance of the system.

5 Thermal Modelling Approaches

To predict the behaviour and the melting process of the PCM as a BTMS for Li-ion battery, a three-dimensional numerical model is developed. The principles of CFD (computational fluid dynamics) modelling for a Li-ion battery module and a PCM will be presented in the next subsections. In addition, alternative modelling software and previous studies on PCM are discussed.

The modelling of the PCM as a battery thermal management system for the Li-ion battery pack will be implemented with commercial, graphic-based CFD -software Ansys Fluent 2024, where the Melting and Solidification model is available. Modelling of a Li-ion battery and PCM also requires the conservation of energy, mass and momentum to be considered to formulate governing equations, and the initial and boundary conditions of the model to be formulated (Sutheesh et al. 2024). In the next subsections, the governing equations for the Li-ion battery and for the PCM are presented respectively. However, the heat transfer by radiation is neglected in this study due to it being insignificantly low.

5.1 Modelling of Lithium-Ion Battery

In this thesis, the modelling of the Li-ion battery is made in a simple manner, and thus few assumptions are made to keep the model computationally manageable. The battery cell's heat generation is assumed to be steady, and the thermophysical properties are assumed to be uniform and invariable over time (Sutheesh et al. 2024).

The heat transfer in a battery cell takes place mainly through conduction due to the solid-solid and solid-liquid interfaces, and for a cylindrical cell, the heat conduction can be calculated by three-dimensional conduction equation (Sun T. et al. 2025; Peng et al. 2022). Thus, the energy conservation for the Li-ion battery can be expressed as in Equation (8).

$$\rho c_{\mathrm{p}} \frac{\partial T}{\partial t} = k\nabla^2 T + \dot{Q} \tag{8}$$

There ρ is the average density of the materials of the battery (kg/m^3), c_{p} the average heat capacity (J/(kgK)), T is the temperature (K), t is time (s), k is the average thermal

conductivity (W/(mK)) and $\dot{Q}$ refers to the volumetric heat generation rate, i.e. the heat generation approximated with Bernardi's equation (Equation 4).

Ling et al. (2015) explains that to decrease the computational costs of the model, a lumped capacitance thermal method could be utilized within the battery cell. As described by Incropera et al. (2007), the lumped capacitance method assumes uniform temperature across the solid, and thus temperature gradients could be neglected. In reality, this kind of condition could not exist, as it would require infinitely high thermal conduction. However, a uniform temperature can be assumed with low error, if the heat conduction within the solid is high compared to the heat transfer between the surface and the surroundings. Thus, the energy conservation equation for the battery would be formed as Equation (9).

$$\rho c_{\mathrm{p}} \frac{\partial T}{\partial t} = \dot{Q} \tag{9}$$

The suitability of the lumped capacitance method can be assessed through Biot number, as Incropera et al. (2007) has stated. Biot number provides a relation of heat transfer resistances; the resistance within the surface to the resistance of the surroundings. Biot number can be calculated with Equation (10).

$$Bi = \frac{hL_{\mathrm{c}}}{k} \tag{10}$$

Where the L_{c} is characteristic length. For the lumped capacitance method to be suitable, the following condition should be satisfied: Bi < 0.1.

5.2 Modelling of PCM

To accurately model the behaviour of the PCM, the conservation of energy, mass and momentum need to be considered, but also few assumptions need to be made due to the complexity of modelling the phase change material. The main challenges when modelling a PCM are related to the movement of the melting/solidification area, mushy zone, which is due to the melting, the changing properties and volume of the material and natural convection in the material (Zaynetdinov et al. 2024). Similarly to Sutheesh et al. (2024), this work considers the PCM as a Newtonian-fluid with its thermophysical properties depending

on temperature. Once the PCM has melted, the liquid flow is considered incompressible, laminar and unsteady.

Zaynetdinov et al. (2024) stated that when modelling phase change materials with CFD, natural convection cannot be ignored in the melting process. In addition, as the PCM's temperature varies, its density and volume also vary. As will be discussed later, a Boussinesq approximation is used for the density, but the changes in volume between solid and liquid will be neglected to minimize computational costs.

In Fluent, the solidification and melting processes, which are needed in the case of phase change material, are solved by the enthalpy-porosity method, as explained in Ansys Inc. (2026). The enthalpy-porosity technique is based on the iteration of enthalpy balance, where the computed factor is a liquid fraction, i.e. the fraction of a cell volume that is in liquid phase. In the enthalpy-porosity method, the interface of the liquid-solid is not tracked explicitly, but the liquid fraction is tracked in each cell. In the enthalpy-porosity method, a mushy zone is also considered, where the material is processed as porous and in momentum equations, sink terms are included. These sink terms are added, so pressure drops caused by the solid material's presence are considered. The mushy zone will be discussed in more detail later in this section.

Zaynetdinov et al. (2024) expressed the energy conservation equation for PCM as in Equation (11).

$$\rho_{\mathrm{pcm}} \frac{\partial h}{\partial t} + \rho \nabla \cdot (H\vec{\mathrm{v}}) = \nabla k_{\mathrm{pcm}} \nabla T \tag{11}$$

Where the $\vec{\mathrm{v}}$ is velocity vector (m/s), and H is the enthalpy (J/kg) and can be calculated with Equation (12).

$$H = H_{\mathrm{ref}} + \int_{T_{\mathrm{ref}}}^{T} c_{\mathrm{p,pcm}} dT + \lambda L \tag{12}$$

The λ refers to the liquid fraction of the PCM, and L to the latent heat (J/kg) of the PCM. The liquid fraction is expressed in Equation (13).

$$\lambda = \begin{cases} 0 & T < T_{\mathrm{s}} \\ \dfrac{(T - T_{\mathrm{s}})}{(T_{\mathrm{l}} - T_{\mathrm{s}})} & T_{\mathrm{s}} < T < T_{\mathrm{l}} \\ 1 & T > T_{\mathrm{l}} \end{cases} \tag{13}$$

Where the subscripts l and s refer to the melting and solidification, respectively. The liquid fraction of the PCM is 0, when the PCM is entirely solid, and vice versa 1 when it is entirely liquid (Sutheesh et al. 2024).

The conservation of mass, i.e. the continuity equation can be expressed as in Equation (14) (Sutheesh et al. 2024).

$$\nabla \cdot (\vec{\mathrm{v}}) = 0 \tag{14}$$

The conservation of momentum for PCM in liquid phase, i.e. Navier-Stokes equation, is expressed in Equation (15) (Zaynetdinov et al. 2024).

$$\rho \frac{\partial \vec{\mathrm{v}}}{\partial t} + \rho \nabla \cdot (\vec{\mathrm{v}}\vec{\mathrm{v}}) = -\nabla p + \mu \nabla^2 \vec{\mathrm{v}} + \rho\big(1 - \beta(T - T_{\mathrm{ref}})\big)\vec{g} - \frac{(1-\lambda)^2}{\lambda^3 + y} A_{\mathrm{m}} \vec{\mathrm{v}} \tag{15}$$

Where p is pressure (Pa), β is the thermal expansion coefficient (1/K), T and T_{ref} are the PCM temperature and the reference temperature, g is the gravitational acceleration 9.81 m/s^2, y is a numerical constant, and A_{m} is the mushy zone constant. As Zaynetdinov et al. (2024) studied, the behaviour of the PCM could be simplified by using the Boussinesq approximation. The approximation assumes constant density. However, the buoyance forces caused by temperature variations and the presence of a gravitational field are taken into account with the buoyancy term $\rho\big(1 - \beta(T - T_{\mathrm{ref}})\big)\vec{g}$ (Sutheesh et al. 2024).

The last term of the Equation (14) can be called as the volumetric force, which helps the solver to arrive at the solid phase more quickly, as it reduces the velocity based on the liquid fraction (Sutheesh et al. 2024; Zaynetdinov et al. 2024). The y in the volumetric force is a small number of 0.001 and is there only to prevent the volumetric force from becoming zero (Zaynetdinov et al. 2024).

The mushy constant is usually in the range of 10^4-10^7 (Al-abidi et al. 2013). High values of the mushy zone constant cause the velocities to drop to zero more quickly in the solidification process, but too high values can cause oscillation in the solutions (Ansys Inc. 2025). As the PCM melts, the temperature lies between the melting and solidification temperatures and is neither fully liquid nor solid in the zone, as Zaynetdinov et al. (2024) has described. This is called the mushy zone, where the liquid fraction is between 0 and 1, and the PCM is considered as porous material where the value of the liquid fraction refers

to the porosity. The mushy constant determines parameters of the phase change, such as rate of convection and gradients in velocity.

Thermophysical properties, such as thermal conductivity and specific heat capacity of PCM can be determined by its liquid fraction as shown in Equations (16 & 17) (Sutheesh et al. 2024).

$$k_{\mathrm{pcm}}(T) = k_{\mathrm{s}} + (k_{\mathrm{l}} - k_{\mathrm{s}})\lambda(T) \tag{16}$$

$$c_{\mathrm{p,pcm}}(T) = c_{\mathrm{p,s}} + \left(c_{\mathrm{p,l}} - c_{\mathrm{p.s}}\right)\lambda(T) \tag{17}$$

where the subscripts s and l refer to solid and liquid phase, respectively.

5.3 Alternative Modelling Software

In addition to Ansys Fluent, other software could be also utilized to model this kind of CFD-simulation study. One other commercial software is OpenFoam. It is a free and powerful software, with capabilities to model different types of fluid flow phenomena with customised specifications, as stated by OpenCFD Ltd. (2024a). The models made with OpenFoam include a wide range of applications, from for example, aerospace and automotive engineering to chemical engineering. At OpenCFD Ltd. (2024b) it has been explained that OpenFoam follows typical CFD simulation setups, which include the initial boundary conditions, specification of the geometry and its properties and, lastly, the tools and applications used. However, in OpenFoam, the setups are done as customized files, differing from the graphic-based Ansys.

Another suitable software for simulating complex phenomenon is COMSOL Multiphysics. In the software, various types of physical phenomenon can be modelled, including electrochemistry, fluid flow and heat transfer problems, as stated in COMSOL (2017). Likewise, Ansys Fluent also COMSOL is a graphic-based software, and it compiles and solves the required equations. COMSOL Multiphysics is capable of simultaneously solve multiple physical problems, and it is easy is to use, as the underlying equations and mathematics does not need to be defined by the user. With COMSOL, physical phenomenon of batteries could be accurately modelled. However, in this thesis the focus is on the

behaviour of the phase change material, and thus the modelling of electrochemical properties of the battery is secondary.

Another possibility to model PCM related simulations would be with simplified models. Zaynetdinov et al. (2024) studied a latent heat thermal energy storage modelled with CFD- and simplified process model implemented in MATLAB. They stated that the simplified process model would not solve the momentum equation for the PCM and thus, does not consider the natural convection in the phase change material, but captured the overall performance of the system more accurately. However, as it did not consider natural convection, the simplified process model was not accurate enough to model the behaviour of the PCM. Thus, the consideration of natural convection is crucial in the case of melting simulations, and CFD-modelling captures more accurately the behaviour of the phase change material. Another simplification that was implemented to the model was that the melting and solidification of the PCM was solved through the apparent heat capacity method, where the solidification and melting is considered by incorporating the latent heat into the specific heat over a temperature range around the melting point (Inkeri et al. 2022; Zaynetdinov et al. 2024).

As stated above, CFD -modelling captures the behaviour of the PCM more accurately than simplified process models. In CFD -modelling, the momentum equation is taken into account, and thus the natural convection is not neglected. Therefore, the CFD -model will be implemented in this thesis, to accurately capture the heat transfer phenomenon and natural convection inside the phase change material.

5.4 Recent Studies on PCM

As mentioned, the studies by Bianco et al. (2022) and Wilke et al. (2016), showed that phase change materials provide more stable temperature distribution throughout a battery cell, and can even prevent the thermal runaway from propagating. In the experimental study by Wilke et al. (2016), the studied PCM was a composite material, containing wax and graphite, and had thermal conductivity of 20 W/(mK). This is significantly higher than, for example, with pure paraffins, which have thermal conductivity of 0.1-0.3 W/(mK) as mentioned in Section 4.2.

Peng et al. (2022) have studied the thermal abilities of different phase change materials. In the study, a numerical model was created, and it examined a hybrid thermal management system, containing heat pipes and pipes with PCM between cylindrical Li-ion cells. The studied phase change materials contained pure paraffin wax and composites of it with different mass fractions of extended graphene. The study showed that melting of the PCM did not happen evenly, but the material melted first from the top due to natural convection. The results also showed that the pure paraffin wax did not have as efficient heat dissipation abilities as the composite PCMs due to its lower thermal conductivity.

Sutheesh et al. (2024), on the other hand, studied a PCM based thermal management system enhanced with fins. In the study, four different three-dimensional models were executed to study the thermal behaviour of a Li-ion cell at different C-rates. These models included a base case where only PCM surrounded the cylindrical cell and three cases where the PCM was enhanced with differently structured honeycomb-shaped fins. The study showed better thermal performance with the fin-based systems at 1C and 3C-rates, as the PCM based system couldn't provide sufficient thermal management anymore at 3C-rate. The fins were found to enhance the thermal behaviour of the system and thus provide more stable temperature distribution in the battery cell.

Huang et al. (2019) conducted a numerical study of PCM, studying its thermal behaviour as a thermal management system for a Li-ion battery pack. The model consisted of 25 aligned cylindrical Li-ion battery cells, and the empty space was filled with PCM. The PCMs studied included pure paraffin and composite material including paraffin and expanded graphene. This study analyzed the thermal properties of the PCMs and their effect on the performance of the battery pack and found that the composite PCM had a more efficient effect on the thermal performance due to higher thermal conductivity. However, natural convection was neglected in this study, and thus its effects on the melting behaviour were not captured.

Active air cooling has been compared to passive cooling in studies by Sabbah et al. (2008) and Chen F. et al. (2020). In both studies, the examined PCM was a composite material containing paraffin wax and graphite. In the study by Sabbah et al. (2008), it was found that at normal operating conditions, both of the cooling methods, passive PCM and active air-cooling at different flow rates, were equally efficient. However, under more stressful conditions, the PCM system was found to maintain more uniform temperature distribution along the pack, and the air-cooling was found to require flow rates of turbulent ranges to

provide sufficient cooling. The PCM also maintained the temperature below the safety limit, as the air-cooling could not do that without reaching the undesirable turbulent ranges. In the study by Chen F. et al. (2020), on the other hand, the active air-cooling with cooled air was found to maintain the temperatures below a safety point more effectively than PCM, but the PCM was found to maintain more uniform temperature distribution. However, in both studies natural convection was neglected, and only the energy conservation equation was applied for the PCM.

It is important to pay attention to the behaviour and thermal performance of PCM in the battery thermal management systems. This ensures better and safer operation of battery cells, pack, and the whole application. Many of previous studies have examined hybrid thermal management systems, comparing the effectiveness of PCM to active management systems. Few studies have paid attention to the thermal properties and behaviour of PCM, but these studies have either been experimental, or the natural convection has been neglected or the PCM has not been in direct contact with the cells. In this thesis, the empty volume in the module is filled with specific PCM, and thus it is in direct contact. The purpose of this thesis is to study and get a better understanding of the thermal behaviour of the PCM and to capture natural convection and assess its effects on the thermal behaviour of the Li-ion battery module.

6 Modelling Setup

This section describes the modelling setups. It includes the specifications of the Li-ion battery pack, PCM, case setup, and settings for Ansys Fluent, such as initial and boundary conditions. Additionally, a grid independence study will be conducted for the model.

The aim of the 3D model is to study how the PCM affects the temperature of the battery cell. The simulation will be run until the PCM achieves a liquid fraction of 1. The heat generation of battery cells is assumed to be constant as the focus is on the behaviour of the PCM throughout the whole melting period. In reality, there would be rest periods between the charges/discharges. This study focuses on a C-rate of 2C, which means that the battery would be fully charged within 0.5 h, as mentioned in Section 2. Another important objective of the simulation is to capture possible natural convection in the PCM and study how it affects the thermal behaviour of the Li-ion battery module.

6.1 Case Description

The Li-ion batteries studied are Molicel INR-21700-P45B (NCA) rechargeable batteries. More specific cell characteristics are presented in Table 1.

Table 1 Characteristics of Li-ion INR-21700-P45B cell (Molicel 2026)

Parameter		Value
Capacity (mAh)	Typical	4500
	Minimum	4300
Cell Voltage (V)	Nominal	3.6
	Charge	4.2
	Discharge	2.5
Charge Current (A)	Standard	4.5
	Maximum	13.5 (70°C cut-off)
Charge Time (h)	Standard	1.5
Discharge current (A)	Continuous	45 (80°C cut-off)
Temperature (°C)	Charge	0 – 60
	Discharge	-40 – 60
Energy Density (Wh/kg)	Gravimetric	242

Cell dimensions are presented in the Table 2.

Table 2 Li-ion cell dimensions

Parameter	Value
Diameter (mm)	21.55
Height (mm)	70.15
Weight (g)	70

The model is based on an actual setup according to Avik et al. (2025), as presented in Appendix 1. The battery module consists of 12 Li-ion INR-21700 cells, and the cells are connected with nickel strings in a 3p4s (3 parallel and 4 series) connection. The batteries are placed onto a 3D printed holder. PCM fills the container up to the height of the battery cells, leaving an empty space above. The container is from polypropylene material, with a wall thickness of 1.2 mm. However, in this thesis the setup is simplified due to computational costs. The battery or container details are ignored, as is the air gap between the battery cells and container lid. Therefore, only cells, container and PCM are modelled as illustrated in Figure 16. Figure 17 shows the dimensions of the module.

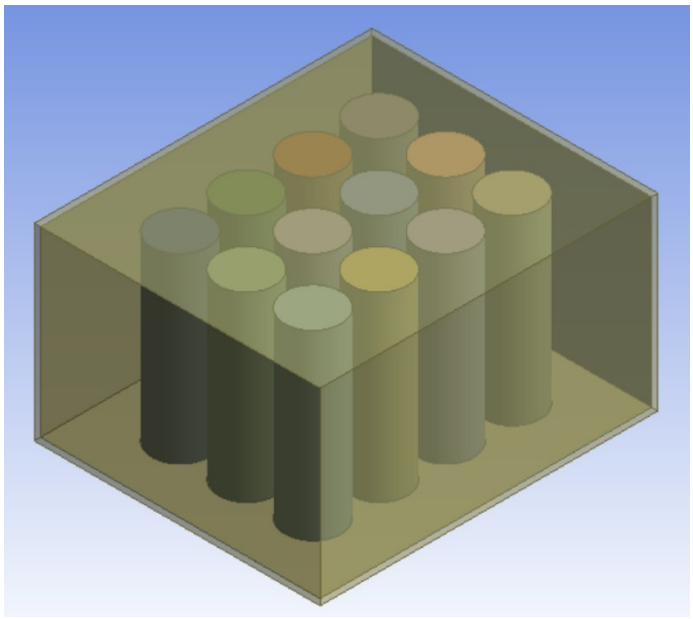


Figure 16. The battery module

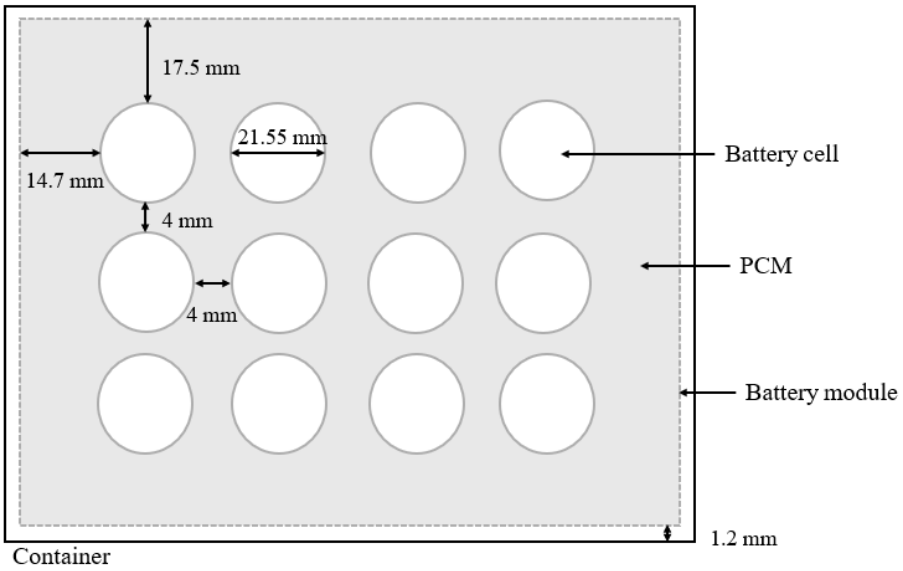


Figure 17. Dimensions of the module

The PCM examined in this thesis is Rubitherm's RT35HC phase change material. This material has a long lifetime, has no supercooling effect, and maintains an almost constant temperature during absorption and release of heat (Rubitherm 2020). More specific information of RT35HC is presented in Table 3.

Table 3 Specifications of RT35HC PCM

Parameter	Value
Melting area (°C)	34–36
Congealing area (°C)	36–34
Heat storage capacity (kJ/kg)	240
Specific heat capacity (kJ/(kgK))	2
Density solid (at 25°C) (kg/l)	0.88
Density liquid (at 40°C) (kg/l)	0.77
Heat conductivity (both phases) (W/(mK))	0.2
Max. operation temperature (°C)	70

However, the heat of fusion, i.e. the latent heat, in this study will be 186 kJ/kg based on experimental results conducted for the RT35HC phase change material (Avik et al. 2025).

In this thesis, only 1/4 of the whole module will be modelled to decrease computational costs. The modelled geometry is presented in Figures 18 and 19, of which Figure 19 is from top view. The results, however, will be presented for the whole battery module.

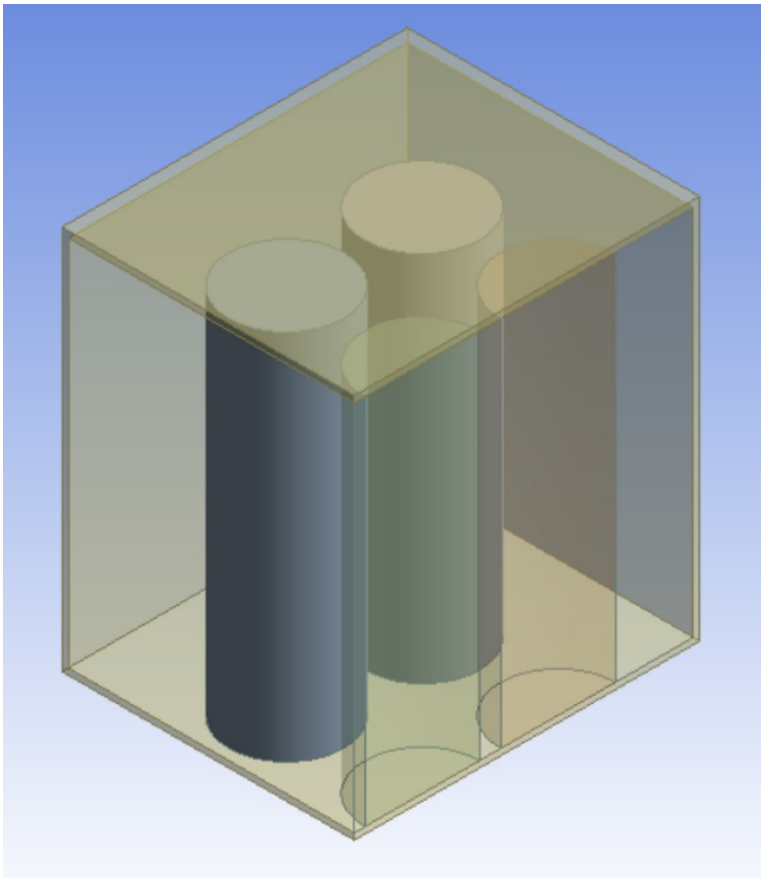


Figure 18. Geometry of the 1/4 module

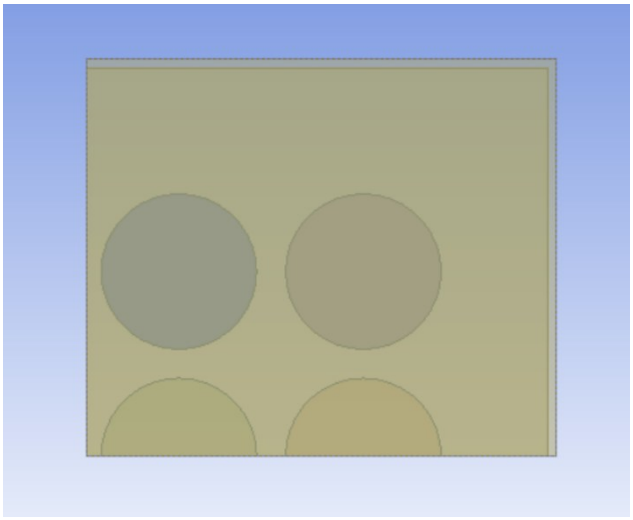


Figure 19. Top view of the model

To be able to utilize the Boussinesq approximation for the PCM, the following condition is required to be satisfied, $\beta(T - T_0) \ll 1$ (Ansys Inc. 2025). When validating this condition, the temperature T is the melting temperature of the PCM, 36°C, and the reference

temperature T_0 is the ambient temperature, 20°C. The thermal expansion coefficient β for PCM RT35HC is 0.000865 (Faden et al. 2017). Hence, $0.0138 \ll 1$ is obtained and the utilization of the Boussinesq approximation is validated.

6.2 Setup for Software

The simulation will be run as a transient, i.e. time dependent simulation and the solver type is selected as pressure-based. In addition, gravitational acceleration is taken into account by defining it in the general set-ups. In Ansys Fluent, the Energy equation is automatically set when the Solidification and Melting model is on. The mushy zone constant is left as default, which is 10^5. As stated in Section 5, in this study the flow is assumed to be laminar, and therefore the Viscous model in Fluent is set as Laminar.

The material properties used in this thesis are presented in Tables 4–6, first presenting the properties of the polypropylene container. The polypropylene properties are obtained as averaged values.

Table 4 Properties of polypropylene (Ashby 2021)

Parameter	Value
Density ρ_{pp} (kg/m^3)	900
Specific Heat $c_{\mathrm{p,pp}}$ (J/(kgK))	1950
Thermal Conductivity k_{pp} (W/(mK))	0.14

The used properties of the phase change material RT35HC are presented in Table 5.

Table 5 Properties of RT35HC

Parameter	Value	Reference
Density ρ_{pcm} (kg/m^3)	880	Rubitherm 2020
Specific Heat $c_{\mathrm{p,pcm}}$ (J/(kgK))	2000	Rubitherm 2020
Thermal Conductivity k_{pcm}(W/(mK))	0.2	Rubitherm 2020
Viscosity μ_{pcm} (kg/(ms))	0.0044	Faden et al. 2017
Thermal expansion coefficient β_{pcm} (K^{-1})	0.000865	Faden et al. 2017
Pure Solvent Melting Heat L_{pcm} (J/kg)	186000	Avik et al. 2025
Solidus Temperature $T_{\mathrm{s,pcm}}$ (K)	307.15	Rubitherm 2020
Liquidus Temperature $T_{\mathrm{l,pcm}}$ (K)	309.15	Rubitherm 2020

The values used for the Lithium-ion battery are presented in Table 6. As the focus in this thesis is on the performance of the PCM, the cell parameters are approximate, and the battery cell material is considered as homogenic instead of determining individual parameters for the specific materials of the battery.

In 3D simulations, the thermal conductivity of a battery is divided into radial and axial directions to capture thermodynamic phenomena in the cell accurately (Al-Zareer et al. 2020). The thermal conductivity in a cylindrical battery varies between the axial and radial directions, as in the axial direction the heat transfers along one material and in radial direction through several material layers (Bryden et al. 2018). However, as the focus on this thesis is on the behaviour of the PCM, and the battery is considered as homogenic, only a single value for thermal conductivity is accounted for. In the study of Steinhardt et al. (2021), the through-plane radial thermal conductivity of a 21700 Li-ion battery varies from 1 to 1.8 W/mK at different open circuit voltages. In this thesis, the heat transfer towards the PCM, i.e. the radial direction plays a more significant role and thus a value of 1 W/mK will be used for the battery thermal conductivity in all directions.

Table 6 Properties of Lithium-ion battery cell

Parameter	Value	Reference
Density ρ_{Li} (kg/m^3)	2720	Li A. et al. 2022
Specific Heat $c_{\mathrm{p,Li}}$ (J/(kgK))	830	Murashko et al. 2020
Thermal Conductivity k_{Li} (W/(mK))	1	

To consider the heat generated by the battery, it needs to be determined into Fluent as volumetric heat generation. In a simplest manner, the heat generated can be approximated by the irreversible heat of the battery as presented in Equation (18).

$$Q = RI^2 \tag{18}$$

Where I is the current of 9 A at 2C rate and R the internal resistance of 0.025 Ω. To get the volumetric heat generation, the Q needs to be divided by the volume of the battery. Therefore, the volumetric heat generation is approximated to be 79 143 $\mathrm{W/m^3}$. As mentioned in the beginning of Section 6, the rest periods between charging and discharging are not considered, which leads to a heat generation at a constant rate.

The boundary conditions of the system are determined so that the bottom of the system is considered as a stationary, no-slip wall, with zero heat flux. These setups inform Fluent that there is no heat transfer through the bottom of the system. The cut faces of the model are set as symmetry. The symmetry boundary conditions can be used with symmetric geometries to model only a part of the model to decrease computational costs. Symmetry selection informs Fluent to treat the boundaries equally, assuming reflectional symmetry with the flow and heat transfer phenomenon (Ansys Inc. 2025). The outer container faces of the model are set as walls. In this thesis, surrounding air is not considered, nor the accurate heat transfer from the container, but the convective heat transfer coefficient is approximated with empirical correlations presented in Appendix 2. The boundary conditions of the outer boundaries of the system are presented in Figure 20.

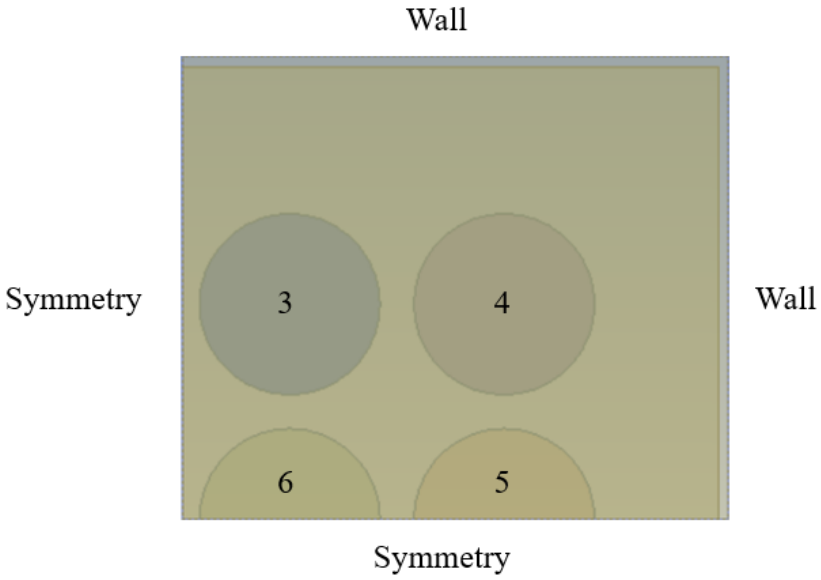


Figure 20. Boundary conditions and cell numbers

As explained by Ansys Inc. (2025), a pressure-velocity solution method informs Fluent if the pressure and velocity are solved simultaneously, i.e. coupled or separately, i.e. segregated. To assign a solution algorithm for Fluent, a scheme for the pressure-velocity method needs to be chosen. A PISO, segregated, algorithm (Pressure-Implicit and Splitting of Operators) is recommended to be used when conducting transient simulations, and thus it is chosen for this thesis.

Ansys Inc. (2025) described that in Fluent discretization methods are set to solve the convection term of the governing equations. In cases of modelling natural convection and buoyancy driven flows, a PRESTO method is recommended as the pressure's spatial discretization method. This PRESTO (PREssure STaggering Option) solves the pressure at the faces of the cell and is suitable for natural convection cases and for a wide range of meshes (Ansys Inc. 2026).

The methods for solving the convection terms in momentum and energy equations are left as default as Second Order Upwind, and the gradient method as Least Squares Cell-Based. As explained by Ansys Inc. (2026), the Second Order Upwind solution method determines the desired values at the faces of the cells through a multidimensional approach. The face values are evaluated through upwind cell's cell-centered values and through a displacement vector. The Second Order Upwind method has better accuracy than the First Order Upwind method, which determines the face values as cell-averaged values.

6.3 Grid Independence Study

In this thesis, the grid independence study is conducted with a smaller amount of PCM to decrease computational time. The spatial discretization, i.e. mesh for the system is constructed as automatic, tetrahedrons with modified sizing between the different boundaries. Especially, the regions close to the boundaries require special attention to capture the heat transfer and flow phenomena accurately.

As aforementioned, the lumped capacitance method would decrease the computational costs of the simulation, as the battery could be treated as one single uniform domain. For the lumped capacitance method to be suitable, Equation (10) should satisfy the condition of Bi < 0.1. However, depending on the temperature difference between the battery and the PCM, the convective heat transfer coefficient was approximated to be around 50–150 W/(m^2K) which results in a Biot number of around 0.2–0.7. Therefore, the lumped capacitance method is not utilized in this CFD model, and the battery domain is spatially discretized. However, as the focus is on the behaviour of the PCM, coarser discretization will be used for the battery cells to decrease computational costs.

For CFD simulation, a grid independence study needs to be performed. In the study, the simulation will be run with different sized meshes, fine, coarse and medium. The results of the study show the validity and expected error of the mesh. The grid independence study in this thesis is conducted similarly to studies by Peng et al. (2022) and Sutheesh et al. (2024), and thus the monitored variable is a single cell temperature. A monitor point is created to track the cell temperature through time with each mesh, and it is located in the middle of cell 3. The monitor point is presented in Figure 21.

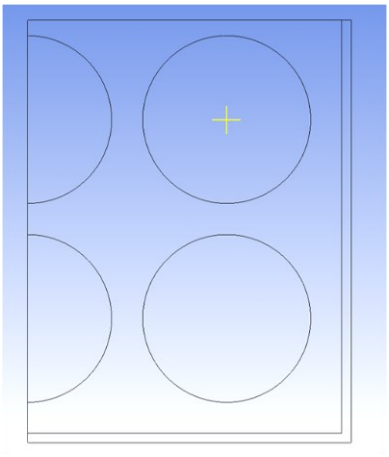


Figure 21. Monitor point from top view

The first, middle size mesh, is created so that it has 186 726 elements. In addition, a finer and a coarser mesh are created for the study, which of the fine mesh has 1 068 912 elements and coarse has only 38 140 elements. A finer grid produces a more accurate solution but increases the complexity, computational costs and storage needed (Ferziger et al. 2020). In this grid independence study, it was noticed that the first fine mesh did not produce a low enough error. Thus, an additional even finer mesh was created with 3 135 953 elements.

In Figure 22, the growth of the monitor point temperature over time is presented at different mesh sizes.

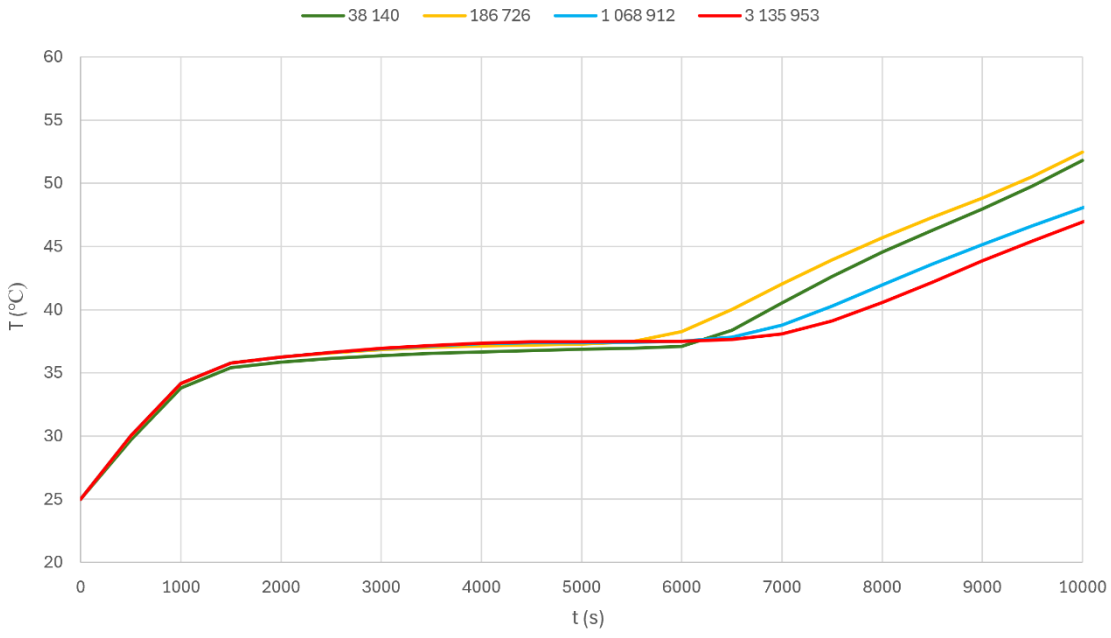


Figure 22. Monitor point temperature with each mesh

From Figure 22, it can be noticed that the overall behaviour of the curves is similar despite the differences between meshes. It can be observed that the medium and coarse mesh overpredict the temperature. The fine and finest mesh shows a lower separation between the results, with the curves showing little to no difference until 6500 s. After this, the curves seem to separate and hold a constant level of difference.

Also averaged liquid fraction is assessed for grid independence study as presented in Figure 23.

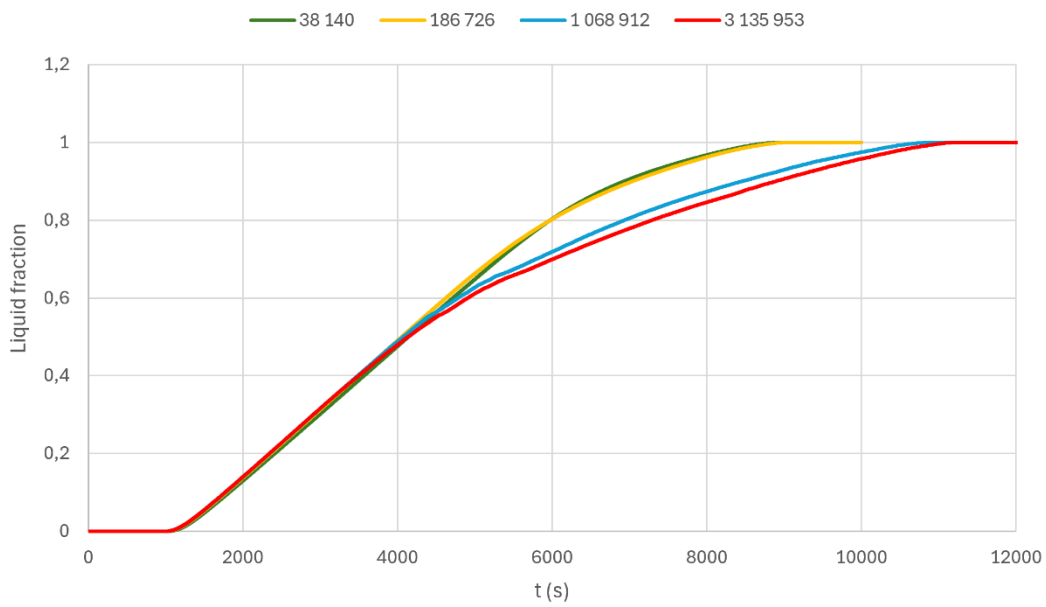


Figure 23. Liquid fraction with each mesh

From Figure 23 it can be observed that the point where fully melted stage is reached varies between the meshes. The coarse and medium mesh behave similarly, and the fully melted stage is reached at around 9000 s. With the two finer meshes, it is reached at around 11000 s, and it implies that the coarser meshes overpredict the melting, similarly to the temperature. The two finest meshes show only small deviation between each other.

One method to evaluate the precision of meshes is discretization error. The discretization error can be evaluated with the Grid Convergence Method (GCI) as described by ASME (2008). This method will be applied with the monitored variable, temperature, in the middle of cell 3.

First, a representative grid size is defined for the 3D case according to Equation (19).

$$h = \left[\frac{1}{N}\sum_{i=1}^{N}(\Delta V)\right]^{\frac{1}{3}} \tag{19}$$

Grid refinement factor r needs to be determined next. It can be determined as the relation of the meshes, and it should be greater than 1.3. The refinement factors are presented in Table 7, where 1 refers to the finest mesh with 3 135 953 elements, 2 to the fine mesh with 1 068 912 elements and 3 to the medium mesh with 186 726 elements.

Table 7 Refinement factors

Refinement factor	Value
r_{31}	2.56
r_{32}	1.79
r_{21}	1.43

From Table 7, it is noticed that the refinement factors are greater than the defined limit. Now, an apparent order p can be calculated with following Equations (20-23).

$$p = \frac{1}{\ln(r_{21})}\left|\ln\left|\varepsilon_{32}/\varepsilon_{21}\right| + q(p)\right| \tag{20}$$

$$q(p) = \ln\left(\frac{r_{21}^{p} - s}{r_{32}^{p} - s}\right) \tag{21}$$

$$s = 1 \cdot \operatorname{sgn}\left(\frac{\varepsilon_{32}}{\varepsilon_{21}}\right) \tag{22}$$

$$\varepsilon_{32} = \Phi_3 - \Phi_2 \tag{23}$$

where Φ_{k} refers to the chosen variable. ε_{21} can be obtained according to Equation (23). After this, extrapolated values can be calculated as presented in Equation (24).

$$\Phi_{\mathrm{ext}}^{21} = \frac{r_{21}^{p}\Phi_1 - \Phi_2}{r_{21}^{p} - 1} \tag{24}$$

Also Φ_{ext}^{32} can be calculated according to Equation (24). Now, the approximate relative error, extrapolated relative error and fine-grid convergence index can be calculated with Equations (25–27), respectively.

$$e_{\mathrm{a}}^{21} = \left|\frac{\Phi_1 - \Phi_2}{\Phi_1}\right| \tag{25}$$

$$e_{\mathrm{ext}}^{21} = \left|\frac{\Phi_{\mathrm{ext}}^{21} - \Phi_1}{\Phi_{\mathrm{ext}}^{21}}\right| \tag{26}$$

$$\mathrm{GCI}_{\mathrm{fine}}^{21} = \frac{1.25 e_{\mathrm{a}}^{21}}{r_{21}^{p} - 1} \tag{27}$$

The results of the GCI related errors are presented in Figure 24, and the results of approximated, e_{a}^{21}, and extrapolated, e_{ext}^{21}, relative errors are presented in Appendix 3.

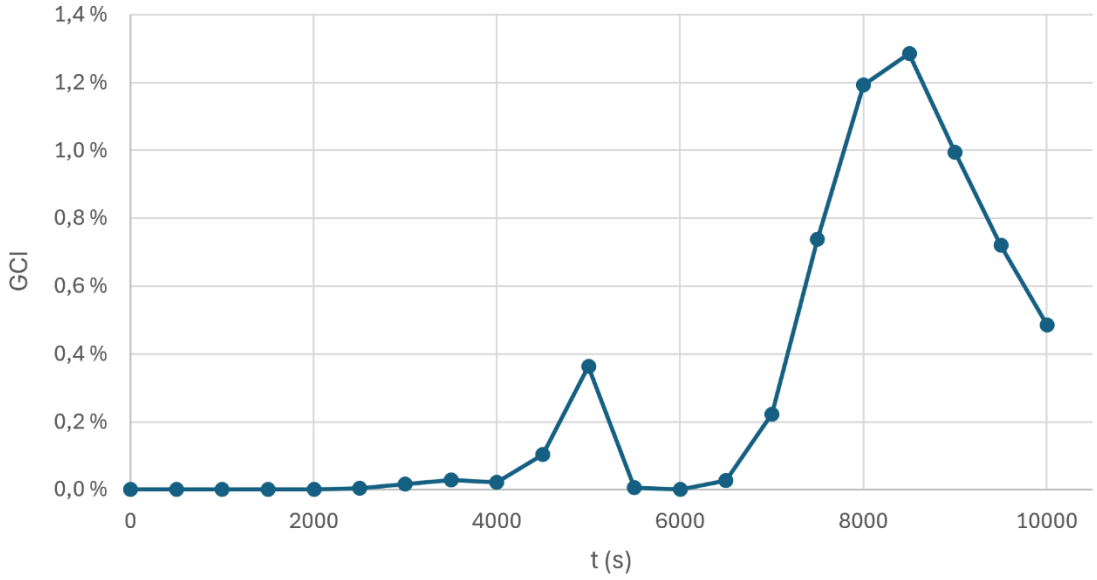


Figure 24. GCI_{fine}^{21} results

From Figure 24, it can be noticed that the error is relatively small between the two finest meshes and remains under 1.4% at all time instants. As stated by Volupe (2026), the GCI under 2% implies a solution with excellent precision. A GCI of 2–5% is suitable in most engineering studies and even 5-10% would be acceptable in parametric studies. Thus, from this grid independence study, it can be concluded that the finest grid gives results with a sufficiently low discretization error and will be applied to the results.

7 Results & Discussion

In this section the results of the simulation are presented and discussed. The simulation results will be verified with experimental data by Avik et al. (2025). In addition, possible errors affecting the results will be presented and evaluated.

In Figure 25, the liquid fraction and maximum temperature of cell 3 are presented as a function of time. The temperature profiles of each cell had similar behaviour as can be seen from Appendix 4. Therefore, only one cell's temperature profile will be utilized in the results. The similar behaviour of the temperature profiles indicate that the PCM maintains uniform maximum temperatures throughout the module, as no deviations or peaks can be observed between the cells.

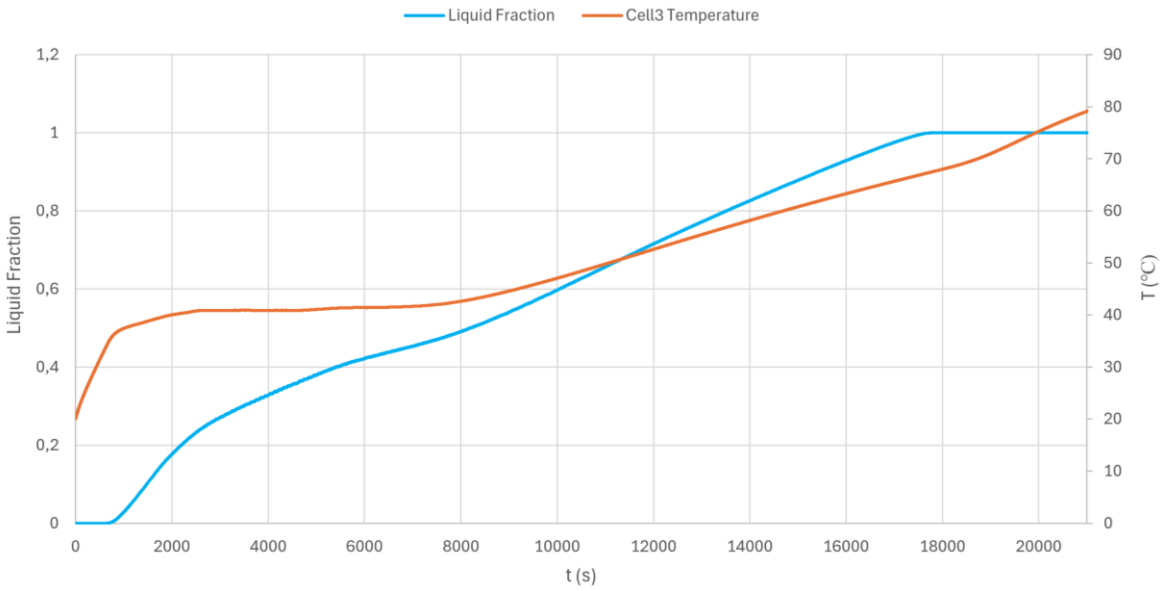


Figure 25 Max cell temperature and liquid fraction as a function of time

From Figure 25, it can be observed that the liquid fraction remains zero until the battery cell temperature reaches the melting range of the PCM, 34–36 °C. During this period, the battery temperature rises on average at a rate of 18.4 °C/1000 s (1.08 °C/min). After reaching the melting point, PCM begins to melt and absorb the heat through the latent heat, thereby slowing the temperature rise of the cell significantly. At the beginning of the melting period, the liquid fraction shows faster melting, but between 2000 s and 8000 s the melting rate decreases. This could be due to PCM melting faster in the regions adjacent to the battery cell surfaces and needing more time to melt in the outer regions further away from the heat

source. Between the start of the melting period at around 930 s, and 8000 s, the cell temperature has an average increase only of around 0.79 °C/1000 s (0.047 °C/min).

From Figure 25 it can be seen that at 8000 s, the PCM has melted approximately 50%. After this, the liquid fraction shows faster melting, which could be due to possible natural convection expediting the melting. Approximately at 8000 s, the temperature of the cell begins to increase more rapidly. This could be due to the melted PCM surrounding the cells and therefore hindering the heat dissipation from the cell surfaces. The maximum temperature of the cell shows an average increase of around 2.53 °C/1000 s (0.15 °C/min) until the end of the melting period. These findings indicate that the first 50% of the melted PCM absorbs the heat more effectively than the last 50%. This may be due to low heat transfer within the PCM.

Figure 25 shows that the time required to achieve complete melting, corresponding to a liquid fraction of 1, was approximately 18000 s (~5 h). After the PCM has fully melted, the cell temperature does not begin immediately to increase significantly faster and shows an average temperature rise of 3.6 °C/1000 s (0.21 °C/min) till 21000 s. After 19000 s, the temperature shows a slightly faster increase but remains moderate. These findings also indicate that the last 50% of melted PCM does not have a similarly significant decreasing effect on the temperature rise compared to the first 50%. On the contrary, it may hinder the cooling due to a higher amount of PCM and thus an increased thermal resistance between the battery and the surrounding air. As the last 50% of melted PCM does not decrease the rise of the cell temperature as effectively, the amount of PCM could be decreased. Optimization of the amount of needed PCM would solve the challenges associated with the weight of the PCM based BTMS as mentioned in Section 3.2.2. Additionally, the thermal conductivity of PCM could be enhanced with additives as mentioned in Section 4.2.

The cell temperature reaches almost 80 °C at 21000 s as can be seen from Figure 25. As mentioned in Section 2.3., with NCA chemistry, thermal runaway can already occur at 65 °C. As presented in Table 1, the operating temperature of INR-21700-P45B Li-ion cells is up to 60 °C. Thus, the safety limit of the cells can be considered to be 60 °C in this thesis. At the time of reaching fully melted stage, the cell temperature has already increased up to 68 °C. As it was noticed from Figure 25, after reaching 50% of melting, the temperature begins to increase significantly faster. This indicates that the PCM cannot dissipate the heat effectively enough after melting and thus cannot maintain sufficient temperature throughout

the whole melting period. As mentioned, the thermal behaviour of PCM could be enhanced with additives to increase its thermal conductivity or by optimizing the amount of PCM.

A simple Lumped Capacitance Method calculation was conducted for a single cell cooled by 20 °C air in natural convection. Low convection heat transfer coefficient of air resulted in a low Biot Number, which allowed the application of the Lumped Capacitance method. The purpose of this calculation is not to be exact but rather give a perspective how the cell temperature would act without PCM. Figure 26 presents the temperature development of the cell with and without PCM.

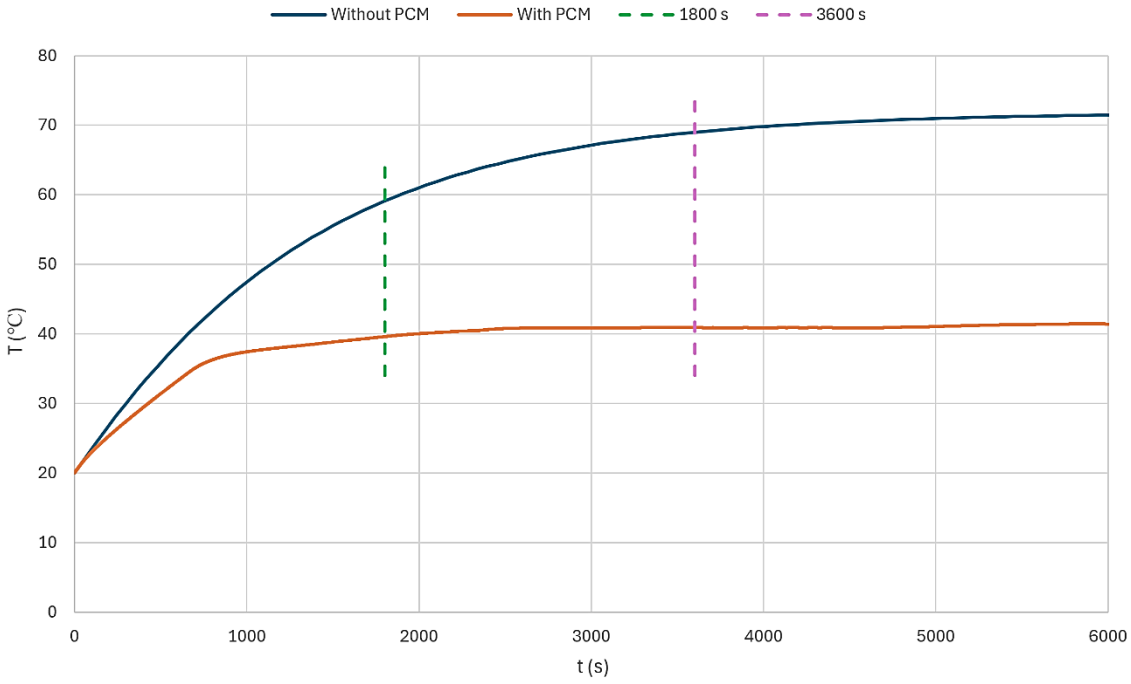


Figure 26. Cell temperature with and without PCM

Figure 26 illustrates how the PCM affects the battery's temperature, and it is observed that the temperature curves behave noticeably differently. The dashed lines mark one charge phase of 0.5 h and one discharge phase, 1 h with the studied 2C rate. From Figure 26 it is noticed that the PCM delays the temperature rise even before the temperature has reached the melting point. This is because of the high mass and higher specific heat capacity of PCM and the low thermal resistance between the cell and PCM, which allows higher heat transfer rate from the cell surface. After one charge phase, 1800 s, the temperature difference is noticeable. With PCM, the temperature stabilizes to 39.6 °C, whereas, without PCM, the temperature increases more significantly to 59.1 °C at 1800 s. After 1 h (3600 s), the temperature with PCM would only increase by approximately 1 °C to 40.9 °C, whereas

without PCM it would increase by almost 11 °C to 69 °C. This results in a temperature difference of over 28 °C between the cases.

The cell temperature with and without PCM with a longer simulation time are presented in Appendix 5. It is worth mentioning, that the container was not considered in the case without PCM and thus the cell temperature does not increase as high, as the heat can freely dissipate without the surrounding air heating up. The case without PCM achieves its maximum temperature of 72 °C already at around 6000 s, whereas the case with PCM does not reach the same temperature until 19000 s. In the PCM case, the temperature increases over a longer period of time and reaches temperature of 95 °C at around 34000 s. Although a steady state was not reached, the temperature seems to settle somewhere between 95–100 °C. However, from Figure 26 it is noticed that the PCM significantly delays the temperature rise of the cell. But, considering the safety limit of 60 °C, the module reaching over 92 °C possesses significant risk of thermal runaway. However, the case without PCM exceeds the safety limit already at 2000 s, highlighting the beneficial effect of PCM. To decrease the maximum temperature of the cell in the case containing PCM, additives could be added to enhance the thermal conductivity of the PCM, or the amount of PCM could be decreased. This would prevent excess heat accumulation around the cells.

In Figure 27, volume-averaged temperature of PCM is presented as a function of time to see how the temperature of PCM develops during battery usage.

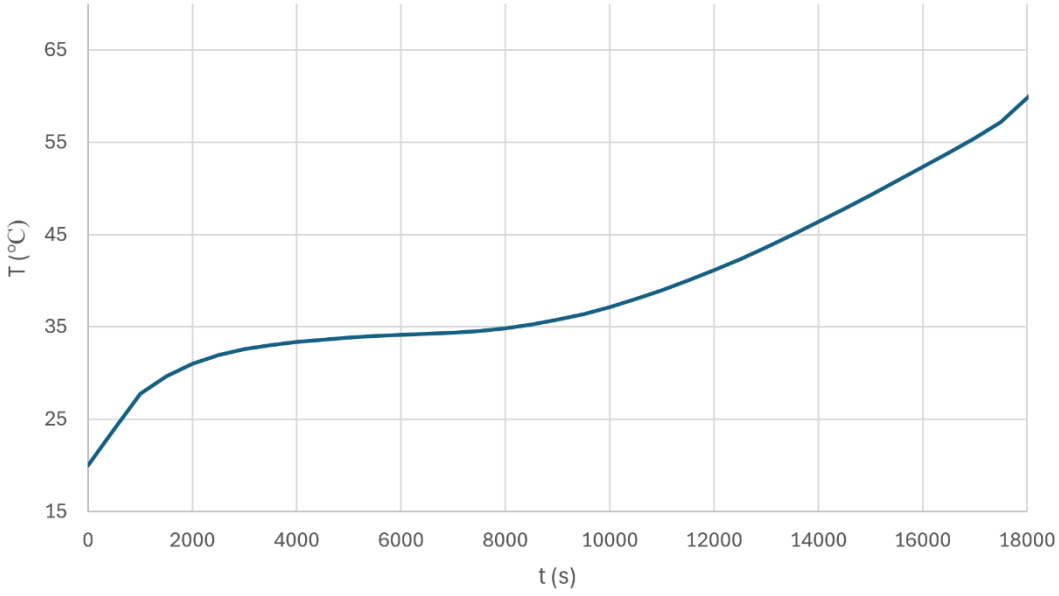


Figure 27. Volume-averaged PCM temperature

From Figure 27 it is seen that the temperature of the PCM increases significantly during the beginning. During this stage, the absorbed heat is stored as sensible heat. It can also be noticed that the temperature remains relatively stable at 2000–8000 s. As discussed in Section 4 and illustrated in Figure 13, the temperature of PCM remains close to constant during the phase change process, as the absorbed heat is utilized mostly as latent heat. Figure 25 shows that the phase change occurs approximately at 930–18000 s. At 8000 s, a liquid fraction of 50% has been reached. It can be concluded that through half of the phase change process, the temperature of the PCM remains close to constant, but begins to increase as higher liquid fraction is reached. At this stage, a higher fraction of the heat is stored as sensible heat. At 18000 s the PCM temperature reaches approximately 60 °C.

Figure 28 presents the heat storage and dissipation fractions from the generated heat during the melting period.

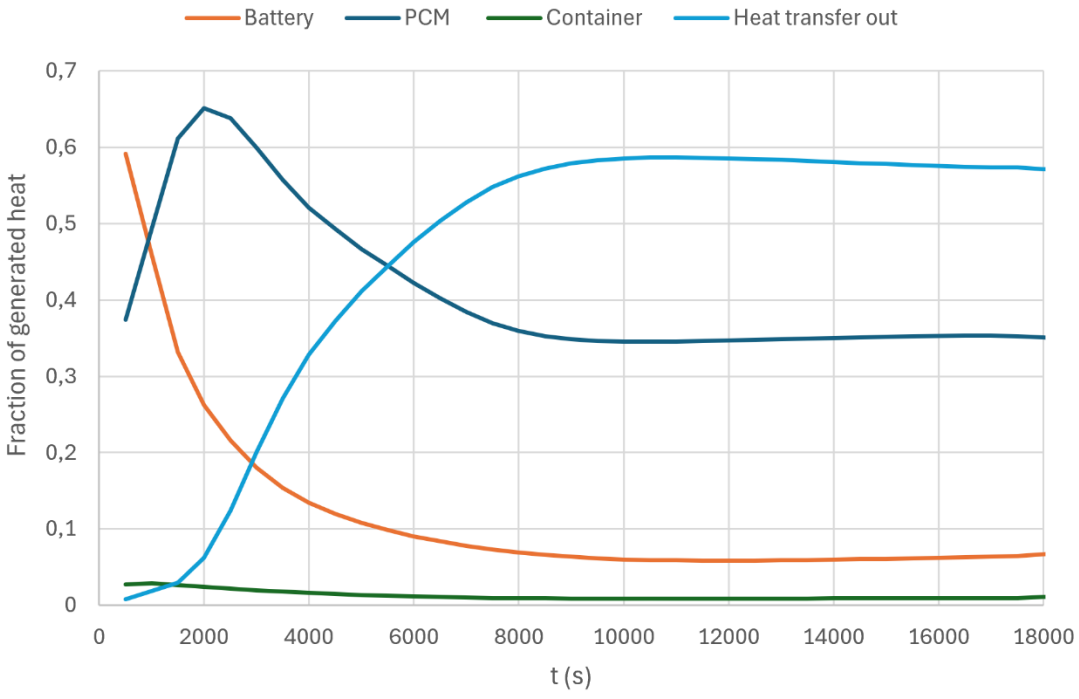


Figure 28. Heat storage and dissipation fractions

From Figure 28, it can be noticed that in the beginning, the battery has the highest fraction of heat stored. At this point, the heat generation has increased the cell temperature, but significant amounts of heat have not yet been transferred to the surrounding materials. The fraction decreases with time, as the heat begins to dissipate from the battery surfaces to the surrounding materials. When looking at the PCM curve, it is noticed that heat storage fraction increases significantly from the beginning. At around 2000 s, the fraction of heat

stored in PCM reaches its peak and begins to decrease as the heat transfer out increases. Simultaneously, the melting process slows down, as seen from Figure 25. The decreasing storage fraction and the slowed melting indicate that the PCM remaining in the solid phase is located further away from the heat source, resulting in an increased thermal resistance between the battery and melting front. The container has a relatively low and uniform fraction of the heat stored throughout the melting period, which is expected due to low mass and volume. The fraction is slightly higher in the beginning but decreases as the PCM begins to melt and the heat transfer out of the system increases. The heat transfer out increases to approximately 8000 s, the first 50% of melting. After that, the heat transfer out of the systems begins to stabilize and even decrease, as the melting in the PCM proceeds further and heat absorption increases.

In Figures 30-39, graphical results of the simulation will be presented. The contours and temperatures are obtained at different locations within the module. The locations of the planes and lines are presented and named in the following Figure 29. Even though Figure 29 presents a quarter of the module, the graphical results will be mirrored for the whole module to get a better understanding of the overall behaviour.

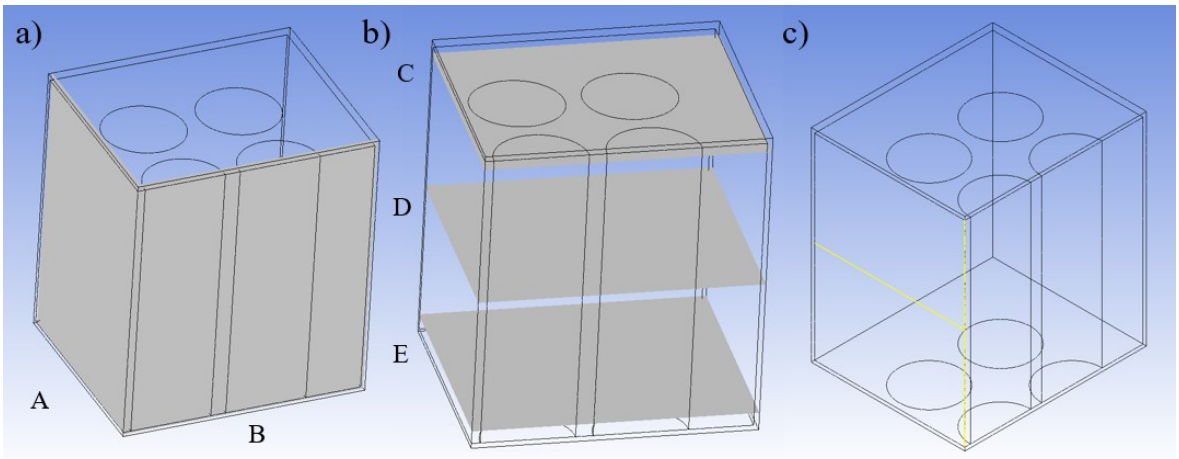


Figure 29. Locations of planes; a) Vertical planes A and B, b) Horizontal planes C, D and E, c) Lines for vertical and horizontal temperatures

In next Figures 30–32, the liquid fraction is presented from vertical and horizontal perspectives. Figure 30 presents the liquid fraction from perspective A, Figure 31 from perspective B and Figure 32 from the three different horizontal planes.

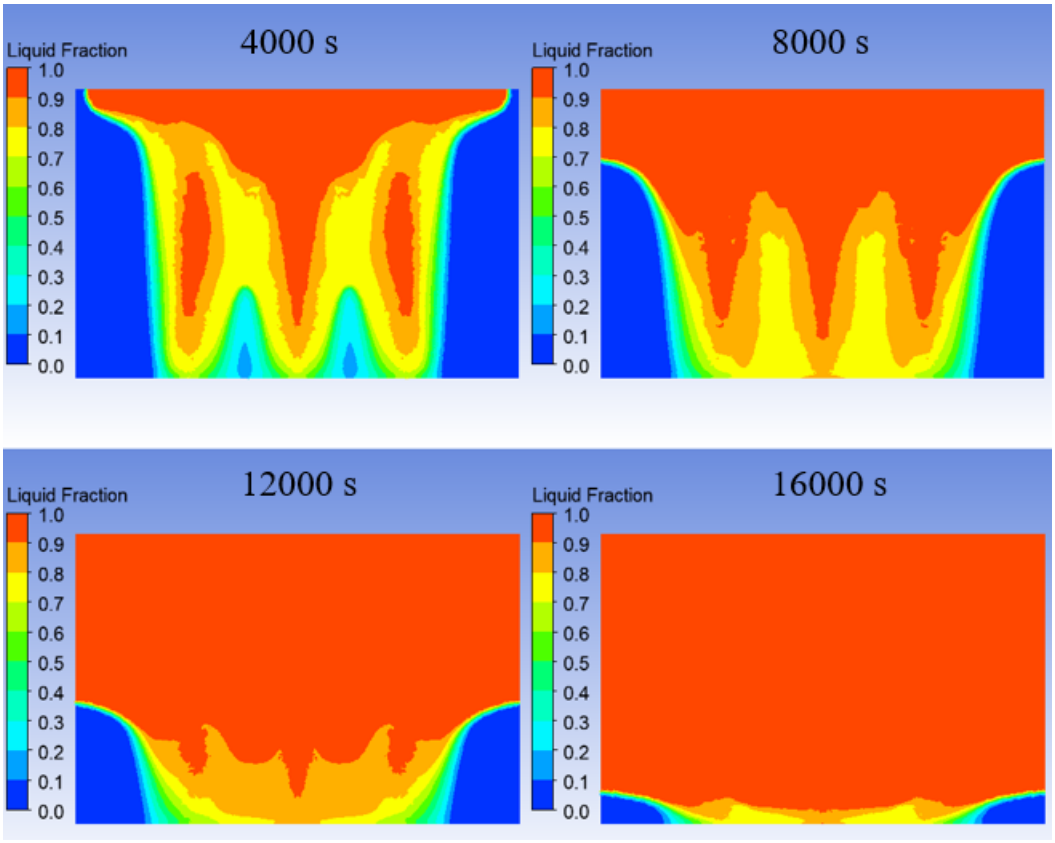


Figure 30. Liquid fraction from perspective A at different time instants

Figure 30 illustrates how the melting proceeds through a liquid fraction contour. The melting of the PCM begins between the cells where the heat is transferred from the cell surface to the surrounding PCM. Already at 4000 s, it is clearly noticed that melting proceeds faster near the battery cells and faster at the upper part compared to the bottom. Even though at 16000 s the PCM has nearly fully melted, small regions remain in solid phase in the bottom corners of the module. These regions take more time to melt due to their distance from the heat source and the melting proceeding faster at the upper part of the module. This is most likely due to natural convection transferring heat towards the upper part of the module and away from the bottom part.

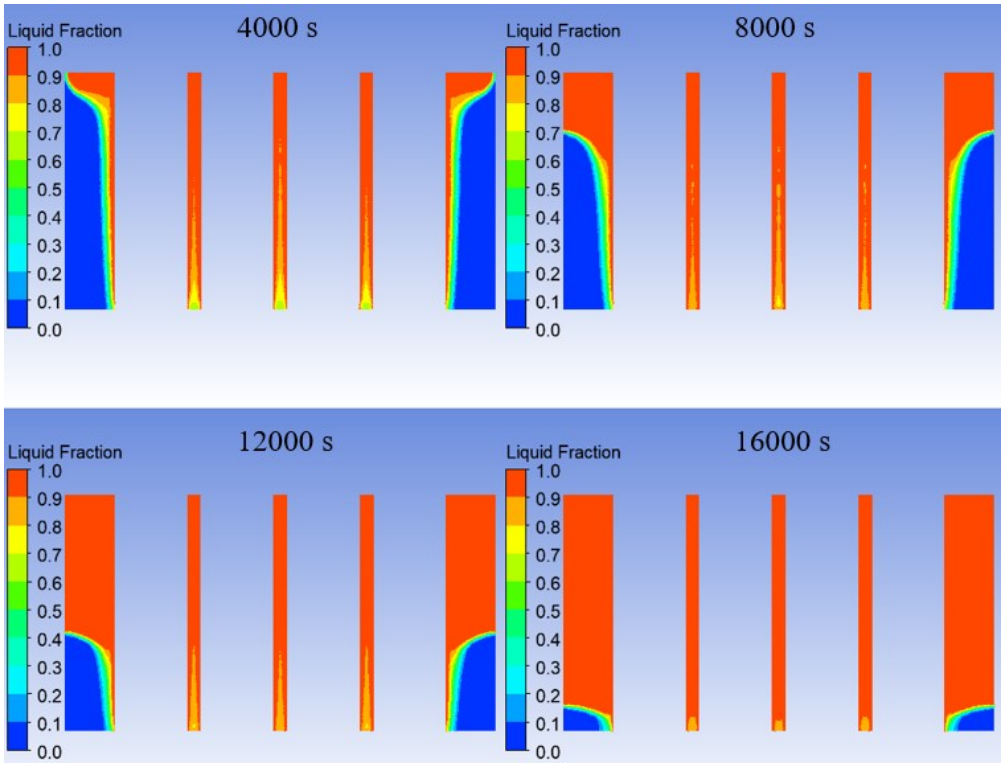


Figure 31. Liquid fraction from perspective B at different time instants

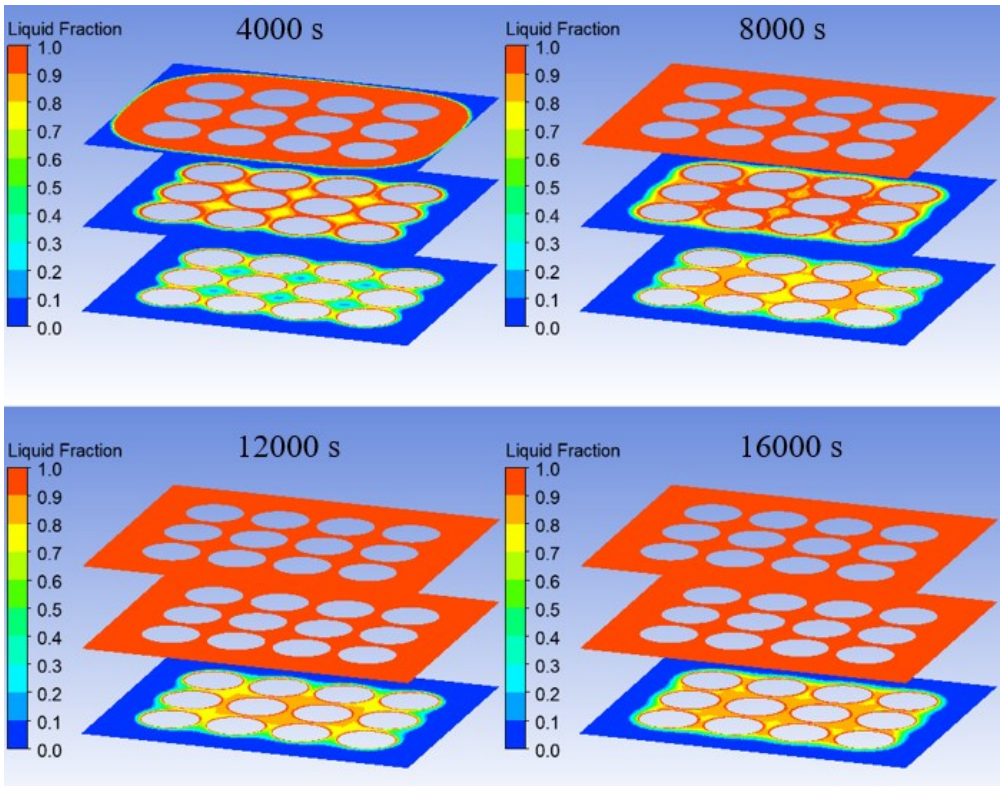


Figure 32. Horizontal liquid fraction contour at different time instants

Figures 31 and 32 illustrate the melting process from vertical perspective B and horizontal perspective. It is noticed that the melting proceeds fastest at the PCM surfaces adjacent to the vertical surfaces of the battery cell, where the heat is generated. It can also be noticed that the melting of PCM is faster at the upper part than at the bottom, which could be caused by natural convection. Figure 32 shows only little difference between 12000 s and 16000 s. However, when looking at Figure 31, it is noticed that the melting is proceeding but has not reached the bottom plane E yet at 16000 s, and thus, in the horizontal direction the melting is similar between the time instants. Figure 32 also highlights the effect of a rectangular shape of the container, as the corners and outer sides need more time to fully melt. In these locations, the heat transfers to the container and out of the system, which can also slow down the melting. The liquid phase is achieved faster in the middle of the module. Thus, the melting is non-uniform, and the corner regions increase the deviation in liquid fraction rise.

In Figures 33–37 the temperature contours and vertical and horizontal temperature profiles of the module at different time instants are presented. In Figure 33 and 34 present the vertical planes A and B.

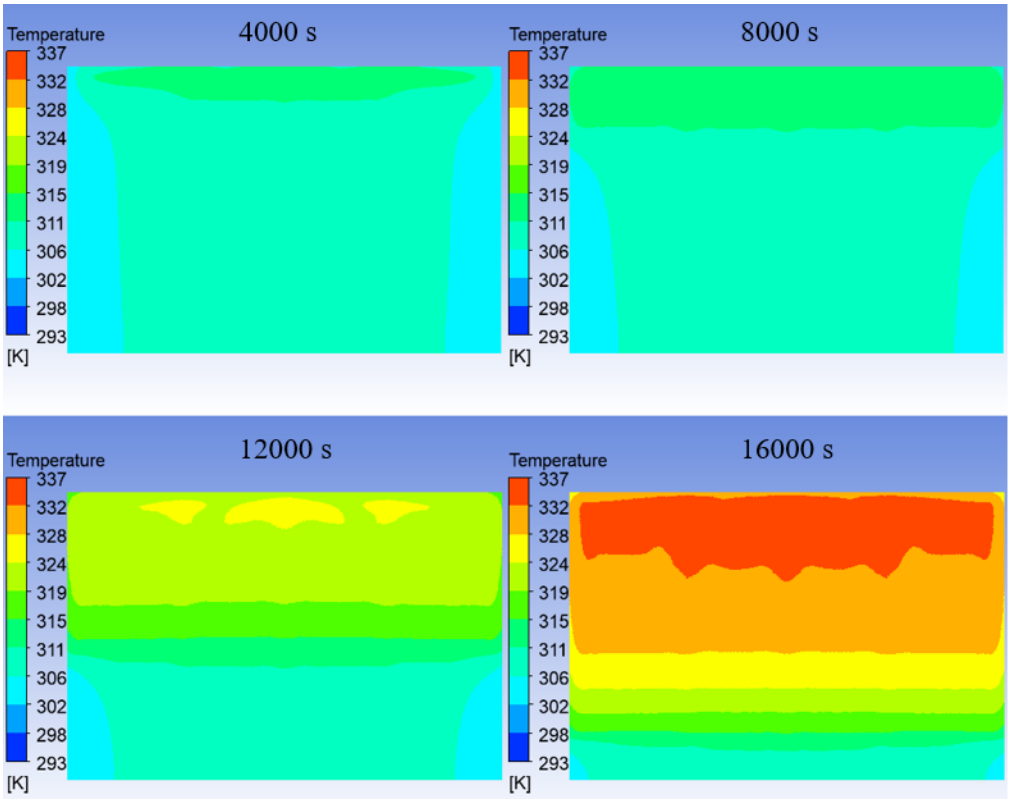


Figure 33. Temperature contour from perspective A at different time instants

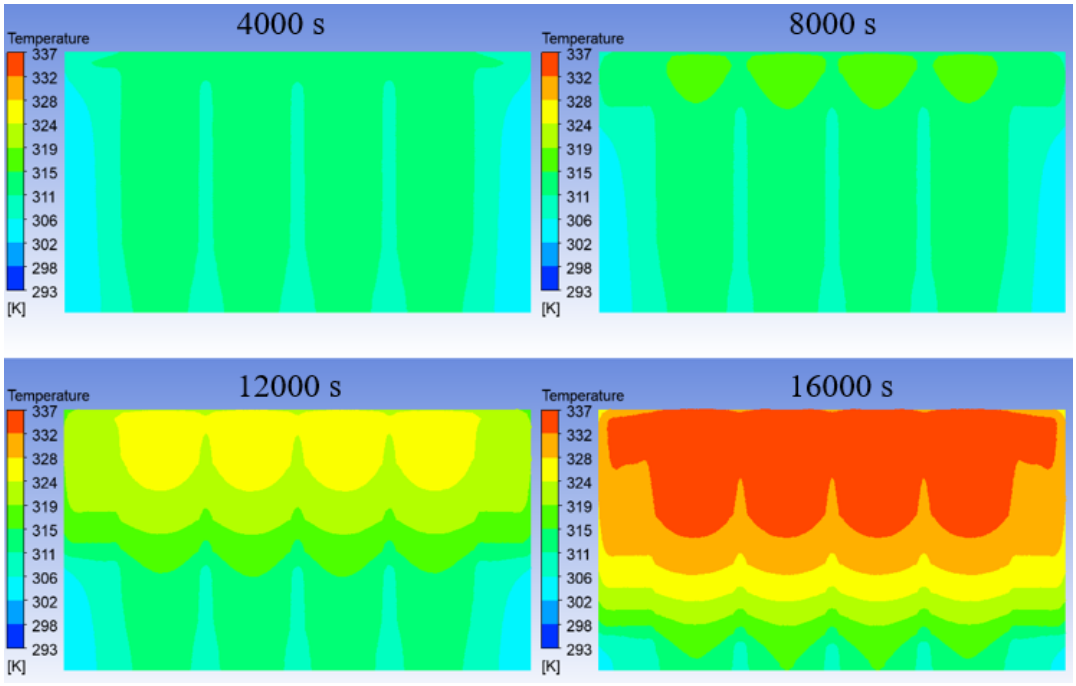


Figure 34. Vertical temperature contour from perspective B at different time instants

Figures 33 and 34 illustrate the temperature contours of the module at different time instants. It can be observed that the temperature increases faster near the cells. This is consistent with the liquid fraction contours shown in Figure 30, where it was found that the PCM melted faster near the cells. Furthermore, the heat accumulates in the upper part of the module, and the temperature increases up to 64 ℃ at 16000 s. This behaviour is supported by Figure 25, where the cell maximum temperature reaches 64 ℃ at 16000 s.

When looking at Figures 30, 31, 33 and 34, it can be noticed that the temperatures begin to increase more rapidly after a higher liquid fraction is reached. Thus, it could be concluded that fully melted PCM is less effective at limiting the temperature and cannot dissipate the heat efficiently. This could also be seen from Figure 25. However, the temperature distribution remains relatively uniform across the width of the module despite the outer bottom regions of the module as can be seen from Figure 33.

In Figure 35 and 36, the horizontal and vertical temperature profiles are presented. The temperatures are obtained at locations shown in Figure 29.

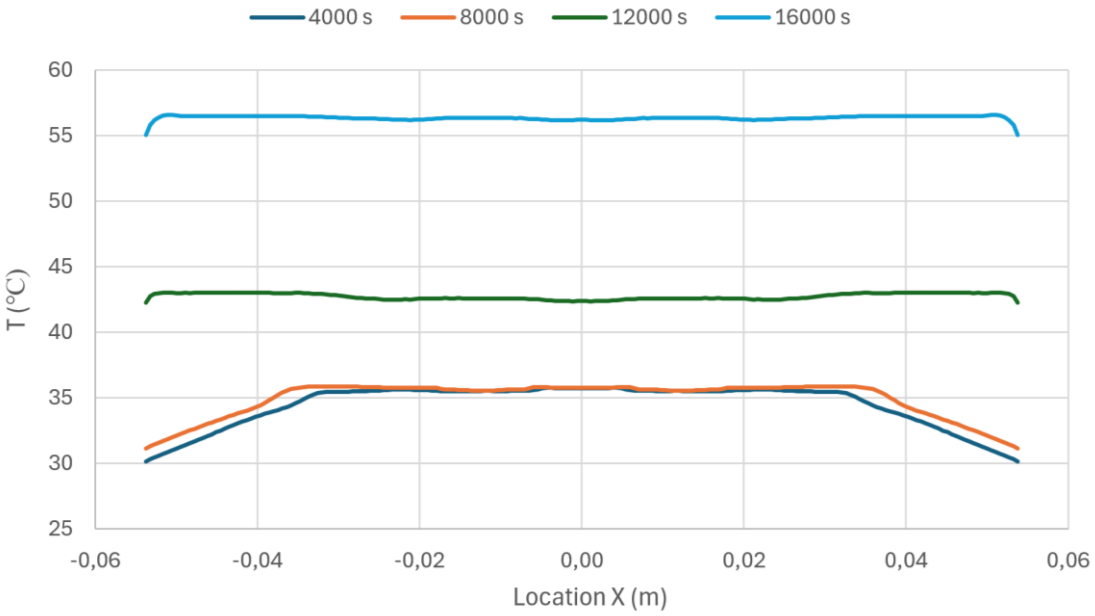


Figure 35. Horizontal temperature profiles

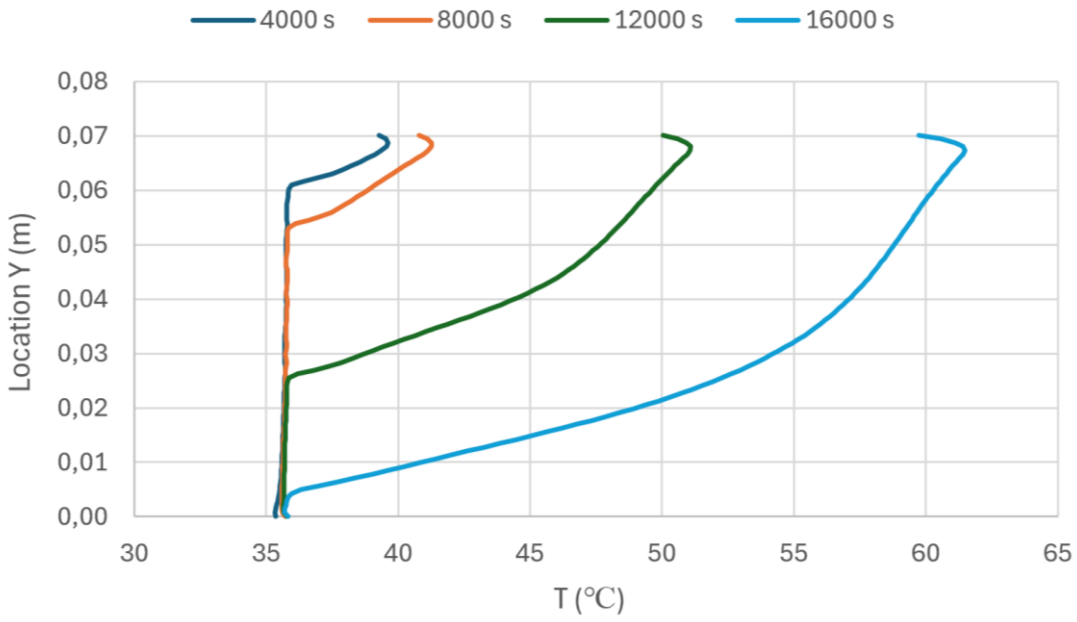


Figure 36. Vertical temperature profiles

From Figure 35 it is noticed that the horizontal temperature remains relatively uniform. At earlier stages of melting, 4000 s and 8000 s, the temperature begins to decrease at approximately 0.03 m away from the centre. When looking at Figure 30, it is noticed that at these locations the PCM is still in solid form, and thus at lower temperature. The maximum temperature difference at these time instants is approximately 5 °C. As the PCM has reached

higher liquid fraction at 12000 s and 16000 s, the temperatures are higher and remain more uniform. However, at all time instants, the temperature decreases close to the walls, which is expected due to heat dissipation into the surrounding air.

Figure 36, on the other hand, shows higher temperature deviations the further the time and melting proceeds. At 4000 s and 8000 s, the temperature curves behave similarly and remain relatively uniform, except at the upper side of the module, where the PCM has already melted as seen in Figure 30. However, at 8000 s module reaches slightly higher temperatures, approximately 40 ℃, whereas at 4000 s, the peak temperature is at around 39 ℃. More deviation can be noticed between the 12000 s and 16000 s temperature curves. Already at 12000 s, the temperature has increased significantly and the deviations in vertical direction are significant, the peak temperature reaching 51 ℃. At the bottom part of the module, the temperature remains close to 36 ℃ in all cases, whereas on the upper part the temperature increases up to 61 ℃ at 16000 s. However, close to the top, at around 4 mm from the air boundary, the temperature begins to decrease rapidly at all time instants due to heat transfer to the surroundings. These results indicate that the PCM maintains a more uniform temperature across the width but cannot maintain a uniform temperature in the vertical direction as the melting proceeds.

In Figure 37, the temperature contours are presented from horizontal planes.

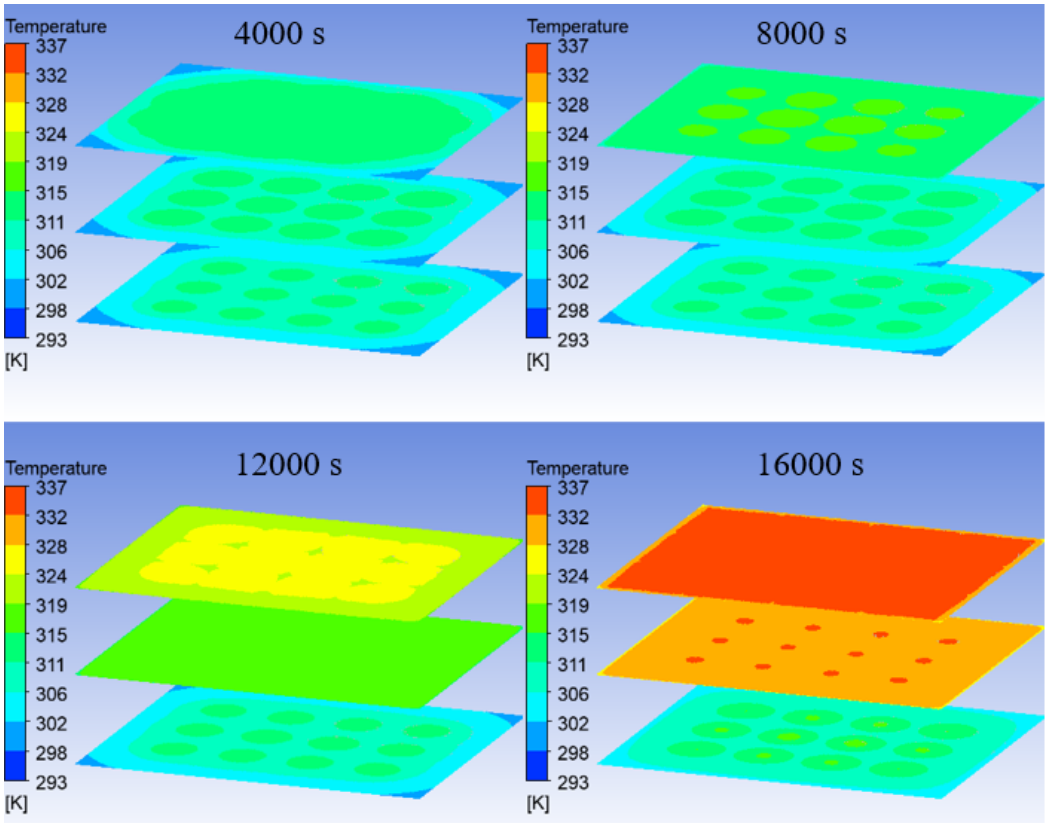


Figure 37. Horizontal temperature contour at different time instants

Figure 37 illustrates temperature distribution across the module from a horizontal perspective, highlighting variations in temperature among the battery cells and corner regions of the module. At 8000 s, higher temperatures can be observed in the cells in the middle of plane C. This is due to the surrounding cells generating heat and low thermal conductivity of the PCM, which limits the heat dissipation. At 16000 s the temperature of the battery cells is reaching 64 °C also at plane D.

It is noticed from Figures 33–37, that there is a temperature deviation in vertical direction exceeding the aforementioned 5 °C limit. This deviation within the module can negatively affect the batterie's performance and lifetime. This vertical temperature deviation is due to the faster melting of the PCM at the upper part of the module, and thus the heat accumulating there.

In the next Figure 38, the velocity vectors in the PCM region are presented.

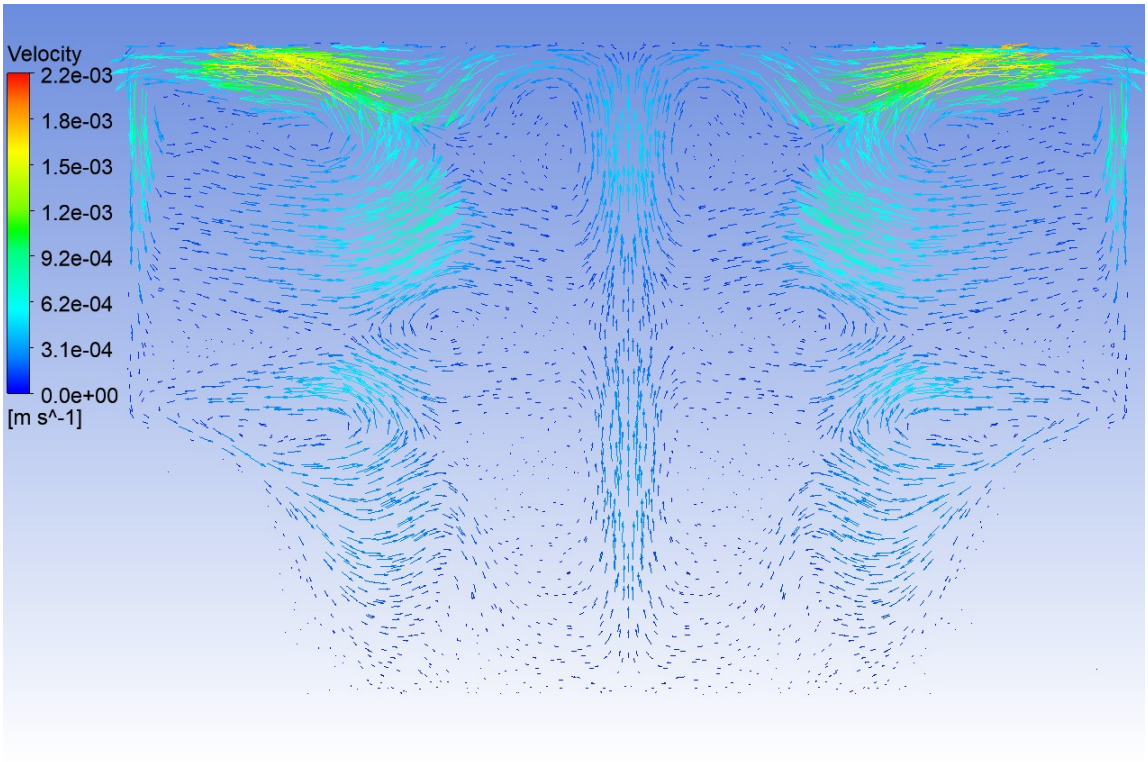


Figure 38. Velocity vectors from perspective A at 12000 s

Figure 38 illustrates the velocity fields within the molten PCM and confirms that natural convection exists in the PCM. It is noticed that liquid PCM near the warm batteries rises due to the buoyancy forces, while cooler PCM descends towards the bottom in cooler regions. From Figure 37, it can be noticed that the cooler regions at 12000 s are located at the outer sides and corners of the container. The movement of the liquid material creates visible recirculation zones within the PCM. In other words, less dense, warmer material rises to the top and forces cooler, denser material to descend to the bottom.

Natural convection explains why the PCM first melted from the top and took more time at the bottom as shown in Figures 30-32. Natural convection enhances the heat transfer and thus the melting proceeds faster at the upper part of the module. The maximum velocity of the PCM is obtained at the maximum simulation time of 21000 s, where the velocity is still only at 0.0034 m/s.

In the next Figure 39, the wall heat flux is presented at 8000 s and 16000 s.

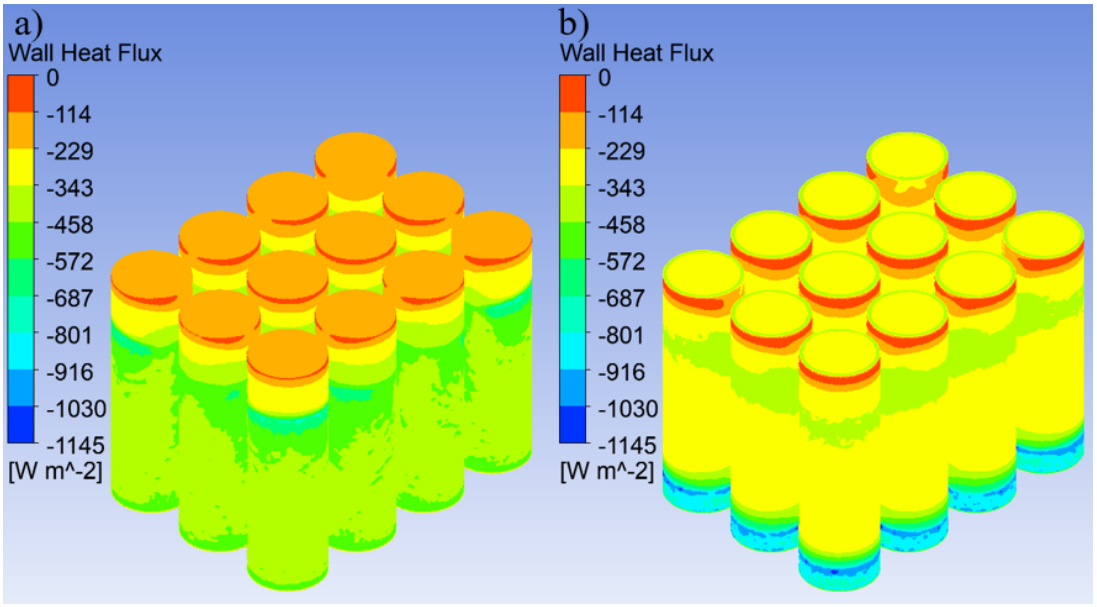


Figure 39. Wall heat flux of battery cells; a) at 8000s b) at 16000s

Figure 39 illustrates the wall heat flux on the battery surfaces and shows whether the heat is released from the cells (negative values) or absorbed by the cells (positive values). As can be noticed, the heat flux is mostly in the negative region, meaning that heat is transferring from the cells to the surrounding PCM. The wall heat flux at 8000 s is mainly around -500 W/m^2, and at 16000 s mainly around -300 W/m^2. This indicates that the heat transfer from the cells to the PCM is greater at 8000 s than at 16000 s. This is attributed to the lower temperatures of PCM at 8000 s due to the ongoing phase change and to a higher temperature difference between the cells and surrounding PCM. At 16000 s, more variation can be observed along the cell surface. Near the bottom of the cell, where the PCM is still in solid phase, the heat flux is around -900 W/m^2 and at the top, where the PCM has fully melted, the heat flux is close to 0 W/m^2. This indicates that in vertical direction, the cooling effect of the PCM is not uniform, on the contrary, it may hinder the cooling and cause variations in heat transfer.

7.1 Model Verification

The study by Avik et al. (2025) experimentally studied the thermal behaviour of the NCA Li-ion batteries, and the effect of Rubitherm's RT35HC phase change material on the battery temperatures. In the study, the batteries were cycled numerous times with different charge rates from 1–2C. The tests were conducted at 0–100% SOC for battery electric vehicle

(BEV) and at 20–80% SOC for plug-in hybrid electric vehicles (PHEV). The results of this study are compared to the results of the PHEV test. In the PHEV test, the battery was charged/discharged 8 times consecutively, which resulted in a 2 h 42 min cycle. After these cycles, there were 45 min rest periods. At 2C rate, only the case containing PCM was studied, as the battery temperature without PCM had already increased close to the determined safety limit of 50 °C at 1.5C rate. Temperatures were measured from various locations between the cells and thermal images of the module were taken at the end of the whole cycle.

In the work by Avik et al. (2025), the temperature of the battery was calculated as an average temperature of the measured temperatures between the cells. The temperature of the container (box) was also obtained as an average of two points near the container wall. From the simulated results, the temperatures are obtained similarly for validation on plane D. The experimental temperatures and the simulated temperatures are shown in Figure 40.

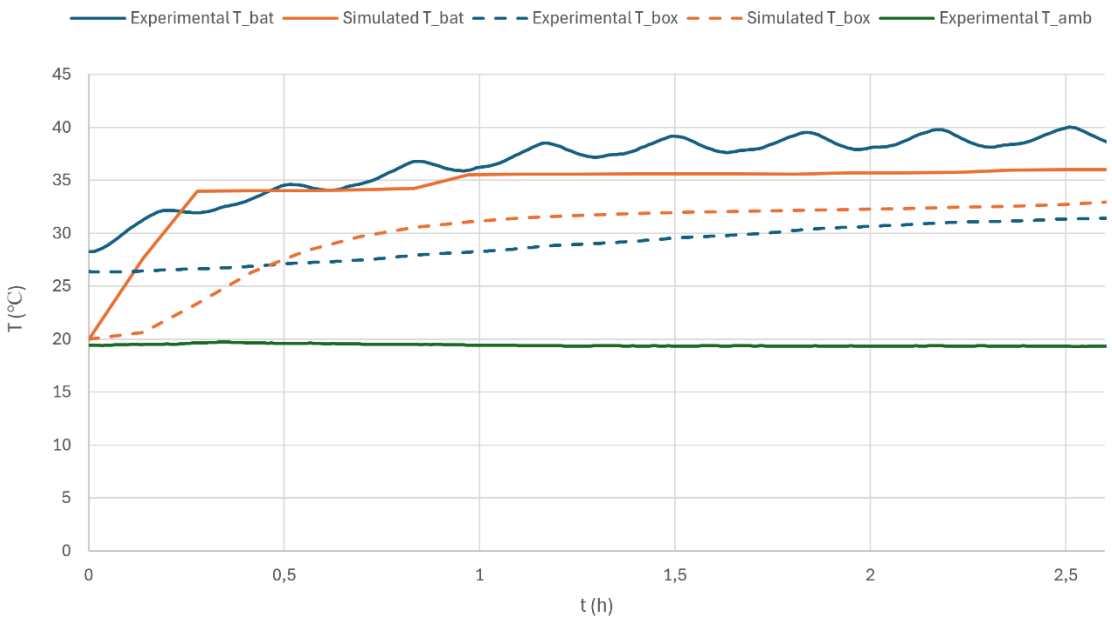


Figure 40. Averaged battery and container temperature, experimental and numerical study results

From Figure 40 it is noticed that the temperatures behave similarly and follow primarily the same curve. In the simulated case, the temperatures take approximately 0.25 h to 0.5 h to achieve the same temperature levels as the experimental case. This is due to the time needed for the simulated case to heat up from the initial ambient temperature. After this, the simulated temperature shows relatively similar temperatures as the experimental, despite

small differences. The simple vertical and horizontal natural convection coefficient correlations may not fully reflect the actual heat transfer phenomenon and thus cause some errors, especially with the container (box) temperature. In addition, the experimental case experiences fluctuations, as the simulated results show steadier behaviour. The fluctuations are due to the consecutive charge/discharge cycling, which may cause internal resistance to fluctuate according to SOC, and thus affect the temperature.

The thermal image of the study by Avik et al. (2025), presented in Appendix 6, shows alignment with the simulated results. The thermal image presents cooler regions at the outer sides of the container, and even cooler regions at the bottom corners of the container. Similar thermal behaviour was also observed in the simulation conducted in this thesis. In the work by Avik et al. (2025), a figure of the module was taken after the whole 2C experiment. The figure is presented in Appendix 7. It can be noticed that the PCM had melted in the middle but remained in a solid state at the top side, bottom and corners of the module. In this thesis, melting proceeded the fastest at the top side of the module. This difference is most probably due to the neglected air inside the container, as in experimental study, the direct contact between PCM and air provided better heat dissipation. Despite the differences in setup, the similarity in temperature behaviour suggests that the developed 3D model captures overall thermal behaviour.

Furthermore, Avik et al. (2025) concluded that the PCM delayed the temperature increase of the module and battery cells, even though it did not stop the temperature increasing. At the 2C rate, the PCM limited the peak temperature to 46 ℃ in the PHEV test, as where the lower C rate case without the PCM reached temperatures close to 50 ℃. Similar effects were also observed from the results of this thesis. When the cases with and without PCM were compared, PCM delayed the temperature rise significantly. After one charging phase, without PCM, the temperature increased up to 59.1 ℃, whereas with PCM the temperature remained at 39.6 ℃.

Overall, experimental and numerical studies showed similar results, indicating that the simulation was conducted successfully. Despite the differences between the operating conditions, both showed beneficial effects of the PCM, as it delayed the temperature rise of the module, thereby improving its thermal performance and safety.

7.2 Sources of Error

Like Ferziger et al. (2020) have described, in a CFD -study the sources of errors include modelling error, discretization error, which was already discussed in Section 6.3, and iterative error. More specifically, these contain the uncertainty of the parameters, boundary conditions, and the time stepping method.

The modelling errors are due to the simplifications of the model, which are done to maintain reasonable computational costs, or because complex phenomenon and exact properties are not known and are difficult to predict (Ferziger et al. 2020). In this thesis, several assumptions were made which may be the source of modelling error. The geometry of the system was significantly simplified. The battery cells were considered plain cylinders, and no connection strings or battery details were considered. In the actual setup, the cells are not directly in contact with the bottom of the container but are placed on a 3D printed holder. Therefore, PCM surrounds the bottom of the cells as well, but this was not considered in this thesis.

Additionally, simplifications were made to the boundary and domain conditions, which may increase modelling error. The bottom of the model was considered adiabatic, meaning no heat transferred through the bottom of the cell nor the container. In reality, there would be heat transfer taking place from the container to the surrounding materials. The surrounding ambient air was not considered, as was not the air inside the container between the battery tops and the container lid. The heat transfer from the container to the environment was approximated through the correlations. The battery cell's heat generation was considered constant instead of varying heat generation based on the SOC and other operating conditions. In addition, the Boussinesq approximation was applied to PCM, which considers constant density, but takes buoyancy forces into account in the momentum equation. This removes the effects of thermal expansion.

The discretization error is caused by discretizing the governing equations in space and time (Ferziger et al. 2020). To minimize the spatial error, a grid independence study was conducted, where the error was found to be of excellent precision. For time discretization, an error-based adaptive time stepping method was utilized, with an error tolerance of 1%. As described by Ansys Inc. (2025), the error-based adaptive time stepping means that the software updates the time step size based on a calculated truncation error. If the truncation

error is smaller than the assigned tolerance, the time step size is updated and increased, and if it is higher, the time step size is decreased. According to the Ansys guide, for most cases, the tolerance of 1% is suitable.

The iterative error refers to the errors caused by the iterative solution method. As described by Ferziger et al. (2020), iterative methods are used to solve the equations, as direct solutions are computationally too expensive to solve. The iterative error describes the difference between exact solutions and iterative solutions. Iterative solutions can be controlled via convergence criteria, i.e. defining the level of residuals. The reduction in the level of the residuals is equivalent to the reduction in the error. Thus, the level of the error should be small enough, but also large enough to keep the computational costs reasonable. After reaching the assigned residuals, the iterations usually stop. As stated by Ansys Inc. (2025), there is no specific value that would be suitable for all CFD problems. By default, the residuals are 10^{-3} for other equations, expect for the energy equation the residual is 10^{-6}. In steady state heat transfer simulations, the residuals should decrease to 10^{-6}, but in transient simulations it is more beneficial to monitor relevant key values as the residuals may fluctuate (Abbaspur 2026). In this thesis, the residuals were set to 10^{-6} for all equations.

Altogether, the highest error is most probably caused by the modelling error. There were several assumptions and simplifications made, which can all affect the results. The discretization error by space was found to be respectively small, and the discretization for time was applied through adaptive time stepping, which should maintain acceptable tolerance of error. The residuals were set to a sufficiently low level, especially for a transient simulation. Thus, the iterative error is not expected to significantly affect the results.

8 Conclusions

The purpose of this thesis was to study the behaviour of phase change material as a thermal management system for a Li-ion battery module. The behaviour was studied by developing a numerical, 3D CFD -model. More precisely, the focus of this thesis was on capturing the melting front and natural convection taking place in the PCM, and how they affect the temperatures of the Li-ion battery module. Other objectives of this thesis were to understand the configuration, working principle and the heat generation mechanisms of Li-ion batteries. The objectives also included discussion of the materials used in Li-ion batteries, the effects of temperature and introduction of different thermal management systems.

It was found that the Li-ion batteries possess many advantages and are therefore used in many applications with increasing use in EVs. Li-ion batteries contain many components, and their working principle is a complex electrochemical process. It was also found that there are several options for the materials which all influence the performance of the Li-ion battery. In addition to materials, internally generated heat and ambient temperatures have a significant effect on the Li-ion battery's performance and safety. Too high temperatures within a cell, module or a pack, can lead to thermal runaway, and in the worst-case scenario, to an explosion. Thus, the thermal management of Li-ion batteries has significant importance in ensuring the safety of applications.

This thesis found that there are multiple possibilities for battery thermal management systems. These include active management systems, such as active air- and liquid-cooling, and passive management systems, such as passive air-cooling, a heat pipe system and a phase change material based system. PCM based systems have raised interest due to their low costs and simplicity. Despite their benefits, PCM based BTMS also have limitations due to limited ability to absorb heat. Thus, it is important to pay attention to the thermal behaviour of PCM.

Previous numerical studies on PCM have examined the thermal conductivity of composite PCMs, or the effectiveness of the passive system compared to active management. It was found that even though the thermal conductivities of pure phase change materials weren't sufficient to maintain optimal temperatures of Li-ion batteries, the PCMs maintained more uniform temperature profiles within the battery cells or modules. In these studies, however,

either the natural convection had been neglected or the PCM wasn't in direct contact with the battery cells.

A numerical, 3D CFD -model was developed utilizing Ansys Fluent. The model was based on an actual module, which consisted of 12 Li-ion INR-21700 cells. The module was placed in a polypropylene container. The empty volume was filled with PCM, and it was thus in direct contact with the battery cells. To reduce computational costs, several assumptions and simplifications were made. The sources of error in the CFD -study included modelling error, discretization error and iteration error. The discretization error was found to be at excellent precision in the grid independence study. The heat generation was assumed to be constant, as the primary focus was on the behaviour of the PCM and its melting process throughout the melting period.

The developed model showed that the studied pure paraffin based PCM delayed the temperature rise of battery cells significantly. When compared to a case where only air surrounded the battery cells, the PCM was found to significantly slow down the increase in temperature even before it had reached its melting point, and even more significantly after that, resulting in a temperature difference over 28 °C after one charge and one discharge phase. However, results also showed that the PCM had limited ability to remove the heat from the cell's surface. After reaching 50% of the melting, the cell temperature began to increase significantly, implying that the last 50% of the PCM provides only limited benefit. The fully melted phase was achieved at approximately 18000 s (~5 h) with constant charging at the 2C rate. After 18000 s, the temperature growth didn't change significantly, which also implies to the limited effectiveness of the last 50% of the PCM. Thus, the amount of PCM could be decreased. Additionally, the thermal conductivity of the PCM could be increased with additives, to increase its ability to transfer the heat away from the cells.

Natural convection was captured successfully in the model. The velocity vectors, and temperature and liquid fraction contours showed that warmer, liquid PCM rose towards the upper part of the module, and cooler PCM descended towards the bottom at cooler locations. Natural convection explained the non-uniform melting behaviour of the PCM, causing faster melting on the upper side of the module. Besides this, also the rectangular form of the container slowed down the melting of the bottom corner regions of the module and thus delayed achieving the fully melted stage. It was noticed that even though the PCM delayed the temperature rise, it could not maintain uniform melting or a uniform temperature

distribution in vertical direction. These issues could also be reduced by increasing the PCM thermal conductivity with additives.

The validation showed that the simulation was able to reproduce the overall thermal behaviour and spatial temperature distributions, indicating good qualitative agreement with the experimental and simulated results. However, the differences in operating conditions may explain the differences between the results. The assumptions and simplifications made in this thesis most probably cause the modelling error to be the largest source of error. This study neglected the surrounding ambient air as well as the air inside the container to decrease computational costs, and thus the heat transfer out of the system was approximated through correlations. In future studies, details of the batteries, container, and overall the module and operating conditions should be considered to capture more accurate behaviour of the PCM and heat transfer. In addition, the enhanced and differing thermal conductivity of the PCM should be studied further to see how it affects the melting process and the temperatures of the module. For future numerical studies, variable heat generation by the battery should be considered to see how cyclic charging affects the behaviour of the PCM.

Altogether, this thesis achieved its objectives, and successfully developed a numerical, 3D model for a phase change material as a battery thermal management system. The PCM was found to significantly delay the temperature rise of the module, and natural convection was found to expedite the melting of the upper part of the PCM. However, the PCM has limited ability to effectively remove the heat from the cells, and it couldn’t maintain a uniform cooling effect in vertical direction due to natural convection. The simplifications of the model should also be noted, and future work should further study the effects of PCM thermal conductivity and cyclic heat generation.

References

Abbaspur, A. (2026). CFD LAND; Ansys Fluent Convergence. [Website]. [Referred 11.8.2026]. Available: https://cfdland.com/ansys-fluent-convergence/

Ali, H. (2024). Thermal Management for Batteries: From Basic Design to Advanced Simulation and Management Methods. ISBN: 978-0-443-19025-4

Al-abidi, A., Mat, S., Sopian, K., Sulaiman, M. & Mohammed, A. (2013). CFD applications for latent heat thermal energy storage: a review. Renewable and Sustainable Energy Reviews 20, pp. 353-363. DOI: 10.1016/j.rser.2012.11.079

Al-Zareer, M., Michalak, A., Da Silva, C. & Amon, C. H. (2020). Predicting specific heat capacity and directional thermal conductivities of cylindrical lithium-ion batteries: A combined experimental and simulation framework. Applied Thermal Engineering, Vol 182, 116075. DOI: 10.1016/j.applthermaleng.2020.116075

Ansys, Inc. (2026). Ansys Fluent Theory Guide. Release 2026, R1. Available [PDF]: https://ansyshelp.ansys.com/public/Views/Secured/corp/v261/en/pdf/Ansys_Fluent_Theory_Guide.pdf

Ansys, Inc. (2025). Fluent User's Guide. Release 2025, R2. Available: https://ansyshelp.ansys.com/public/account/secured?returnurl=/Views/Secured/corp/v252/en/flu_ug/pt01.html

Ashby, M. (2021). Material property data for engineering materials. Department of Engineering, University of Cambridge. 5th edition. Available [PDF]: https://www.ansys.com/content/dam/amp/2021/august/webpage-requests/education-resources-dam-upload-batch-2/material-property-data-for-eng-materials-BOKENGEN21.pdf

ASME. (2008). Procedure for Estimation and Reporting of Uncertainty Due to Discretization in CFD Applications. Journal of Fluids Engineering, Vol 130, 078001. DOI: 10.1115/1.2960953

Avik, A., Kannan, A., Ruuskanen, V., Mostafaie, S. & Kauranen, P. (2025). Passive thermal management of a Li-ion battery module using phase change materials. Applied Thermal Engineering, Vol 288, 129563. DOI: 10.1016/j.applthermaleng.2025.129563

Battery Design (2022). Battery Cooling Options. [Website]. [Referred 12.5.2026]. Available: https://www.batterydesign.net/battery-cooling-options/

Bernardi, D., Pawlikowski, E. & Newman, J. (1985). A General Energy Balance for Battery Systems. Journal of The Electrochemical Society, Vol 132, 5.

Bianco, V., De Rosa, M. & Vafai, K. (2022). Phase-change materials for thermal management of electronic devices. Applied Thermal Engineering, Vol 214, 118839. DOI: 10.1016/j.applthermaleng.2022.118839

Bryden, T., Dimitrov, B., Hilton, G., Ponce de León, C., Bugryniec, P., Brown, S., Cumming, D., Cruden, A. (2018). Methodology to determine the heat capacity of lithium-ion cells. Journal of Power Sources, Vol 395, pp. 369-378. DOI: 10.1016/j.jpowsour.2018.05.084

Conrad (2023). Overview of current battery technologies » Comparison of rechargeable battery types. [Website]. [Referred 7.5.2026]. Available: https://www.conrad.com/en/guides/industry/rechargeable-battery-technologies.html

Chen, F., Huang, R., Wang, C., Yu, X., Liu, H., Wu, Q., Qian, K. & Bhagat, R. (2020). Air and PCM cooling for battery thermal management considering battery cycle life. Applied Thermal Engineering, Vol 173, 115154. DOI: 10.1016/j.applthermaleng.2020.115154

Chen, J., Kang, S., E, J., Huang, Z., Wei, K., Zhang, B., Zhu, H., Deng, Y., Zhang, F. & Liao, G. (2019). Effects of different phase change material thermal management strategies on the cooling performance of the power lithium ion batteries: A review. Journal of Power Sources 442, 227228. DOI: 10.1016/j.jpowsour.2019.227228

COMSOL (2017). COMSOL Multiphysics Reference Manual 5.3a. Available [PDF]: https://doc.comsol.com/5.3a/doc/com.comsol.help.comsol/COMSOL_ReferenceManual.pdf

El Idi, M., Karkri, M. & Abdou Tankari, M. (2021). A passive thermal management system of Li-ion batteries using PCM composites: Experimental and numerical

investigations. International Journal of Heat and Mass Transfer 169, 120894. DOI: 10.1016/j.ijheatmasstransfer.2020.120894

EPA (United States Environmental Protection Agency). (2026). Sources of Greenhouse Gas Emissions. [Website]. [Updated 9.6.2026]. Available: https://www.epa.gov/ghgemissions/sources-greenhouse-gas-emissions

Etacheri, V., Marom, R., Elazari, R., Salitra, G. & Aurbach, D. (2011). Challenges in the development of advanced Li-ion batteries: a review. Energy & environmental science, 4, pp. 3243-3262. DOI: 10.1039/C1EE01598B

Faden, M., König-Haagen, A., Höhlein, S. & Brüggemann, D. (2017). An implicit algorithm for melting and settling of phase change material inside macrocapsules, International Journal of Heat and Mass Transfer, Vol 117, pp. 757-767. DOI: 10.1016/j.ijheatmasstransfer.2017.10.033

Ferziger, J., Perić, M., & Street, R. (2020). Computational Methods for Fluid Dynamics, 4th edition. DOI: 10.1007/978-3-319-99693-6.

Finkelstein, S., Ricci, M., Bötticher, T. & Schmidt-Rohr, K. (2024). How lithium-ion batteries work conceptually: thermodynamics of Li bonding in idealized electrodes. Physical Chemistry Chemical Physics 26, pp. 24157-24171. DOI: 10.1039/D4CP00818A

Goodenough, J. & Park, K. (2013). The Li-Ion Rechargeable Battery: A Perspective. Journal of the American chemical society, Vol 135, pp. 1167-1176. DOI: 10.1021/ja3091438

Gulfam, R., Zhang, P. & Meng, Z. (2019). Advanced thermal systems driven by paraffin-based phase change materials – A review. Applied Energy Vol 238, pp. 582-611. DOI: 10.1016/j.apenergy.2019.01.114

Huang, R., Li, Z., Hong, W., Wu, Q. & Yu, X. (2019). Experimental and numerical study of PCM thermophysical parameters on lithium-ion battery thermal management. Energy Reports, Vol 6, pp. 8-19. DOI: 10.1016/j.egyr.2019.09.060

IEA. (2026). Global battery markets are growing strongly – and so are the supply risks. [Online]. [Referred 10.7.2026]. Available: https://www.iea.org/commentaries/global-battery-markets-are-growing-strongly-and-so-are-the-supply-risks

Incropera, F., Dewitt, D., Bergman, T. & Lavine, A. (2007). Fundamentals of Heat and Mass Transfer. 6th edition. pp.3-10

Inkeri, E., Tynjälä, T. & Nikku, M. 2022. Numerical modeling of latent heat thermal energy storage integrated with heat pump for domestic hot water production. Applied Thermal Engineering, Vol 214, 118819. DOI: 10.1016/j.applthermaleng.2022.118819

Intergovernmental Panel on Climate Change (2023). Summary for Policymakers. In: Climate Change 2023; Synthesis Report. Contribution of Working Groups I, II and III to the Sixth Assessment Report of the Intergovernmental Panel on Climate Change. IPCC, Geneva, Switzerland, pp. 1-34. DOI: 10.59327/IPCC/AR6-9789291691647.001

In-Taek, O., Lee, J., Han, J., Lee, S., Kim, S. & Rhi, S. (2023). Li-Ion Battery Immersed Heat Pipe Cooling Technology for Electric Vehicles. Electronics, Vol 12, Iss. 24. DOI: 10.3390/electronics12244931

Kim, J., Oh, J. & Lee, H. (2018). Review on battery thermal management system for electric vehicles. Applied Thermal Engineering, Vol 149, pp. 192-212. DOI: 10.1016/j.applthermaleng.2018.12.020

Li, A., Yuen, Y., Chun, A., Wei, W., Jingwen, W., Chun Sing, L., Sanghoon, K. & Heng Yeoh, G. (2022). Thermal Propagation Modelling of Abnormal Heat Generation in Various Battery Cell Locations. Basel, Vol 8, Iss. 11. DOI:10.3390/batteries8110216

Li, Y., Yang, J. & Song, J. (2017). Design structure model and renewable energy technology for rechargeable battery towards greener and more sustainable electric vehicle. Renewable and Sustainable Energy Reviews, Vol 74, pp. 19-25. DOI: 10.1016/j.rser.2017.02.021

Liao, Z., Zhang, S., Li, K., Zhang, G. & Habetler T. (2019). A survey of methods for monitoring and detecting thermal runaway of lithium-ion batteries. Journal of power sources, Vol 436, 226879. DOI: 10.1016/j.jpowsour.2019.226879

Ling, Z., Wang, F., Fang, X., Gao, X. & Zhang, Z. (2015). A hybrid thermal management system for lithium ion batteries combining phase change materials with forced-air cooling. Applied Energy 148, pp. 403-409. DOI: 10.1016/j.apenergy.2015.03.080

Liu, C., Neale, Z. & Cao, G. (2016). Understanding electrochemical potentials of cathode materials in rechargeable batteries. Materials Today, Vol 19, number 2, pp.109-123.

Liu, H., Wei, Z., He, W. & Zhao, J. (2017). Thermal issues about Li-ion batteries and recent progress in battery thermal management systems: A review. Energy Conversion and Management 150, pp. 304-330. DOI: 10.1016/j.enconman.2017.08.016

Liu, L., Zhang, X. & Lin, X. (2022). Recent Developments of Thermal Management Strategies for Lithium-Ion Batteries: A State-of-The-Art Review. Energy Technology, Vol 10, 2101135. DOI: 10.1002/ente.202101135

Mohammadian, S., He, Y. & Zhang, Y. (2015). Internal cooling of a lithium-ion battery using electrolyte as coolant through microchannels embedded inside the electrodes. Journal of Power Sources, Vol 293, pp. 458-466. DOI: 10.1016/j.jpowsour.2015.05.055

Molicel (2026). Product data sheet: Model INR-21700-P45B. [Referred 13.5.2026]. Available: https://www.molicel.com/wp-content/uploads/INR21700P45B_1.2_Product-Data-Sheet-of-INR-21700-P45B-80109.pdf

Murashko, K.A., Pyrhönen, J. & Jokiniemi, J. (2020). Determination of the through-plane thermal conductivity and specific heat capacity of a Li-ion cylindrical cell. International Journal of Heat and Mass Transfer, Vol 162, 120330. DOI: 10.1016/j.ijheatmasstransfer.2020.120330

OpenCFD Ltd. (2024a). OpenFoam; Fundamentals. [Website]. [Updated 2.1.2024]. [Referred 30.4.2026]. Available: https://doc.openfoam.com/2312/quickstart/

OpenCFD Ltd. (2024b). OpenFoam: Quickstart. [Website]. [Updated 2.1.2024]. [Referred 30.4.2026]. Available: https://doc.openfoam.com/2312/quickstart/

Passerini, S., Bresser, D., Moretti, A. & Varzi, A. (2020). Batteries : Present and Future Energy Storage Challenges. DOI: 10.1002/9783527610426. ePDF ISBN: 978-3-527-82730-5

Peng, P., Wang, Y. & Jiang, F. (2022). Numerical study of PCM thermal behavior of a novel PCM-heat pipe combined system for Li-ion battery thermal management. Applied Thermal Engineering, Vol 209, 118293. DOI: 10.1016/j.applthermaleng.2022.118293

Pesaran, A. (2002). Battery thermal models for hybrid vehicle simulations. Journal of Power Sources, Vol 110, pp. 377-382

Rubitherm Technologies (2020). Data Sheet: RT35HC. [Online]. Available [PDF]: https://www.rubitherm.eu/media/products/datasheets/Techdata_-RT35HC_EN_09102020.PDF

Rubitherm Technologies (2026). What is PCM. [Website]. [Referred 16.4.2026]. Available: https://www.rubitherm.eu/en/pcm.html

Sharma, A., Tyagi, V., Chen, C. & Buddhi, D. (2009). Review on thermal energy storage with phase change materials and applications. Renewable and Sustainable Energy Reviews 13, pp. 318-345. DOI: 10.1016/j.rser.2007.10.005

Sabbah, R., Kizilel, R., Selman, J. & Al-Hallaj, S. (2008). Active (air-cooled) vs. passive (phase change material) thermal management of high power lithium-ion packs: Limitation of temperature rise and uniformity of temperature distribution. Journal of Power Sources 182, pp. 630-638. DOI: 10.1016/j.jpowsour.2008.03.082

Sharma, R., Ganesan, P., Tyagi, V., Metselaar, H. & Sandaran, S. (2015). Developments in organic solid–liquid phase change materials and their applications in thermal energy storage. Energy Conversion and Management 95, pp. 193-228. DOI: 10.1016/j.enconman.2015.01.084

Steinhardt, M., Gillich, E., Rheinfeld, A., Kraft, L., Spielbauer, M., Bohlen, O. & Jossen, A. (2021). Low-effort determination of heat capacity and thermal conductivity for cylindrical 18650 and 21700 lithium-ion cells. Journal of Energy Storage, Vol 42, 103065. DOI: 10.1016/j.est.2021.103065

Sun, C. (2019). Advanced Battery Materials. ISBN 978-1-119-40755-3

Sun T., Yan, Y., Wang, X., Rasool, G., Zhang, K. & Li, T. (2025). A comprehensive study on heat transfer mechanism and thermal runaway suppression of the lithium-ion battery. International Journal of Heat and Mass Transfer, Vol 245, 127027. DOI: 10.1016/j.ijheatmasstransfer.2025.127027

Sutheesh, P., Jose, J., Hotta, T. & Rohinikumar, B. (2024). Numerical investigations on thermal performance of PCM-based lithium-ion battery thermal management system

equipped with advanced honeycomb structures. International Communications in Heat and Mass Transfer, Vol 158, 107937. DOI: 10.1016/j.icheatmasstransfer.2024.107937.

The Engineering ToolBox. (2003). Air Viscosity: Dynamic and Kinematic Viscosity at Various Temperatures and Pressures. [Online]. [Referred 5.6.2026] Available: https://www.engineeringtoolbox.com/air-absolute-kinematic-viscosity-d_601.html

The Engineering ToolBox. (2009). Air Properties - Thermal Conductivity vs. Temperature and Pressure Charts and Calculator. [Online]. [Referred 5.6.2026]. Available: https://www.engineeringtoolbox.com/air-properties-viscosity-conductivity-heat-capacity-d_1509.html

Tomaszewska, A., Chu, Z., Feng, X., O'Kane, S., Liu, X., Chen, J., Ji, C., Endler, E., Li, R., Liu, L., Li, Y., Zheng, S., Vetterlein, S., Gao, M., Du, J., Parkers, M., Ouyang, M., Marinescu, M., Offer, G. & Wu, B. (2019). Lithium-ion battery fast charging: A review. eTransportation 1, 100011. DOI: 10.1016/j.etran.2019.100011

Tukes. (2026). Lifecycle of lithium-ion batteries. [Website]. [Referred 1.7.2026]. Available: https://tukes.fi/en/lifecycle-of-lithium-ion-batteries

Volupe. (2026). Grid Convergence Index (GCI) Calculator. [Website]. [Referred 16.7.2026]. Available: https://volupe.com/support/grid-convergence-index-calculator/

Wang, Qian; Jiang, B., Li, B. & Yan, Y. (2016). A critical review of thermal management models and solutions of lithium-ion batteries for the development of pure electric vehicles. Renewable and Sustainable Energy Reviews, Vol 64, pp. 106-128. DOI: 10.1016/j.rser.2016.05.033

Wang, Qingsong; Ping, P., Zhao, X., Chu, G., Sun, J. & Chen, C. (2012). Thermal runaway caused fire and explosion of lithium ion battery. Journal Power Sources, Vol 208, pp. 210-224. DOI: 10.1016/j.jpowsour.2012.02.038

Warner, J. (2024). The Handbook of Lithium-Ion Battery Pack Design: Chemistry, Components, Types and Terminology. 2nd edition. ISBN: 978-0-443-13807-2

Wilke, S., Schweitzer, B., Khateeb, S. & Al-Hallaj, S. (2016). Preventing thermal runaway propagation in lithium ion battery packs using a phase change composite material: An

experimental study. Journal of Power Sources, Vol 340, pp. 51-59. DOI: 10.1016/j.jpowsour.2016.11.018

Yang, L., Villalobos, U., Akhmetov, B., Gil, A., Khor, J., Palacios, A., Li, Y., Ding, Y., Cabeza, L., Tan, W. & Romagnoli, A. (2021). A comprehensive review on sub-zero temperature cold thermal energy storage materials, technologies, and applications: State of the art and recent developments. Applied Energy, Vol 288, 116555. DOI: 10.1016/j.apenergy.2021.116555

Yang, T., Yang, N., Zhang, X. & Li, G. (2016). Investigation of the thermal performance of axial-flow air cooling for the lithium-ion battery pack. International Journal of Thermal Sciences, Vol 108, pp. 132-144. DOI: 10.1016/j.ijthermalsci.2016.05.009

Zaynetdinov, K., Inkeri, E., Nikku, M. & Tynjälä, T. (2024). Experimental and numerical investigation of a laboratory-scale shell-and-tube latent heat storage. Applied Thermal Engineering, Vol 262, 125213. DOI: 10.1016/j.applthermaleng.2024.125213

Zhang, J., Shao, D., Jiang, L., Zhang, G., Wu, H., Day, R. & Jiang, W. (2022). Advanced thermal management system driven by phase change materials for power lithium-ion batteries: A review. Renewable and Sustainable Energy Reviews,Vol 159, 112207. DOI: 10.1016/j.rser.2022.112207

Zhu, P., Gastol, D., Marshall, J., Sommerville, R., Goodship, V. & Kendrick, E. (2020). A review of current collectors for lithium-ion batteries. Journal of Power Sources, Vol 485, 229321. DOI: 10.1016/j.jpowsour.2020.229321

Zubi, G., Dufo-López, R., Carvalho, M. & Pasaoglu, G. (2018). The lithium-ion battery: State of the art and future perspectives. Renewable and Sustainable Energy Reviews, Vol 89, pp. 292-308. DOI: 10.1016/j.rser.2018.03.002

Appendix 1. Experimental setup, no PCM



Figure A1 – 41 Container with Li-ion cells

Appendix 2. Correlations for determining the convective heat transfer coefficient

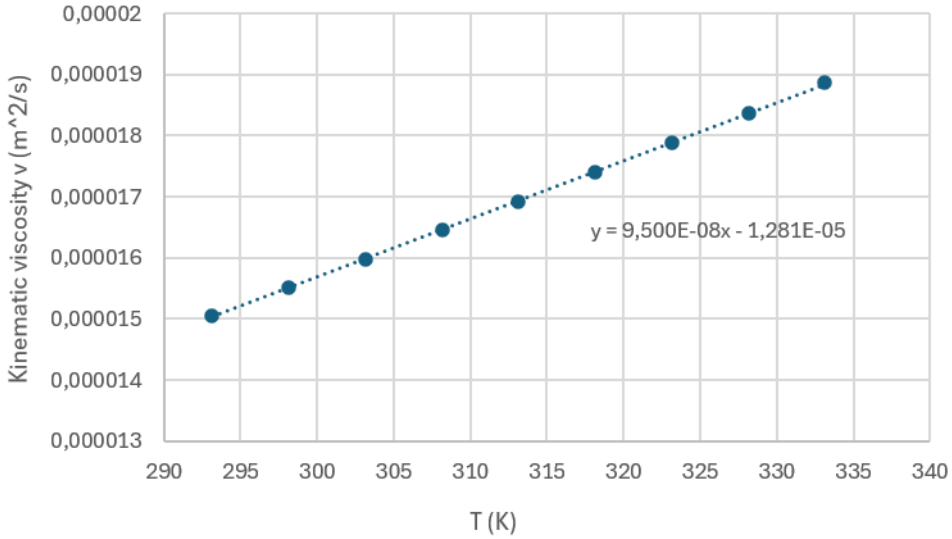


Figure A2 – 1 Fit for kinematic viscosity, data from The Engineering ToolBox (2003).

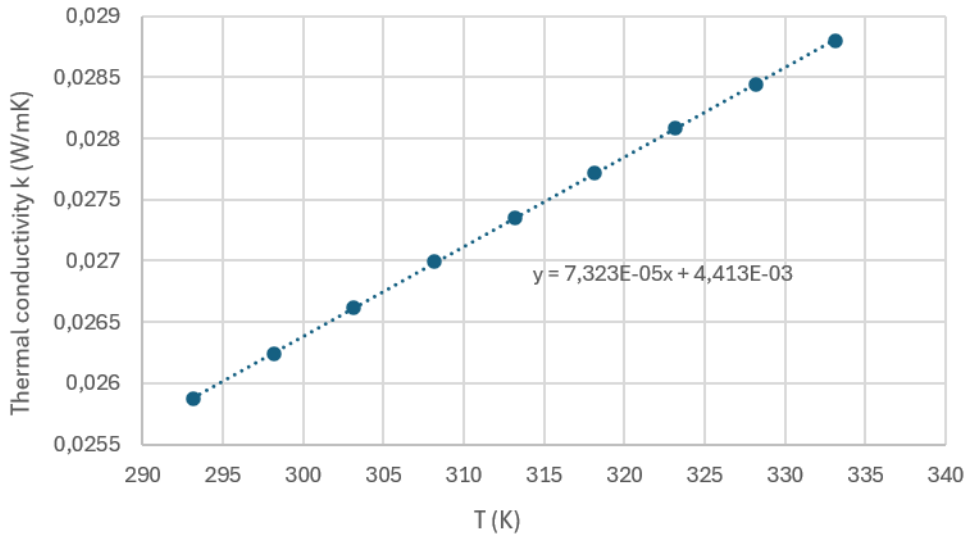


Figure A2 – 2 Fit for thermal conductivity, data from The Engineering ToolBox (2009).

General form of the fit

$$h = A(T - B)^n$$

Correlation for vertical plane's heat transfer coefficient:

$$h_{vert} = 2.82(T - 293.1)^{0.233} \quad (1)$$

Correlation for horizontal plane's heat transfer coefficient:

$$h_{horz} = 3.77(T - 293.1)^{0.211} \quad (2)$$

Appendix 3. Approximate and extrapolated relative errors of two finest grids

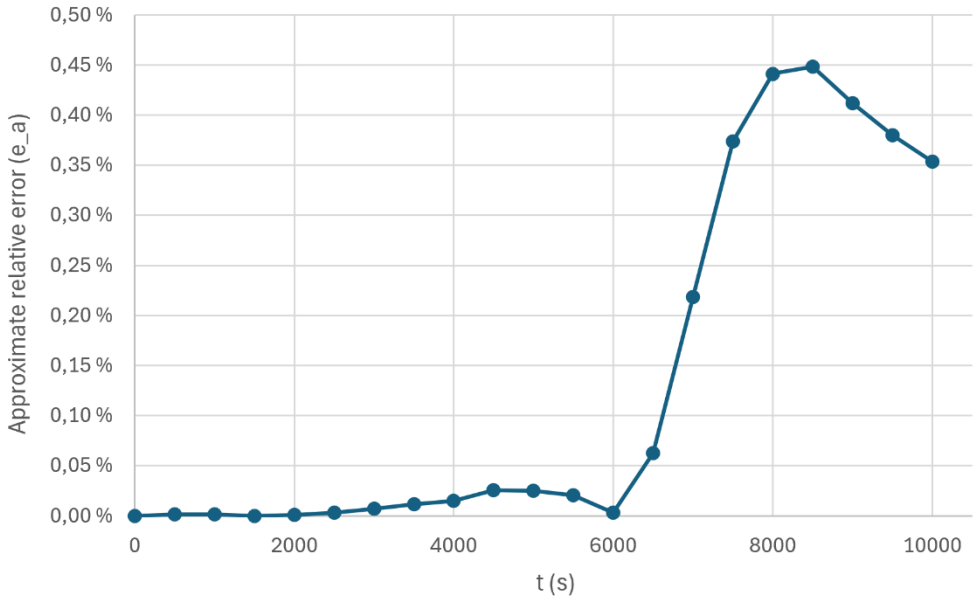


Figure A3 – 1 Approximate relative error

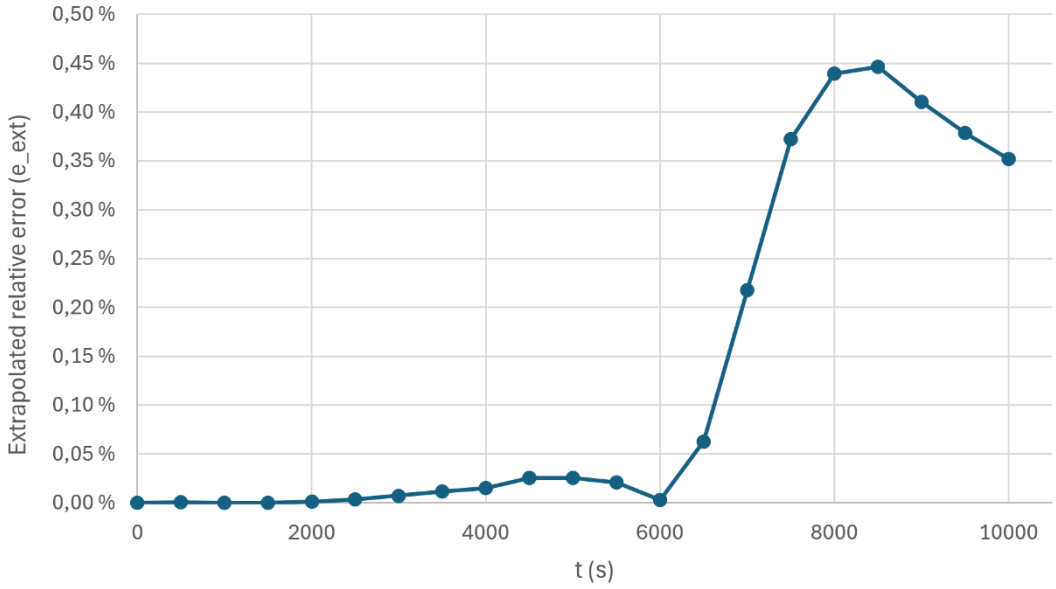


Figure A3 – 2 Extrapolated relative error

Appendix 4. Maximum temperatures of each cell

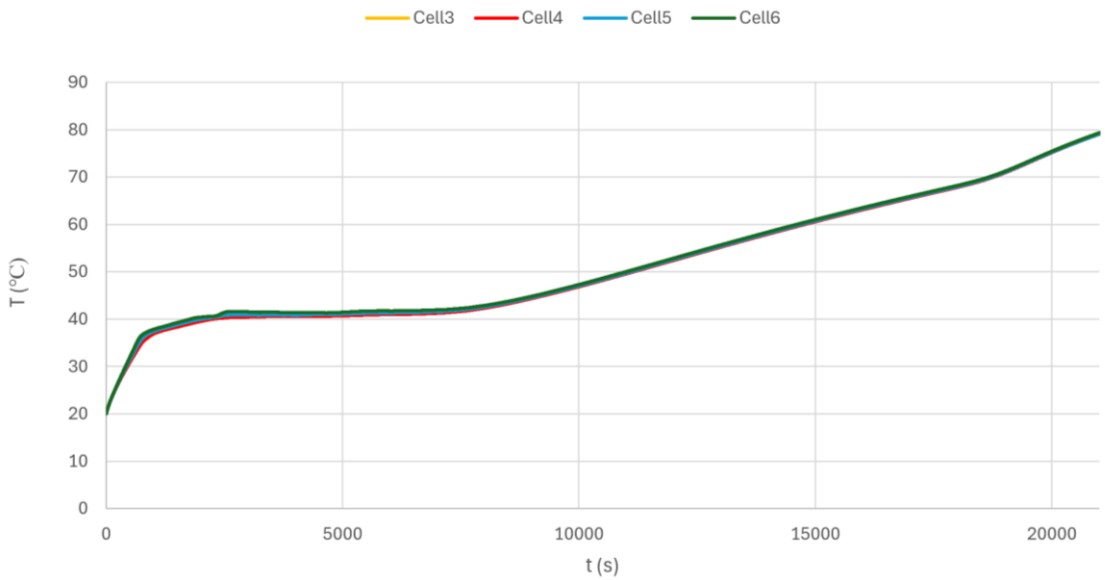


Figure A4 – 1 Maximum temperatures of cells 3, 4, 5 and 6

Appendix 5. Cell Temperatures with and without PCM with longer simulation time

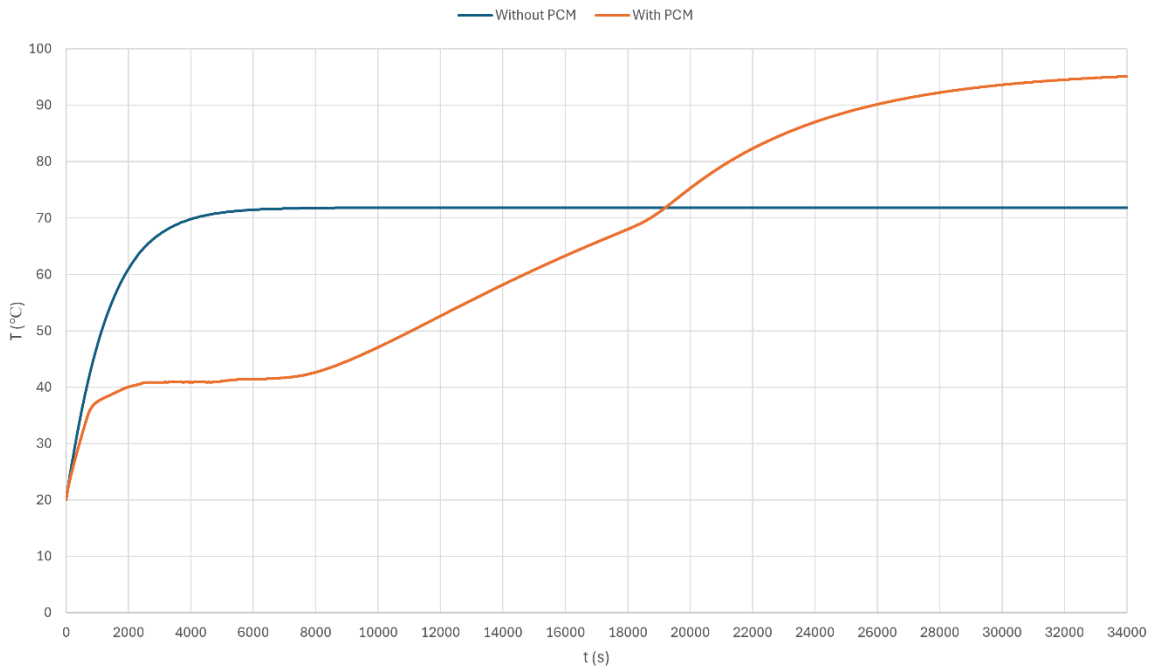


Figure A5 – 1 Cases with and without PCM

Appendix 6. Thermal image, experimental

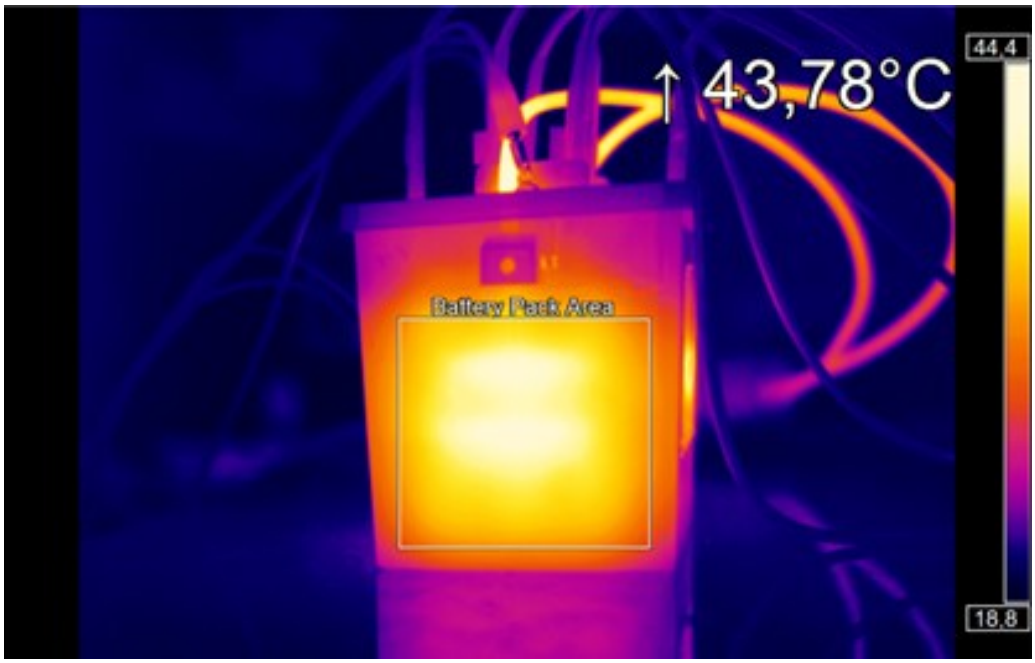


Figure A6 – 1 Thermal image at 2C with PCM (Avik et al. 2025)

Appendix 7. Experimental study

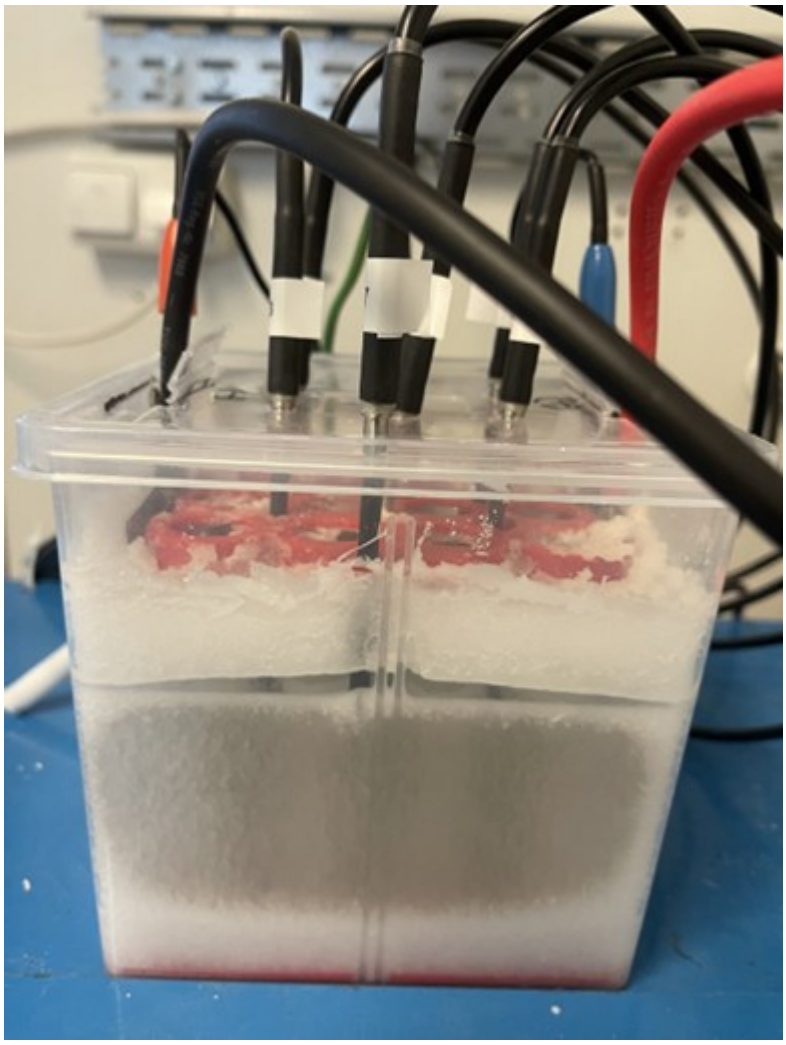


Figure A7 – 1 Experimental study, PCM after 2C cycling (Avik et al. 2025)